Technische Universität München

Lehrstuhl für Bioverfahrenstechnik

Vibration packing of liquid chromatography columns

Andrés David Martínez Merizalde

Vollständiger Abdruck der von der Fakultät für Maschinenwesen der Technischen Universität München zur Erlangung des akademischen Grades eines Doktor-Ingenieurs genehmigten Dissertation

Vorsitzender:		Prof. dr.ir. Daniel J. Rixen
Prüfer der Dissertation:	1.	Prof. Dr.-Ing. Dirk Weuster-Botz
	2.	Prof. Dr.-Ing. Heiko Briesen

Die Dissertation wurde am 28.10.2019 bei der Technischen Universität eingereicht und durch die Fakultät Maschinenwesen am 13.04.2020 angenommen.

Acknowledgements

The work and research in this dissertation took place during my activities as scientific researcher at the Institute of Biochemical Engineering of the Technical University of Munich, under the supervision of Prof. Dr.-Ing. Dirk Weuster-Botz, and would not have been possible without the help and support of colleagues, friends and family.

Foremost I would like to thank Prof. Dr.-Ing Dirk Weuster-Botz for his trust giving me the great opportunity to work in such an interesting project, for his continuous support and supervision guiding this scientific effort, as well as for the provision of the outstanding facilities, resources and equipment of the Institute of Biochemical Engineering and his permanent willingness and openness for discussion.

Many thanks to PD Dr.-Ing. Dariusch Hekmat for his scientific and practical guidance regarding equipment and experiments, as well as the long constructive discussions we had over papers, presentations and the direction of the project. Also many thanks for his outstanding role finding and providing material and scientific resources from industrial partners.

I would also like to thank Prof. Dr.-Ing Heiko Briesen of the Chair of Process Systems Engineering for assuming the role of second examiner, for his support and advice during our research cooperation and for fomenting my scientific curiosity during my master's thesis at his chair well over 4 years ago. As well to Prof. Dr.-Ing. Daniel Rixen for acting as Chairman of the examination commission and his support during the defense process.

Many thanks to present and past colleagues at the Institute of Biochemical Engineering, the Professorship of Bioseparation Engineering and the Specialty Division for Systems Biotechnology for the supportive and collegial work atmosphere. Special thanks to those colleagues who crawled (or made me crawl) under the kicker-table during our infrequent impulse-transfer stress-reducing experiments. I also warmly thank all past and current technical and administrative employees at the institutes whose work enable the smooth functioning of the PhD students' activities and research - Ellen, Gabi, Georg, Markus, Marlene, Norbert, Patrick and Michaela.

To all my students; Berk, Xinyi, Marc, Matthias, René, Konsti, Fatemeh, Nikita, Qinhao, Yosua, Zewen, Bernhard, Altay, Arul, Thiemo und Max, thank you very much for the productive work and engaging discussions.

Por encima de todo, este trabajo esta dedicado a mi familia, sin cuyo apoyo nada hubiera sido posible. Aún en la distancia su continuo aliento y fé en mi, en especial durante tiempos turbulentos, reforzaron mi convicción en la idea subyacente a nuesta cultura: *echaos pa'lante!*

Men say they know many things;
But lo! they have taken wings, —
The arts and sciences,
And a thousand appliances;
The wind that blows
Is all that any body knows.

HENRY DAVID THOREAU

Contents

1. Introduction

Industrial biotechnology comprises the application of biotechnological tools for the commercial manufacturing of a broad range of products through the metabolic pathways of whole microorganisms, cells or their individual components, such as enzymes and cell walls. Although it has been a tool used by mankind since the neolithic, modern advances in genetic manipulation and process technology have heralded a new era of increase in innovation and use of biotechnological tools for large-scale industrial production [1], so called biomanufacturing. Estimated to have reached world sales in the order of €340 billion in 2017 [2], biotechnology also holds considerable market share in strategic segments, such as active pharmaceutical ingredients (API), at an estimate of 47.9 %. Often characterized by the use of renewable feedstock, biomanufacturing using genetically optimized microorganisms or cell cultures can also deliver products faster and at a higher resource- and environmental sustainability, resulting in lower costs and energy use [1].

As humanity approaches the climate change Rubicon, the potential for a bio-based economy decreasing fossil fuel use and waste generation have set high growth expectations for the field in the foreseeable future. Additional to intrinsic market pressure, governmental policies are increasingly supporting the expansion of industrial biotechnology into commercial maturity [2].

Among the wide range of bio-derived products such as chemicals, fuels and polymers; biotechnological tools provide particularly considerable advantages for the production of active pharmaceutical ingredients. Recent strides in molecular biology, improvement of protein expression and drug discovery have expanded the usage of biological-based therapeutics into a wide range of products, with substances such as peptides, lipids, oligonucleotides, proteins and monoclonal antibodies (mAb) entering the market [3]. As world population increases and western countries get older, the need for improved healthcare has driven the pharmaceutical field to increasingly adopt biologics, attracted by high potency and target selectivity.

In general, biomanufacturing can be divided into two subunits; upstream and down-

stream processing (Figure 1.1). The former encompasses the action of the biocatalyst under controlled conditions inside a bioreactor, and the setting and optimization of fermentation conditions. Due to intrinsic properties of biological systems, this unit is characterized by diluted concentrations of the bioproduct in aqueous solutions. The goal of the second process unit is to purify the target molecule for the production to be competitive with chemical processes. Besides low concentration, the bioproduct itself is often sensitive to temperature and solution composition, which limit the available purification steps and parameter space.

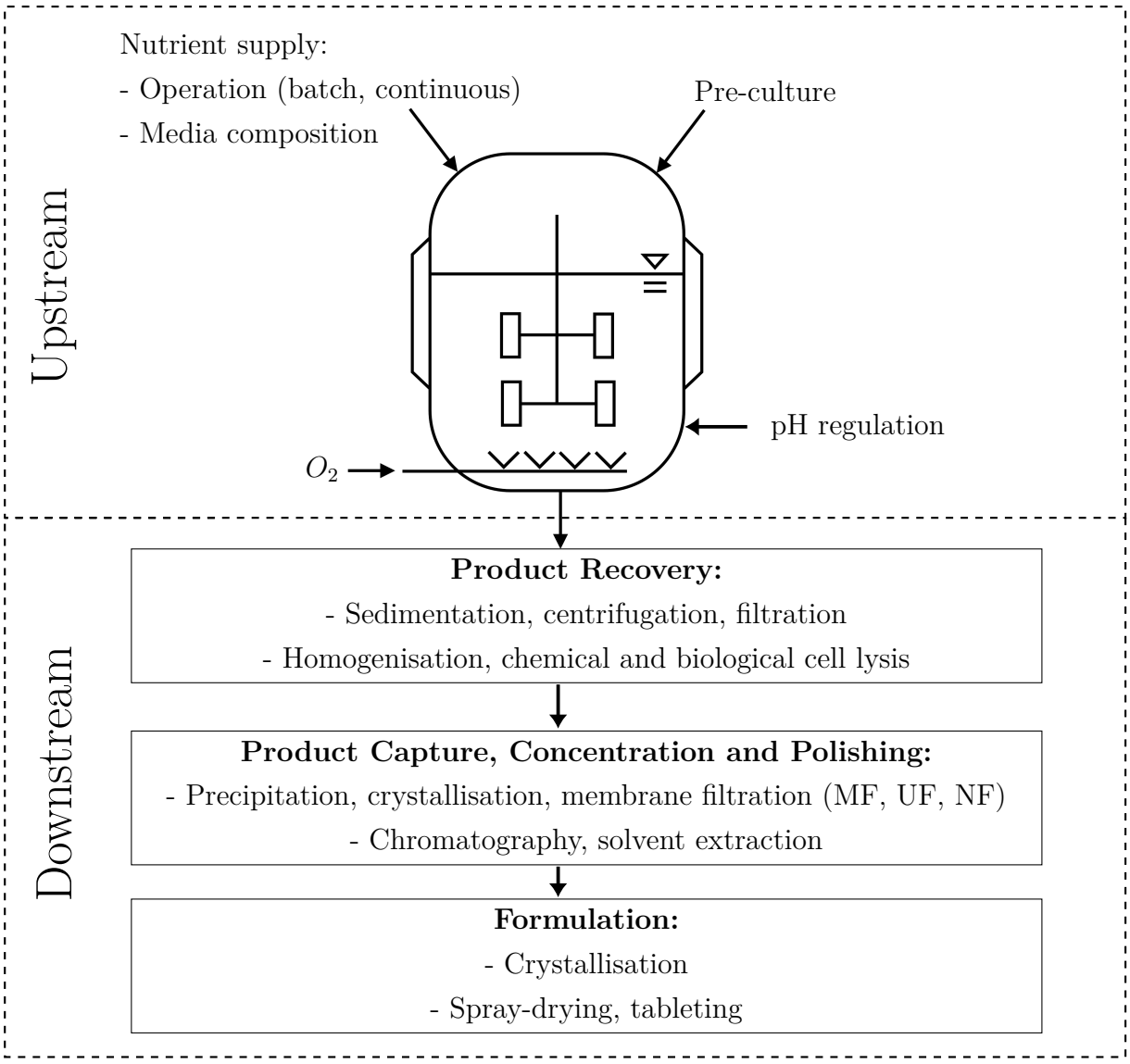

Fig. 1.1.: Bioprocess general overview, modified from [4].

2. Motivation and scope

In practice, the downstream processing of bioproducts often represents the bottleneck of the overall process, with up to half of the costs of bioproduct manufacturing arising during this step, specially in the production of pharmaceutical proteins or macromolecules [4]. Due to these substances being pH- and temperature sensitive, liquid chromatography (LC) is often the most suitable separation operation among the possible purification steps at the different stages.

Figure 2.1 exemplarily shows the downstream operations during production of monoclonal antibodies (mAB) [5], large proteins involved in the immune response to pathogens. Besides virus inactivation steps, the product capture, concentration and polishing are all carried out using different LC modes. The wide use of LC in biomanufacturing, often termed biochromatography, comes as result of the stringent purity requirements of governmental regulatory agencies, and the mild conditions during chromatographic separations, characterized by low shear forces, low temperatures and buffered solutions, which help maintain biological activity of the product [4].

The principle of chromatography relies on the contrast in adsorption thermodynamics of different components in solution to the solid surface of chromatographic media, and depends on the surface active groups and the chemistry of each individual solute. In simplified terms, components can be more affine to either the solid phase or to the liquid solution. This affinity determines how a component partitions between both phases when these are in contact, and the resulting equilibrium concentration in each phase.

In practice, liquid chromatography is most commonly done in a cylinder filled with consolidated microscopic chromatographic particles forming what is termed the chromatographic bed, with permeable nets at the column ends to retain the media. The network of microscopic channels formed by this structure (seen in Figure 2.2b) allows the perfusion of the liquid solution containing the components to be separated, either by gravity or forced mechanical action. The solution enters the chromatographic column as a volume of initially homogeneous mixture, which becomes separated as it travels

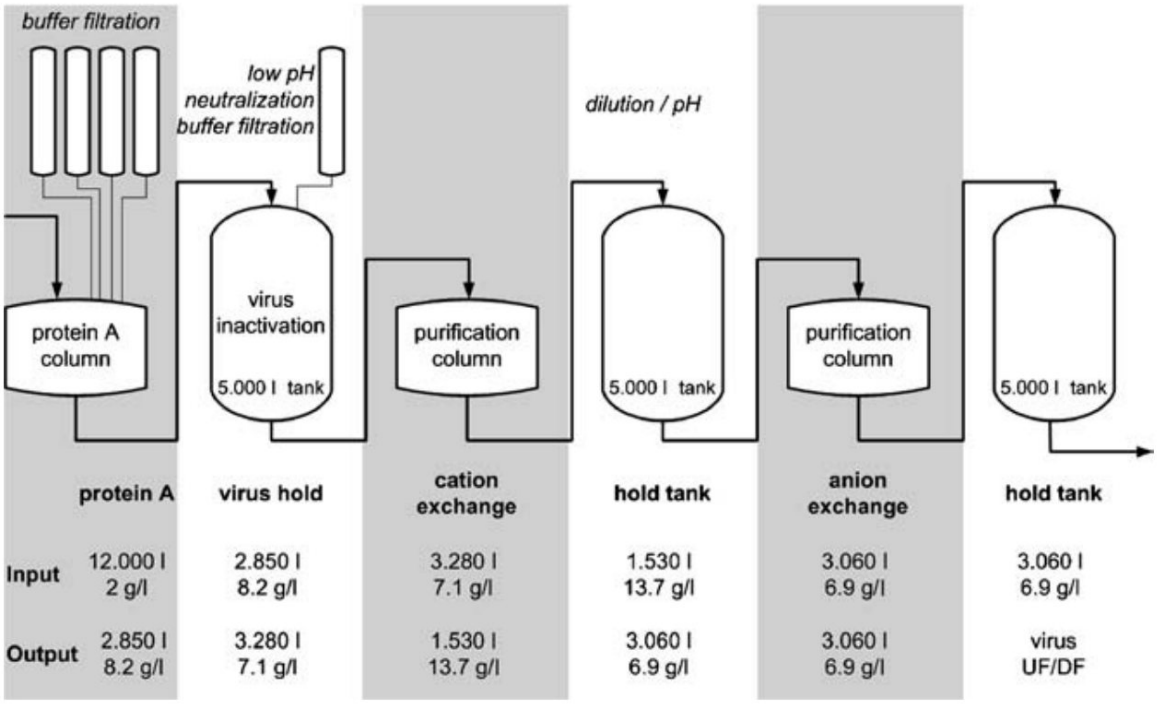

Fig. 2.1.: Downstream processing steps in large-scale macromolecular monoclonal antibody production. Liquid chromatography is essential for the production of these macromolecules. [5].

through the column and its components interact with the media. Components affine to the solid media have longer column residence times and will elute later than less-affine ones, enabling the separation of individual solutes by collecting the different eluate fractions at the column outlet [4].

Besides surface chemistry of the chromatographic media and solution composition, the geometric structure of the porous bed plays an important role during separation due to its effect on flow distribution. For example, the presence of channels represent a region of low hydraulic resistance for the solution to flow through and can lead to the solution bypassing sections of the chromatographic bed. Large voids inside the packing lead to backmixing and dilution of the components, undoing previous separation. Thus, the amount of voids inside the column, also called porosity, is a bed property used to estimate the quality of a packed column [6], with denser beds being usually more efficient than less dense ones [7], albeit not necessarily [8].

Even in the absence of large bed defects, the homogeneity of the chromatographic structure determines how homogeneously the solution will flow through the column, and how diluted the separated solute fractions will exit. The process through which the structure forms is termed packing, and consists most commonly in the consolidation of

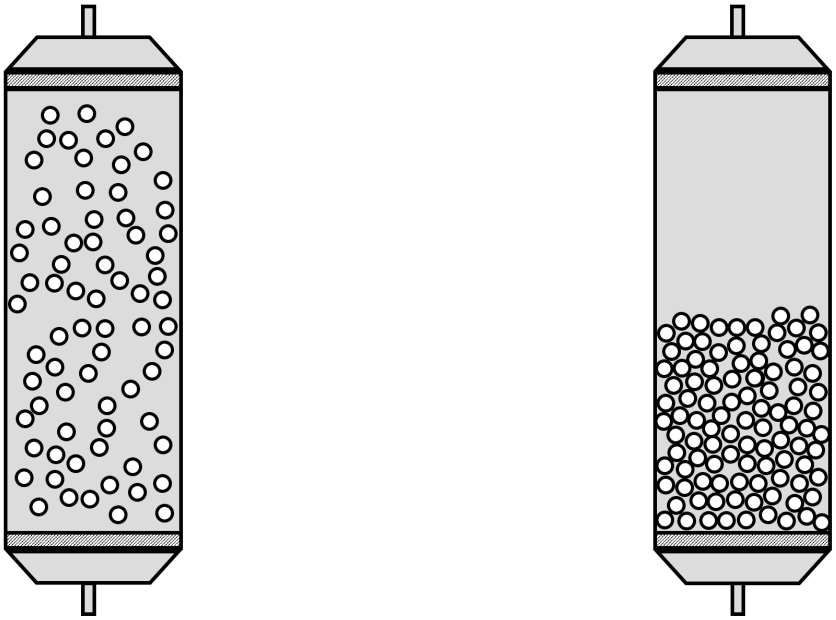

(a) Suspension of chromatographic particles in the column before packing.

(b) Packed particles forming the chromatographic bed.

Fig. 2.2.: Most biochromatography columns are packed starting from a suspended particle slurry. The steps taken to form the bed determine its final structure, and are termed "packing".

spherical microscopic particles into a packed bed, shown in Figure 2.2. The starting condition consists of a particle suspension, also called slurry, contained inside the column (Figure 2.2a) which through diverse steps is directed to the bottom of the column until a stable packing is created (Figure 2.2b). Once this has taken place, the top flow distributor (not shown) is lowered and placed in contact with the bed, bypassing the particle-free solution (top region in Figure 2.2b) created during packing.

Most packing methods consist in the use of flow drag, mechanical compression, or a combination of both. The viscous drag generated during flow packing carries the particles in the flow direction, and are retained inside the column by glass wool, metallic or polymeric frits, which permit the solution to flow through. Mechanical compression is most commonly applied at the end of the packing process and consists of driving the flow distributor into the particle bed. While manufacturers of chromatographic media recommend individual packing protocols for each media [9, 10, 11], and diverse packing methods can be found in the literature [5], these are all in essence variations and combinations of flow or mechanical compression packing.

Chromatographic column packing is a granular densification process, sharing a phys-

ical background with other areas, such as compaction of powder metals in metallurgy, tableting of pharmaceuticals and soil compaction in civil engineering. A characteristic of such granular materials is the microscopic heterogeneity that can take place during compaction or packing. Due to their opaque and microscopic nature, these heterogeneities are not observable at the macroscopic scale, and are of limited experimental accessibility [12, 13], with computer simulations often being used to discern them [14]. Employing both approaches it has been found that while it is possible to pack a chromatographic bed to the same macroscopic compaction degree with flow or mechanical packing, the compression is microscopically different and heterogeneous with each approach (see Figure 2.3), with flow packing forming denser region on the packing bottom, and mechanical compacting compacting mostly the top bed region.

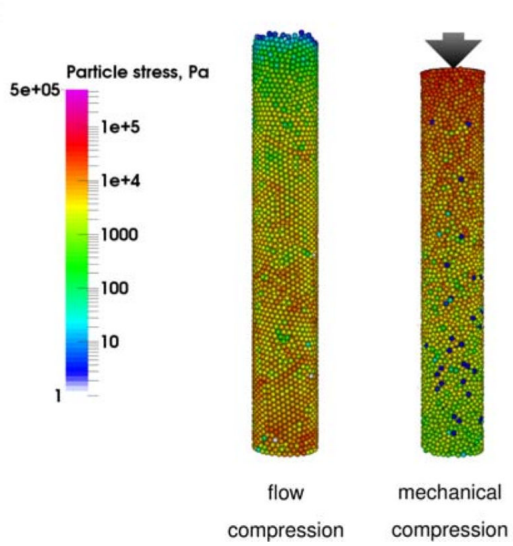

Fig. 2.3.: Packing simulation of a chromatographic bed through flow or mechanical compression. While both methods cause an heterogeneous compaction, flow packing mostly compacts the bottom region of the packing, while mechanical compression overwhelmingly acts on the top region. These heterogeneities are macroscopically not evident during experiments [14].

Furthermore, besides axial differences due to packing steps, it has been observed that columns are also radially heterogeneous. Figure 2.4 shows the effect of column radial heterogeneity on the dispersion of an iodine injection due to heterogeneities in flow distribution caused by the packing structure. Iodine is unretained and does not interact with chromatographic media, so its broadening arises essentially by hydrodynamic dispersion, a term grouping solute advection and diffusion [15]. Due to a higher porosity near the column wall, flow is locally faster than in the bulk of the packing.

As the solute travels through the column, differences in flow velocity cause the initially concentrated solute zone to broaden, resulting in a diluted solution eluting from the column. In real applications, diluted components represent low separation efficiencies.

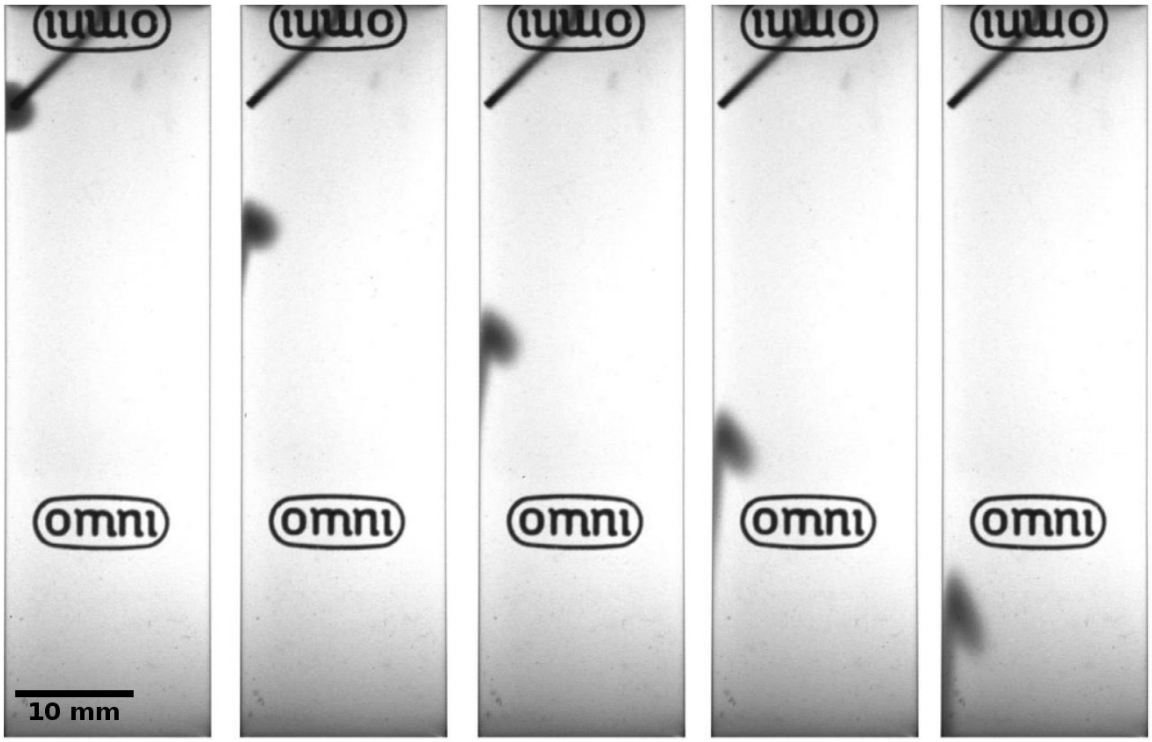

Fig. 2.4.: Visualization of structure heterogeneity in a chromatographic bed. Iodine was injected to the wall region of a packed column in the leftmost picture and subjected to flow (pictures taken approximately every minute). The injected iodine solution moves faster at the wall region due to higher local porosity and corresponding lower hydraulic resistance. The solute volume broadens as it advances through the bed, becoming diluted [16].

Just as in the axial direction, radial heterogeneity also depends on the packing conditions and protocols. Figure 2.5 shows the packing dynamic of the same packing method carried out at two different slurry concentrations. In both cases, flow packing was applied to the particle suspension, and the consolidating bed followed optically.

At high slurry concentrations (see Figure 2.5a), the bed was formed by the layering of large particle clumps, which resulted in the formation of larger voids due to the short time available for particles to move into a void before being locked in place by arriving clumps on top. On the other hand, a more dilute particle slurry (see Figure 2.5b) result in the particles arriving individually onto the bed front, and having enough time to move and rearrange. While this diminishes the amount of voids in the final structure, it enables size segregation of the particles, observed as an increased radial heterogeneity

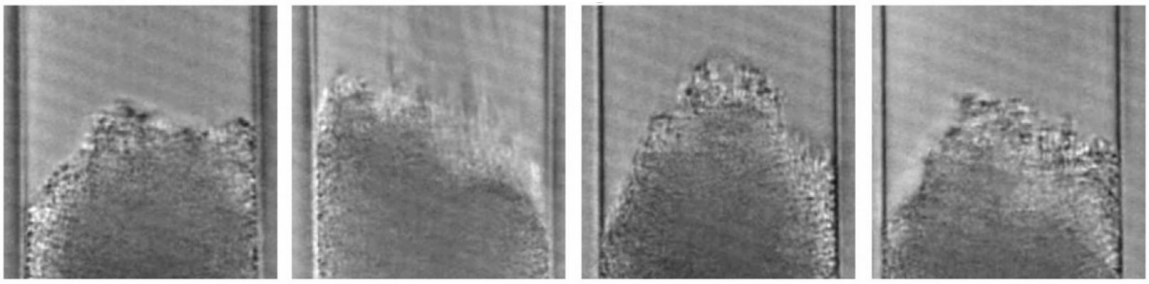

(a) Bed formation during flow packing of a slurry with a concentration of 100 $^{mg}/_{ml}$. At higher concentration particles arrive in clumps forming an irregular bed front.

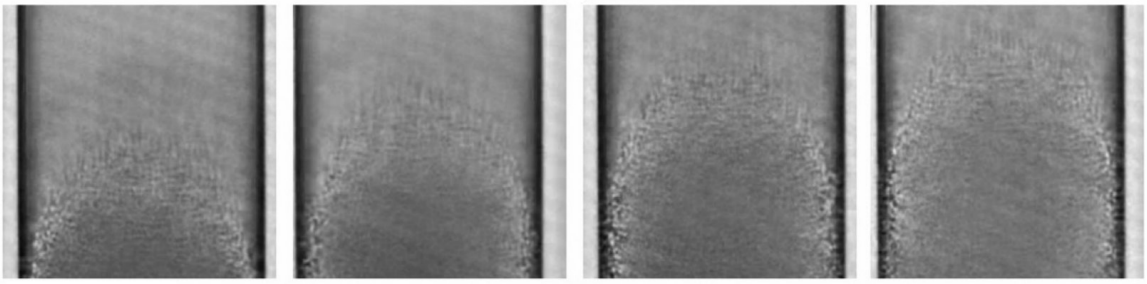

(b) Bed formation during flow packing of a slurry with a concentration of 10 $^{mg}/_{ml}$. At dilute concentrations particles arrive individually, forming a cone shaped growing bed front.

Fig. 2.5.: Influence of slurry concentration on the formation of the packed bed of silica particles in fused-silica tubing (75 µminternaldiameter). Bed was formed by flow packing using acetone as pushing solvent [17].

[17].

Besides flow distribution, the geometry of the packing determines the stability of the chromatographic column under long-term operation. Voids remaining after packing can be later occupied by rearranging particles as the bed undergoes use, which often comprises the pumping of mixtures with different viscosities through the bed, having a de-stabilizing effect. This unwanted compression taking place during operation can lead to the formation of a head-space between the top distributor and the bed, channeling in the packing, or to a locally inhomogeneous compaction. All of which negatively impact separation and are observed as a deterioration of the column efficiency over time, often requiring the re-suspension and re-packing of the column.

The evolution of column homogeneity during separation cycles can be seen in Figure 2.6. Three columns packed using either flow-packing, mechanical compression (also called DAC - Dynamic Axial Compression) or a combination of both were subjected to simulated separation cycles. S_{init} represents the degree of heterogeneity, with lower values indicating more homogeneous columns. It was observed that mechanical packing

alone delivers a packing stable over time, albeit comparatively heterogeneous. Flow-packing results in an initially more homogeneous structure, which however is unstable and becomes more heterogeneous under operation stress. A combination of flow and mechanical packing can deliver a packing which can be both initially homogeneous and stable over time [13].

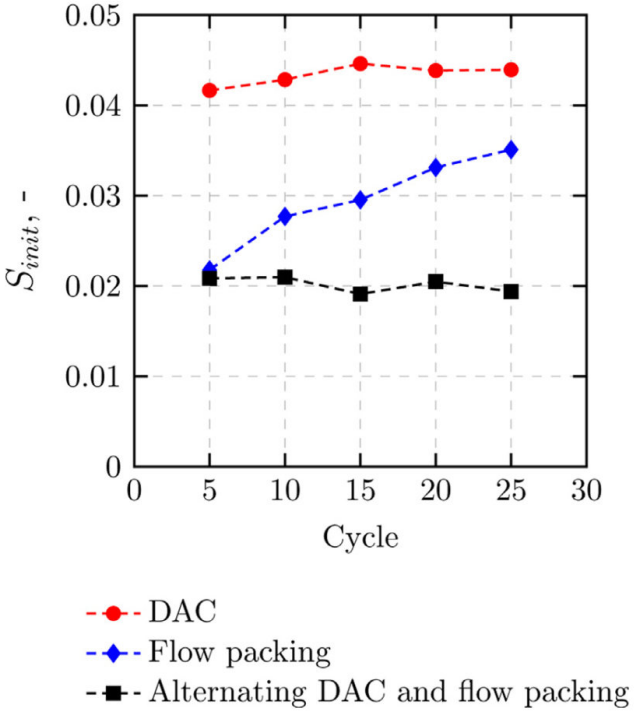

Fig. 2.6.: Evolution of structure homogeneity under operation of columns packed using mechanical compression (also called DAC - Dynamic Axial Compression), flow packing, or a combination of both. S_{init} indicates the degree of heterogeneity, with lower values corresponding to more homogeneous columns [13].

Among other granular densification problems, the use of mechanical vibrations is commonly used to affect compaction. For example, pneumatic vibrators are often used to compact soil and cement, or ultrasonic transducers to compress metal powders for posterior sintering [18]. A similar approach has been reported during the packing of chromatographic capillaries. A column was submerged in an ultrasonic bath while flow packing took place, after which the separation efficiency was determined for sonicated and non-sonicated columns. The two column groups were compared using the Reduced Height of Equivalent Theoretical Plate (see Section 3.1.2 for more information), which are plotted in Figure 2.7 as h against the non-dimensional flow velocity v. In short, more efficient columns exhibit lower h than less efficient ones at same velocities. The

sonicated columns were more efficient than standard ones, indicating that ultrasonic vibrations acted on the packing to achieve a more homogeneous structure.

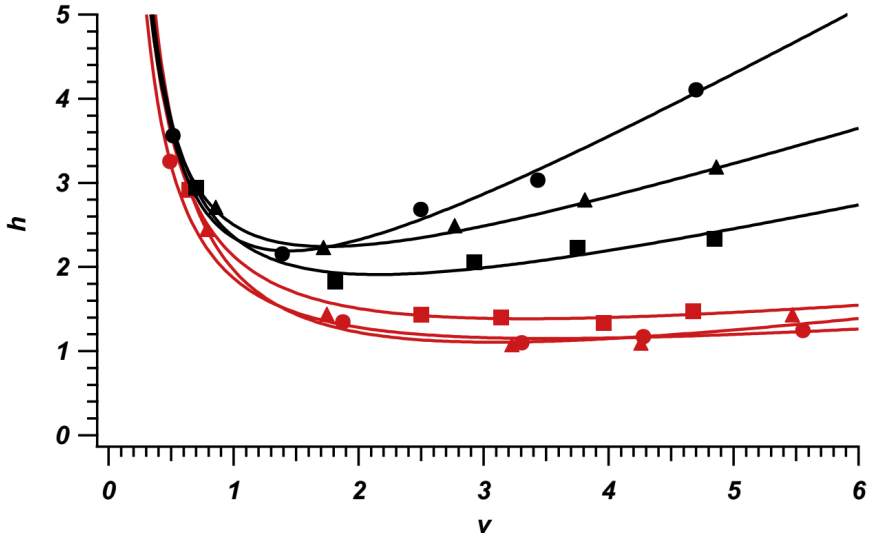

Fig. 2.7.: Comparison of chromatographic capillaries flow packed with (red points) and without (black points) ultrasound [19]. Lower h denote more efficient columns (see Section 3.1.2 for more information). Columns packed under ultrasound are more efficient than standard ones.

A problem specific to chromatographic packing is the requirement of microscopic homogeneity. While vibration most often leads to a macroscopic compaction which suffices for non-chromatography applications, it is not necessarily linked to homogeneity at a microscopic level, and can potentially lead to inhomogenous structures, as shown previously for flow or mechanical packing. Indeed, this has been reported on other experiments on the ultrasound packing of chromatographic columns. It was shown that although the use of ultrasound for the additional settling of chromatographic columns delivered denser packings, these were however more heterogeneous and thus, less efficient overall [20].

In summary, though highly selective, chromatographic separations are limited by solute volume broadening due to hydrodynamic dispersion [5] and long-term column stability, both affected by the bed structure. Irrespective of chromatography mode, particle type or process parameters, if the bed is heterogeneous or contains void defects, irregular flow and back-mixing will lower column efficiency [8] and make the bed prone to unwanted settling under operation. With API-markets alone worth an estimated of $ 230 billion in 2016 [21], an improvement in the chromatographic step would positively affect the profitability and competitiveness of a large market sector.

2.1. Objectives

Current column packing technology presents several problems regarding the fundamental understanding of the process, and its practical application.

There is a lack of understanding of the packing process of chromatographic particles due in part to the inability to measure the real structure of packed beds. Although simulation approaches have delivered important insights into the physical events during packing, there is a need for 3-dimensional reconstructions of real packed biochromatographic beds. Among other possibilities, this would enable to study the link between packing methods and resulting bed geometry, and the evolution of granular structures through particle migration under operation.

In practice, this lack of fundamental background results in the development of empirical packing methods achieving columns far from their most efficient state. This is reflected in conventional procedures often have difficulties delivering reproducible, dense and homogeneous columns. Column variability can negatively impact overall process reliability and require time and personal intensive re-packing, while poorly-packed inhomogeneous columns directly affect the efficiency of chromatographic separation through unfavorable hydrodynamics. Furthermore, poorly-packed columns will continue to settle during operation cycles and column transport, possibly forming a gap between bed and flow distributor, channeling in the packing or wall separation.

The objectives of this work are two-fold:

- Improve the understanding of the relation between packing structure and column efficiency by developing a novel imaging method enabling exact measurement of the 3-dimensional microstructure of columns packed with biochromatography particles. This information has been previously unavailable due to chromatographic media having high internal porosities and being composed by low density materials, which makes them difficult to measure.
- Study the implementation of ultrasound and mechanical vibration for the packing of liquid chromatography columns. Granular matter densification is a process which, although widely used in industry, is not well understood and deceivingly complex. Given the sensitivity of chromatographic separation to heterogeneities in the packed bed, the goal is to achieve macroscopic bed compaction while retaining or improving microscopic homogeneity.

3. Physical and theoretical background

3.1. Chromatography

Chromatography is a separation process used for the partition of a an initially homogeneous molecular mixture solved in a carrying solvent into its individual components. The mixture components are carried in a fluid phase in contact with a second added phase, most commonly a solid, with which each component has a different affinity. Due to different thermodynamic equilibria in each phase, an exchange of mass and energy takes place between them and the mixture is separated by the relative movement of each component between the two phases. Once mass transport has taken place, each component has a different concentration in the solid and liquid phase depending on their affinity. For the hypothetical separation of two components A and B, the ideal case would correspond to one component being more affine to and being more concentrated at the solid surface, while the other one being more affine to and being more concentrated in the solution. At this point, the components can be isolated by separating one phase from the other [5].

Commonly, the solid phase is fixed in place and designated as the stationary phase, while the phase containing the mixture flows through it and is termed the mobile phase. Depending on state of matter of the mobile phase, chromatography processes can be divided in gas chromatogarphy (GC), liquid chromatography (LC) and supercritical chromatography (SFC). Other phase presentations exist, such as thin layer chromatography (TLC), consisting in the mixture being placed separately from the mobile phase on a thin layer of the stationary phase which is dipped in the mobile phase [5].

Most typical chromatographic processes are based on the adsorption of molecules dissolved in a liquid phase onto the surface of a solid. This is also true for the majority of industrial preparative chromatographic processes, concerned with the production of highly pure substances, in contrast to analytic chromatography, in which the goal is the

identification of the components in a mixture.

The stationary phase is usually packed in a cylindrical container forming a solid network of pores through which the mobile phase flows, and in which the mixture to be separated enters as an homogeneous feed.

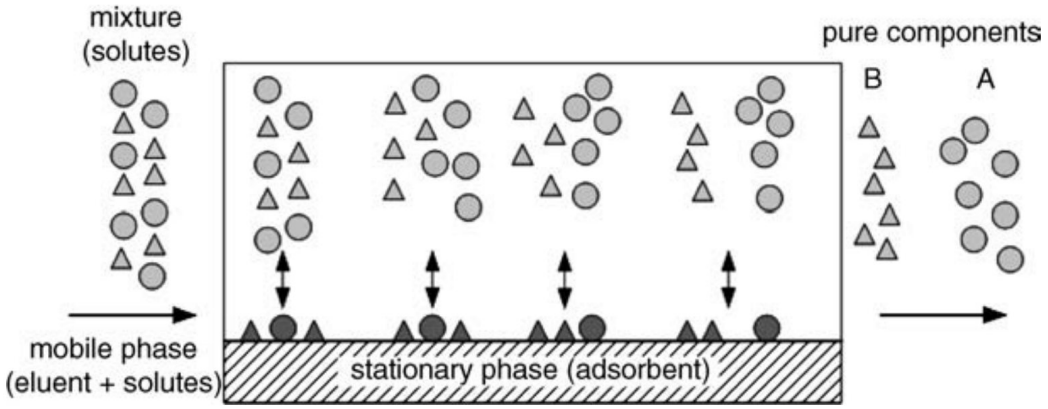

Fig. 3.1.: Mechanism of adsorption chromatography. A binary feed mixture of components A and B enter the column as an homogeneous mixture. Component B has a higher affinity to the stationary phase and elutes the column after component A as the solution is forced to flow through the packed bed [5].

Figure 3.1 shows the working principle of a liquid chromatography process. The component with the comparatively higher affinity to the stationary phase will more readily adsorb onto its surface, leaving the mobile phase. The component with less affinity for the stationary phase preferentially remains in the mobile phase, leaving the column first. Depending on process conditions, it is possible for the feed mixture to leave the column completely separated in its pure components [5].

Interaction between the components and stationary phase can be based on size exclusion, ion exchange, hydrophobic interaction, affinity or mixed mode, among others [22] and determines, along with buffer composition, the elution order.

While monolithic columns have gained considerable relevance in the last decades, preparative industrial liquid chromatography columns are still mostly packed with microscopic particles forming the porous stationary phase [23]. More specifically, industrial biochromatography often employs compressible, porous particles based on organic polymers, such as agarose, polymethylacrylate and cellulose. Other biochromatography media include rigid, near-spherical ceramic hydroxapatite [24] and irregurlaly shaped porous glass particles [25]. Figure 3.2 shows the different porosities that define a packed column. Inter-particle volume (V_{Int}) describes the macroscopic pore volume through

which the mobile phase flows, moving dissolved components by advection. The volume occupied by the adsorbent (V_{Ads}) can be further divided into the purely solid particle matrix (V_{Solid}), and the pore volume in the particles (V_{Pore}), in which components diffuse [5].

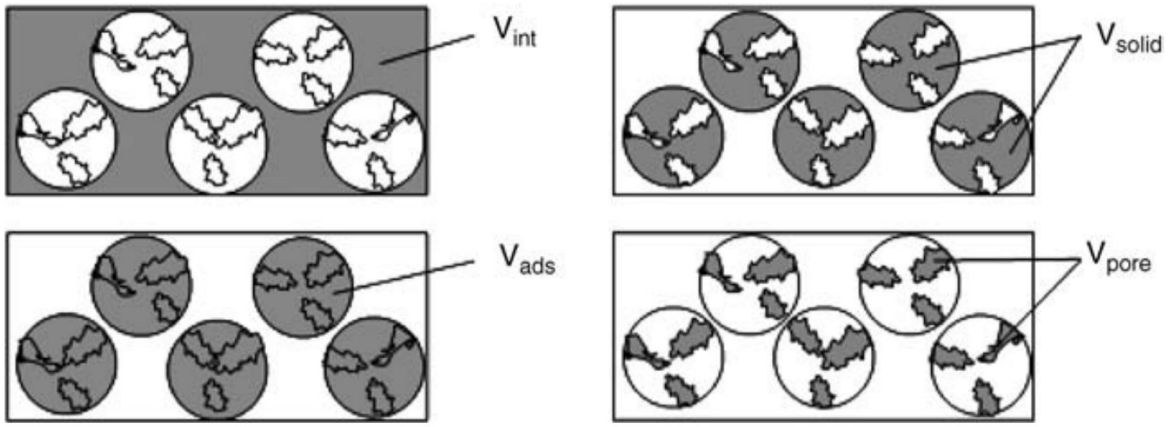

Fig. 3.2.: Different porosity and void categories in a packed column. V_{Int} denotes the space between particles, which form V_{Ads}. The latter can be further divided into its solid structure V_{Solid} and pore system V_{Pore} [5]

Column porosity or void fraction (ε), an important property of packed beds often used to determine whether a bed has been correctly packed, can be determined through:

$$\varepsilon = \frac{V_{Int}}{V_{Column}} \tag{3.1}$$

The corresponding solid ratio can be obtained through:

$$\varphi = 1 - \varepsilon \tag{3.2}$$

Each type of porosity plays a role on column efficiency. For example, Figure 3.3 exemplarily shows the elution behavior of two components based on size exclusion. Smaller molecules able to diffuse into the pore system V_{Pore} of the adsorbent elute later than larger components, which can only traverse the V_{Int} [5]. In this case, the ratio of the porosities partially determines whether the eluting peaks overlap.

3.1.1. Hydrodynamic dispersion

Besides component adsorption determined by thermodynamic equilibrium in both phases, the change in concentration is affected by dispersion, which arises due to the interaction

between diffusion and advection [15]. These effects are a consequence of the hydrodynamics of fluid distribution, and solute band dispersion will take place even if the dissolved component does not directly interact with the stationary phase.

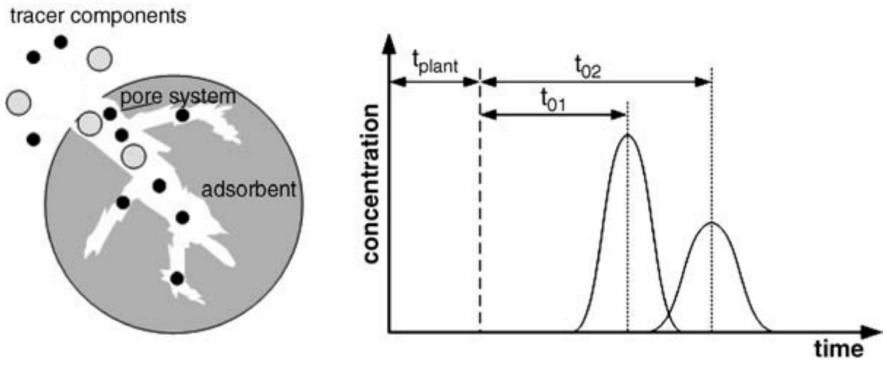

Fig. 3.3.: Elution behavior of a mixture based on size exclusion chromatography. Small components with more available space take longer to elute than larger molecules [5]

Figure 3.4 shows the transit through a column after injection of a single component. The starting solution has a constant concentration, and the local region of the column in which it was injected has a rectangular concentration profile of the component ($X = 0$). As the mobile phase carries the mixture through the column, the initial solute band widens and the concentration decreases, acquiring a Gaussian distribution profile.

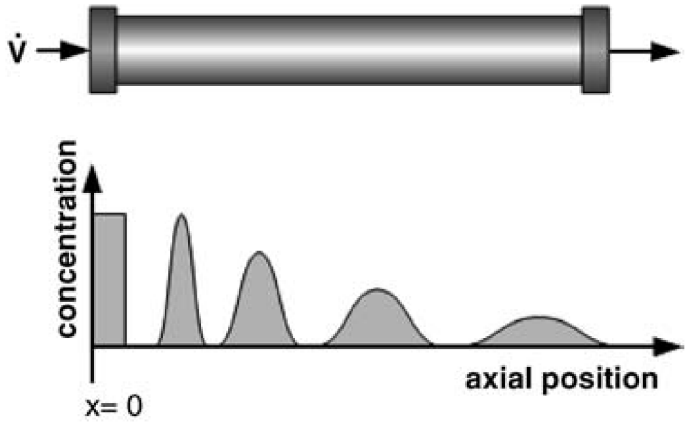

Fig. 3.4.: Dispersion of an injected solute band as it traverses a packed column [5]. Component concentration changes over time even if it does not interact with the stationary phase. Final chromatogram has a Gaussian profile.

The ideal flow profile in a column would correspond to a plug flow condition in which the velocity along the column area is homogeneous. There are several reasons for non-ideal fluid dynamics in real packed columns (Figure 3.5). For one, microscopic

channels built by the particles cause a velocity gradient with the lower velocities at the channel walls. Local variation of packing properties such as porosity or voidage cause different flow velocities at the mesoscopic scale, and also result in eddy diffusion of the solute molecules as these take different paths through heterogeneous structures. Macroscopic velocity gradients are caused by heterogenous properties along the entirety of the column. For example, the nearest particle layer to the column wall has an ordered structure characterized by a single-point contact between each particle and the column. Since the particles cannot enter the flat wall, voidage is at its maximum and rapidly diminishes (see Figure 5.12), causing a large porosity and hydraulic resistance gradient.

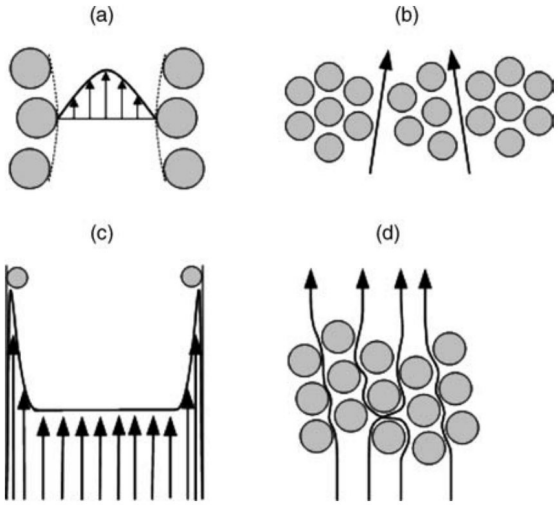

Fig. 3.5.: Fluid inhomogenities at different scales. **(a):** microscopic channel causes a parabolic velocity distribution, **(b):** mesoscopic heterogeneities in packing porosity, **(c):** macroscopic structural difference causing a velocity gradient along the entire column, and **(d):** eddy diffusion [5].

In general, fluid distribution non-idealities arise from the lack of an homogeneous packing structure in the entirety of the column. Such structure would, under ideal conditions of mono-dispersity, take the form of a face-centered cubic (FFC) or hexagonal close-packed (HCP) lattice (shown in the following section). These crystalline structures are homogeneous repeating units building the most-dense possible structure with a porosity of approximately 26 % [26]. In real columns, poly-dispersity of chromatographic media and the practical difficulty of packing an homogeneous crystalline structure of microscopic units in a macroscopic cylinder mean that chromatographic beds are amorphous structures with heterogeneous local properties.

Overall, chromatogram shape depends on the type of equilibrium isotherm, mass transfer kinetics and overall flow dynamics [5]. For some cases, it has been estimated

that as much as 70 % of the hydrodynamic dispersion in a column is caused by transcolumn heterogeneity [19]. Figure 3.6 shows three types of adsorption isotherms and their effect on the resulting chromatogram.

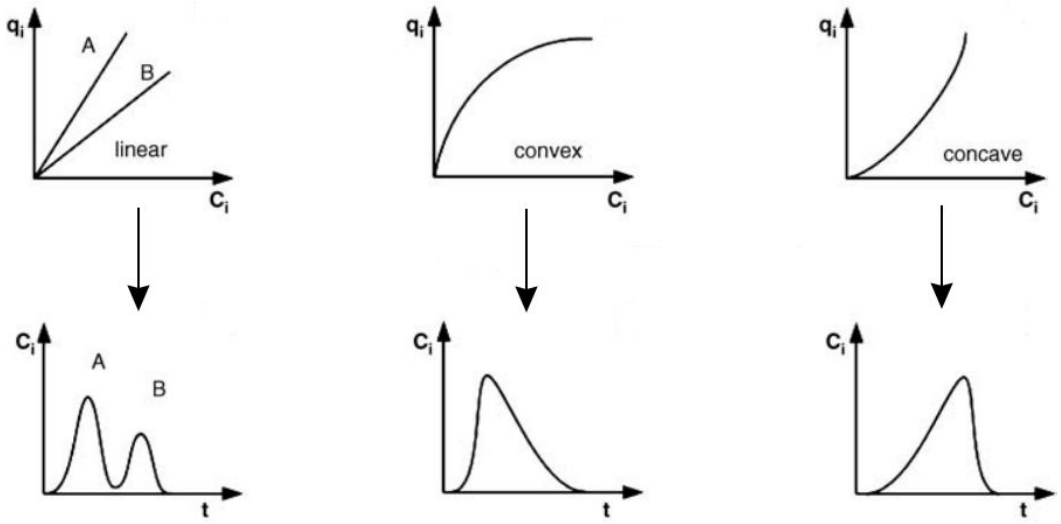

(a) (Top) Linear isotherm and (bottom) resulting chromatogram.

(b) (Top) Concave isotherm and (bottom) resulting chromatogram.

(c) (Top) Convex isotherm and (bottom) resulting chromatogram.

Fig. 3.6.: Adsorption isotherms and resulting chromatograms. q_i represents the loading of the solute i on the media at a concentration in the fluid c_i [5]. Final chromatogram shape depends on isotherm type and flow distribution.

Chromatogram shape indicates the dilution of the product elution fraction and peak shape is used to qualify the chromatographic performance through several characteristic values shown in the next section.

3.1.2. Chromatographic Performance

The plate number (N_C) of a chromatographic column with length L_C, and its corresponding Height of an Equivalent Theoretical Plate ($HETP$) calculated with Equation 3.4 are used to characterize packed columns and is a measure of overall column efficiency, being affected by fluid distribution heterogeneities, mass transfer and adsorption processes. Smaller plate heights correspond to higher efficiencies and to narrower peak widths approaching to the ideal rectangular profile of the initial injection. Narrower peaks imply an easier separation of different components and higher outlet concentrations. The aim of chromatographic parameters, extra-column equipment specifications

and packing methods is to obtain peaks as narrow as possible and HETP as small as possible [5].

$$HETP = \frac{L_C}{N_C} \tag{3.3}$$

The efficiency of preparative liquid chromatography columns is usually checked by introducing a non-interacting marker that is detected after elution with an appropriate detector (see Figure 3.7). Commonly employed tracers are 1 M NaCl detected by conductivity, and acetone (around 2 % v/v) detected by UV (280 nm) with an injection volume of ca. 2 % of the bed volume. The resulting chromatogram is then analyzed based on peak profile, HETP and asymmetry [5, 9, 10].

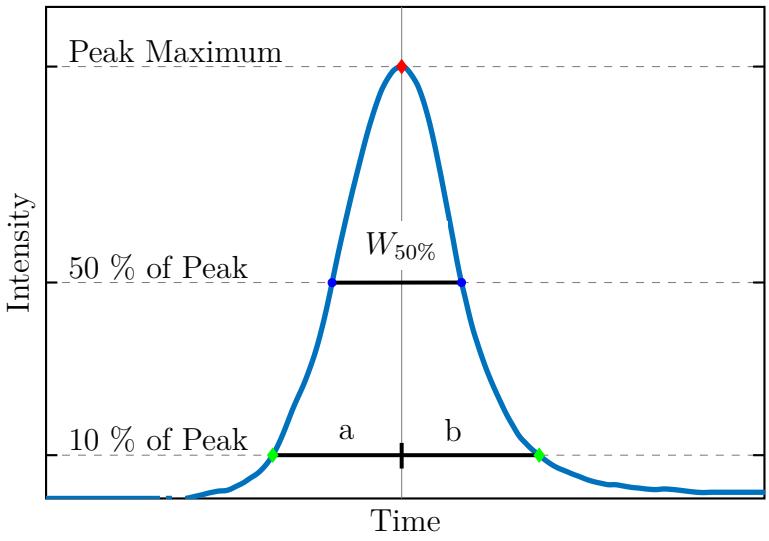

Fig. 3.7.: Computation of chromatogram characteristic values for calculation of HETP.

With the peak information, it is possible to calculate HETP with Equation 3.4. Where $W_{50\%}$ corresponds to the peak width at the 50 % level of the peak, and t_r to the elution time of the peak maximum. Both values are usually calculated in time units, or by multiplying by the employed flow rate, in volumetric units.

$$HETP = \frac{L_C}{5.54} \cdot \left(\frac{W_{50\%}}{t_r}\right)^2 \tag{3.4}$$

HETP has length units and it is commonly divided by the respective particle diameter to obtained the non-dimensional reduced HETP (rHETP)

$$rHETP = \frac{HETP}{d_P} \tag{3.5}$$

Although HETP groups all factors affecting efficiency together, it is possible to estimate the effect of individual factors on the broadening of the solute band with the van Deemter equation [27] as seen in Figure 3.8:

$$HETP = A + \frac{B}{V} + C \cdot V \tag{3.6}$$

Where V corresponds to either the interstitial u_{Int} or superficial velocity V_S according to

$$V_S = \frac{\dot{V}}{\pi \cdot (d_c/4)^2} \tag{3.7}$$

with $\dot{V}$ and d_c corresponding to the volumetric flow rate and column diameter respectively, and

$$u_{Int} = \frac{V_S}{\varepsilon} \tag{3.8}$$

A represents the eddy diffusion factor, affected by the structure of the packing. It depends on particle parameters such as size distribution and shape. Additionally, the way a column was packed determines also plays a role on this term. In the normal range of velocities of chromatographic columns this term remains constant.

B indicates the axial diffusion term, which depends on the molecular properties of each component. Higher velocities help diminish the influence of this factor.

C corresponds to the non-equilibrium factor, reflecting the mass transfer limitation of the process. As velocities are increased, there is less time for the thermodynamic equilibrium to be reached, and the influence of this term thus increases.

The optimal flow rate at which a chromatographic separation should be carried out from a theoretical point of view depends on the interaction of the different terms, with the ideal velocity being the minimum of the van Deemter curve seen in Figure 3.8

Other than rHETP minima, other parameters such as overall process time or loss of biological activity over time can determine that the optimal mobile phase velocity does not correspond to the Van Deemter minimum.

An additional measure of the packing is the asymmetry factor (As), which gives the ratio of the trailing portion to the fronting portion of the peak with the factors a and b obtained at the 10 % value of peak maximum (see Figure 3.7)

$$As = \frac{b}{a} \tag{3.9}$$

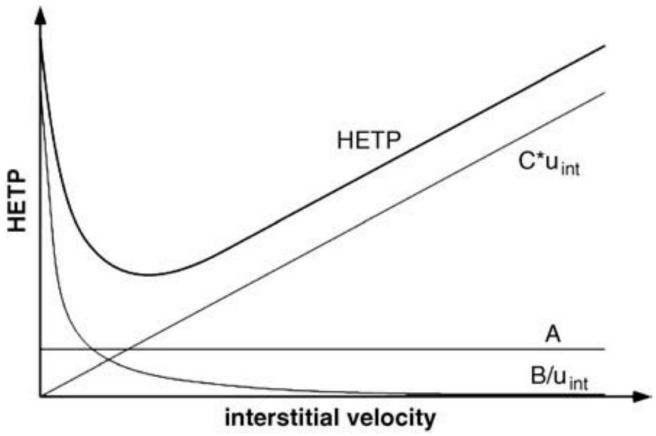

Fig. 3.8.: Van Deemter Curve with eddy diffusion, axial diffusion and non-equilibrium partial curves [5].

Beds with an heterogeneous structure will have marked tailing or fronting asymmetries. For example, channeling defects allow a portion of the mobile phase to flow out of the column before the bulk of the fluid, which would be apparent as a fronting asymmetry.

3.1.3. Chromatographic media

Chromatographic media consist in porous adsorbents to achieve larger loadability in comparison to non-porous materials. Loadability or capacity represents the amount of component that binds to the media per unit of volume. The overall mass transfer of the target component into the particle, and its posterior de-sorption, are defined by the surface chemistry of the media and goal molecule, and have a significant effect on overall band broadening. Particle pore size plays a role in the packing performance, and should be large to maximize pore diffusivity of the components [5], while particle porosity affects mechanical stability and capacity. Shape of the media can also impact column efficiency. It has been reported that in contrast to spherical particles, irregularly shaped media present more challenges during packing and consolidate into less dense packings [25].

Chromatographic particles can be divided in two distinct groups; inorganic solids and organic polymers. The former are characterized by relatively high densities and constant porosities, arising from their often rigid nature. In contrast, cross-linked organic polymeric particles are often compressible materials which deform under stress and exhibit a non-linear pressure-flow behavior. Furthermore, they commonly swell

or shrink depending on the employed mobile phase, and are characterized by low bulk densities [5]. Often used for analytical and preparative purposes in the life sciences [28], chromatographic processes based on polymeric media represent significant advantages for bioseparations: high selectivity, low shear rates, room temperature process, buffered solutions, among others [4].

Regardless of particle type, there are general requirements for ideal chromatographic particles. The matrix material should avoid non-specific interactions with target molecule, while having good mechanical and chemical properties to sustain cleaning-in-place and efficient working flow rates. Small particle diameter and narrow size distributions help diminish the A term in the Van Deemter equation by enabling the formation of a more homogeneous packing structure [4].

Among several factors, the mean pore size plays a defining role during the pore diffusion step of the mass transfer. Media can be tailored for a specific pore profile independently of its size. Figure 3.9 shows scanning electron microscopy (SEM) images of media commonly employed in biochromatography, each with distinct surface and pore characteristics. Ceramic hydroxyapatite (CHT) particles (seen in Figure 3.9a) belong to the inorganic solids group and are characterized by a relatively rougher surface caused by the sintering production process. Polymethylacrylate (PMA) (Figure 3.9b) and agarose (Figure 3.9c) particles are in comparison smoother. Particle characteristics of the media employed in this work are further explained in section 4.1.

Chromatography media are usually delivered and stored as a solid-in-liquid suspension. The manner in which this suspension is introduced into an empty column and forms the packed porous bed determines its structural homogeneity and is a fundamental step in the chromatographic process with implications on the final efficiency. Irrespective of particle type, chromatography mode or other process parameters, an efficient column requires a structure as homogeneous as possible.

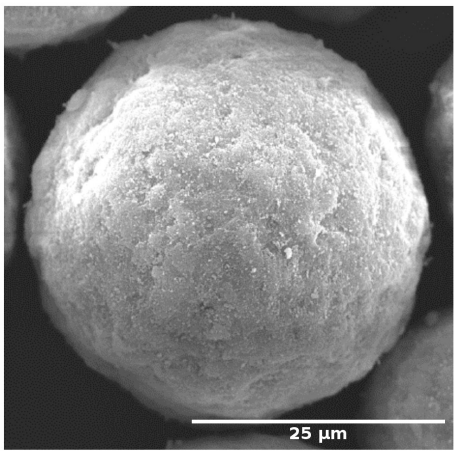

(a) SEM of a ceramic hydroxyapatite particle [29].

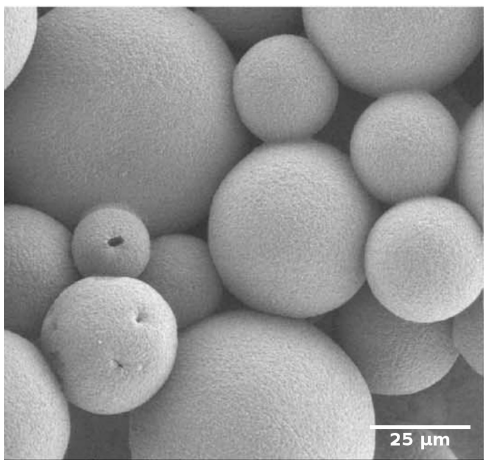

(b) SEM of polymethylacrylate particles [30].

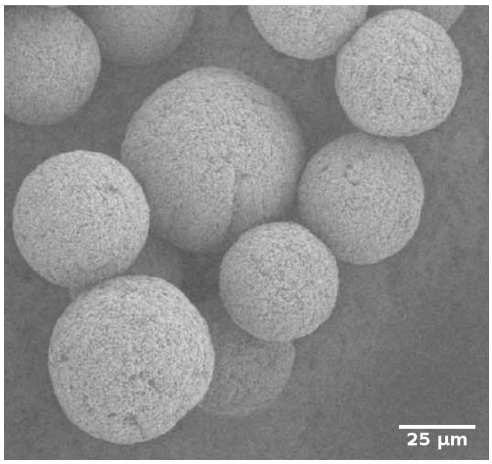

(c) SEM of agarose particles [30].

Fig. 3.9.: SEM images of commonly used biochromatography resins employed in this work.

3.2. Column packing

Column packing and its influence on bed structure has been under study since the start of modern chromatographic science [31]. Besides depending on intrinsic particle properties, packing involves a complex interaction of the different steps forming a packing protocol. Parameters and the order of discrete events such as packing under pressure, flow ramps, slurry concentration and any bed densification steps determine the final packing structure. An example of additional bed densification takes place during packing of compressible resins, which often includes a final mechanical compression step in which the plunger is driven into the bed. Although decreasing overall bed porosity, mostly only the top region is compacted, and the degree of compaction is a compromise between total void volume and column homogeneity. Due to their complexity and

empiricity, packing procedures are commonly kept a trade secret and described as an art rather than a science [19, 32, 33].

The first step during packing involves the insertion of the particle slurry into a prepared column. It is generally recommended to avoid slurry sedimentation, which occurs under Stokes's law [4]:

$$v_s = \frac{d_p^2 \cdot \Delta\rho \cdot g}{18 \cdot \eta} \tag{3.10}$$

Where d_p is the particle diameter, $\Delta\rho$ the density difference between particle and fluid, g the gravitational acceleration and η the dynamic viscosity of the fluid. Since most chromatographic media are not mono-dispersed, slurry sedimentation entails size segregation as larger particles fall faster and form the bottom-most region of a packing, while the top region contains the smaller particles.

The granular nature of chromatographic media plays a fundamental role during packing dynamics. The process of packing microscopic particles is characterized by dissipating interactions due to inelastic collisions, static friction and the athermal nature of the particles [34]. Above sizes of about 1 µm, the gravitational energy exceeds the energy behind thermal or Brownian motion, described by k_bT, where k_b corresponds to the Boltzmann constant, and T the system temperature [35]. Thus, microscopic particles do not exhibit thermal averaging and do not explore the phase space to reach the configuration corresponding to the global energy minimum.

Once they reach a local energetic minimum, they constitute a meta-stable structure sustained by a network of force-chains. Such granular packing is then denominated as "jammed", as it is caught in a small region of phase space and will behave as a static solid unless energy is supplied into the system [36]. The force-chains holding the packing depend both on the current state, as well as the history of the system. Figure 3.10 shows a 2-dimensional packing of photoelastic disks under bi-axial stress exhibiting force-chain networks [37]. The particles forming the chains preferentially carry forces across the packing, and can shield regions in the packing in which non-participating particles can move, and in which void spaces can take place and remain stable under packing compression. Thus, particle packings at rest and seemingly macroscopically homogeneous exhibit structural heterogeneities at the microscopic scale [38], which in the case of chromatographic beds, represent packing defects due to sample dilution in

void spaces and velocity gradients of the mobile phase.

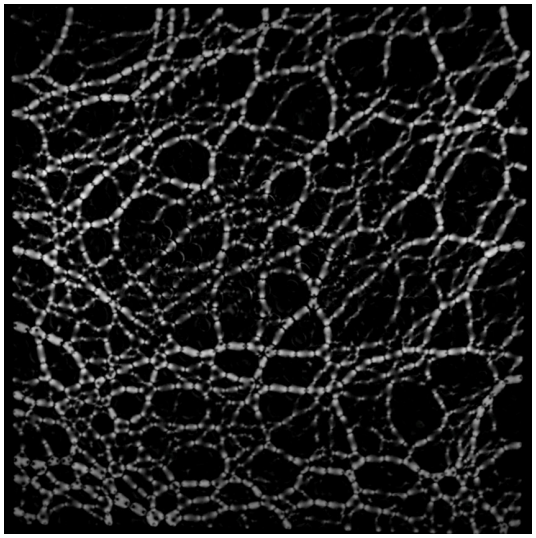

Fig. 3.10.: Force transmission in a 2-dimensional packing of photoelastic discs under bi-axial compression. Discs appear white under stress forming the observed force-chains 3. Dark regions do not participate in the force transmission along the packing [37].

Such inter-grain cooperativity to build stable force-chains comes from the presence of particle-particle friction, often modeled as a set of dash-pots, springs and sliders depending on model complexity and studied behavior (see Figure 3.11 for an example) [38]. When packing chromatographic columns, additional properties such as compressibility, swelling/shrinking and agglomeration also play a role.

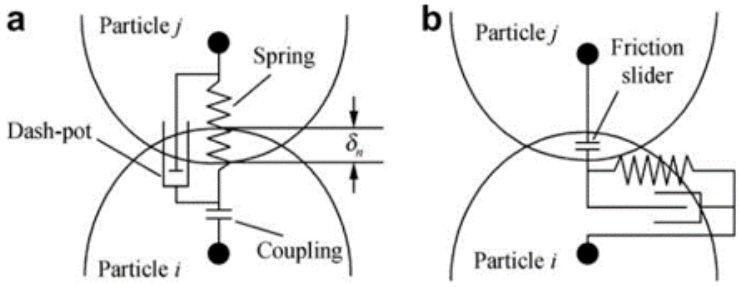

Fig. 3.11.: Modeling of the frictional contact between two particles divided into normal and tangential forces [39].

The effect of particle friction on chromatography packing has been previously studied. Smoother particles slip more easily over each other during packing, achieving a denser but more heterogeneous structure. In contrast, rougher media resisted movement under compression, delivering more homogeneous microstructures albeit with more void spaces [40].

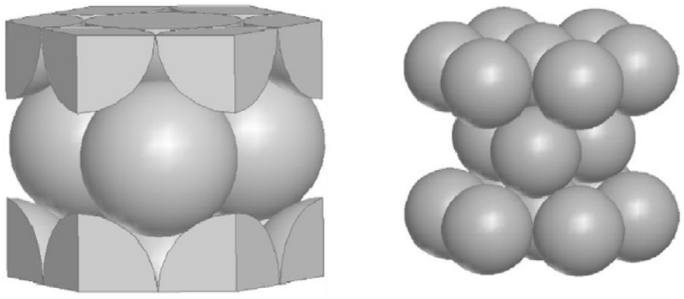

(a) Hexagonal close packed (HCP)

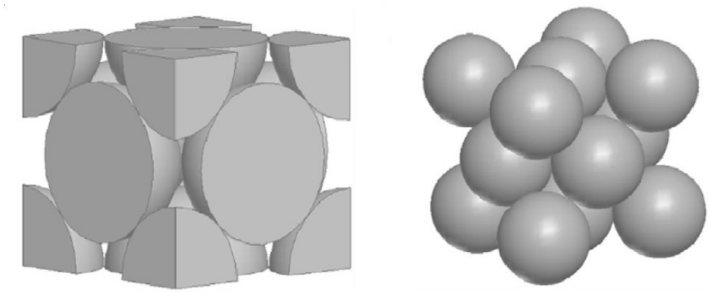

(b) Face centered cubic (FCC)

Fig. 3.12.: Particle crystalline arrangements of monodisperse spheres with minimal porosity [41].

While ideal entirely homogeneous packing configurations such as (hexagonal close packing) HCP or FCC (face centered cubic), seen in Figure 3.12, have a porosity of approximately 26 %, it is commonly accepted that porosities between 26 % and 48 % are actually reached in modern columns, with average porosities of approximately 37 % [5]. Packing density can give an assessment of the amount of packing defects in a bed and is used as the foremost criterion to evaluate column packing protocols [7]. A bed with a high porosity implies a large amount of void spaces in its structure and is often a result of low packing quality.

However, it has been determined that packing homogeneity has a larger effect on efficiency than global bed porosity. A heterogeneous distribution of void spaces along a column causes a high hydrodynamic dispersion which negatively affects column quality [7]. Computer simulations [8] and experiments [40] have suggested that it is then preferable to have an overall less dense column with homogeneously distributed voids than a denser packing in which voids are heterogeneously located.

In practice, the determination of structural homogeneity, void location and local porosities in packed columns is experimentally complex, specially at large column di-

ameters. Instead, macroscopic criteria are used to compare packed beds and packing methods. A common value for this is the achieved compression (λ):

$$\lambda = \frac{L_0 - L}{L_0} \tag{3.11}$$

Where L_0 denotes the initial or a standard bed height, for example gravity-settled height, and L the packed bed height. It can be related to the packing density using

$$\varepsilon = \frac{\varepsilon_0 - \lambda}{1 - \lambda} \tag{3.12}$$

Where ε_0 corresponds to the initial bed porosity.

Previous phenomena not only determine bed formation but also long-term bed stability and account for a commonly observed phenomenon in granular matter. Granular packings rest at jammed states, which may be distant from the most stable configuration [42]. At long time-scales, the packing undergoes structural relaxation, slowly becoming denser [34]. In practice in chromatography, this is often observed as the additional settling of a packed bed as it undergoes operation, transport or storage. As a chromatographic bed compacts in this manner, a gap between the top of the bed and flow distributor is formed, requiring lowering of the plunger or repacking of the bed to avoid dilution and backmixing of the feed mixture.

In general terms, packing chromatographic columns is a problem of granular densification, an area of interest for diverse industries. There have been several explored approaches such as thermal cycling [43], upward flow [44], wall oscillation [45], viscous flow packing, pressing [13], mechanical vibration [46] and ultrasound irradiation [47, 48]. More specifically, mechanical and ultrasonic vibration have seen extensive use in the compaction of soil in oil exploration and metallurgic industry, among others [18, 49, 50, 51, 52, 53].

3.2.1. Vibration packing

Unless perturbed by an external force, a packing will remain static through the frictional stabilization of the force-chains. External perturbations can unlock the structure, temporarily release force-chains and allow the densification of void spaces through particle rearrangement [46]. This approach has been theoretically proposed as a mean to minimize packing defects in chromatographic columns [8].

The mechanism shown in Figure 3.13a corresponds to a packing under vertical vibration, and describes the compaction initially taking place on the point nearest to the vibration. As the region is densified up to a maximum value, a compaction front rises through the bed until reaching the top. At this point in time, additional compaction will take place in logarithmic time asymptotically approaching a steady-state porosity. Figure 3.13b shows the evolution of the bed density, which is divided in two main stages. In the first one, the free surface of the packing is rapidly displaced as the compaction front rises. Compaction velocity in the second stage, after the front has reached the free surface, is much slower [54].

Packing compaction depends on vibration intensity. At low vibration amplitudes there is not enough energy to overcome frictional resistance. If vibration is too high, force-chain collapse is disorganized, particles acquire too much kinetic energy, and as many void spaces are formed as are destroyed during each vibration cycle, thus no overall densification takes place [38].

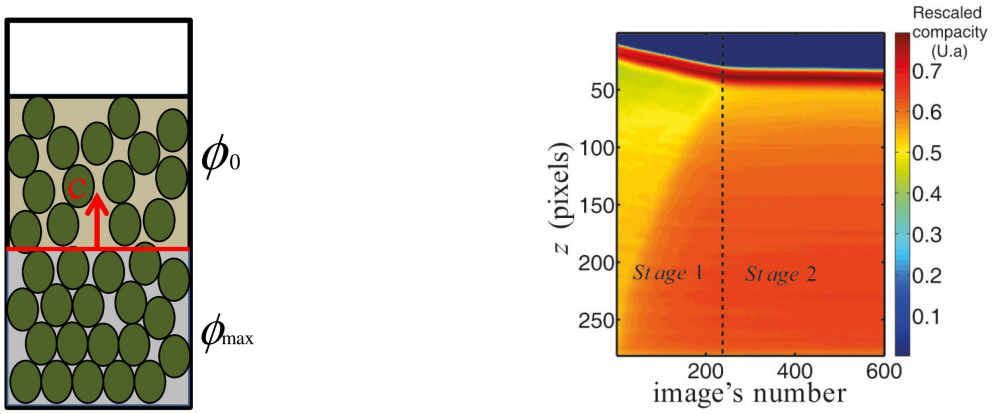

(a) Ascending compaction front caused by vertical vibrations.

(b) Change of packing density under vibration under time.

Fig. 3.13.: Evolution of a granular packing under vertical vibration on the bottom of the cylindrical container. The compaction front travels from the bottom to the top, increasing the solids-fraction (Equation 3.2) of the packing. [54].

Existing studies on the vibration-packing of chromatographic columns have focused on the limited case of particles with rigid and non-spherical shapes, like irregular silica or controlled pore glass [5, 55]. Both cases suggested the use of rotational vibrators attached to the bottom flange of the column to compress the packing (see Figure 3.14).

A process focused on the packing of controlled pore glass particles with vibration generated employing either one, two, or three turbine rotational vibrators simultaneously on a 450 mm column was patented [55]. It was found that vibration delivered

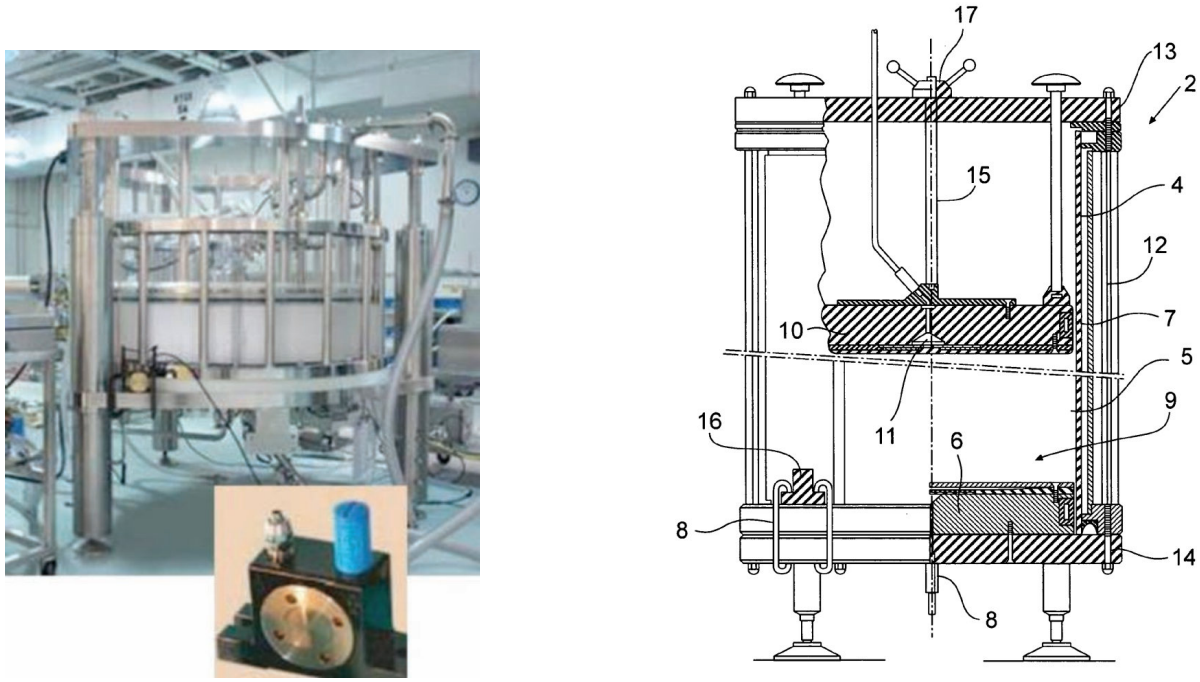

(a) Turbine rotational vibrator clamped to column flange for packing of irregular silica or controlled pore glass [5].

(b) Patent on multiple rotational vibrators for the packing or irregular glass particles [55].

Fig. 3.14.: Vibration packing has so far only been explored for rigid irregular media.

columns with lower rHETP in all cases. The more vibrators, the lower the rHETP. Even packings first consolidated under gravity settling and compacted under vibration showed a higher efficiency than flow-packed columns.

3.2.2. Ultrasound during packing

Ultrasound

Ultrasound is a disturbance moving as a pressure wave (see Figure 3.15) through a medium at a frequency larger than 20 kHz.

Common applications include ultrasonic imaging in medicine [56] or material science employing low-intensity ultrasound, versions of which have been used to monitor the state of chromatographic columns [57]. High intensity ultrasound can be used to disperse particles or disrupt cells through cavitation. Other applications include densification of green bodies in metallurgy and ultrasonic friction welding.

Ultrasound is most often generated using transducers based on the piezoeletric effect, which consists of the expansion and contraction of a material under an electric charge

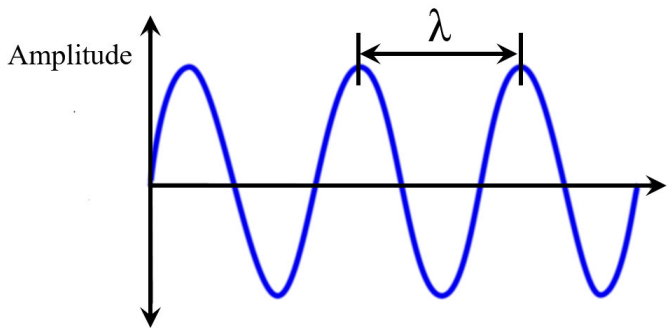

Fig. 3.15.: Profile of a wave. Amplitude can describe local density or pressure. λ denotes wavelength.

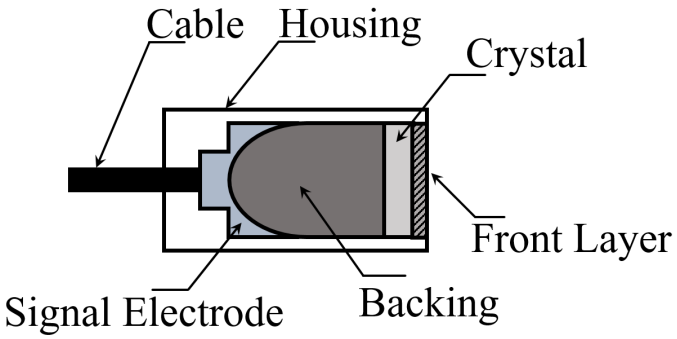

Fig. 3.16.: Schematic ultrasound transducer construction.

[58]. For this, ceramic crystals are commonly employed in the configuration shown in Figure 3.16). The form and dimensions of the crystal are chosen according to the frequency to be generated and application, with disk or ring-like shapes being the most common. The thickness of the crystal is most usually $\lambda/2$ (Figure 3.15) of the target frequency to achieve acoustic resonance [58], meaning that higher frequency transducers have thinner crystals and are often mechanically weaker than low frequency ones. To protect the crystal from physical and chemical elements, a layer is often attached to the front, which can also function to improve wave transmission to the medium [59] according to equation:

$$R = \left(\frac{Z_0 - Z_1}{Z_0 + Z_1} \right)^2 \tag{3.13}$$

Where R denotes the degree of wave reflection at the interface between two materials with different acoustic impedances (Z_0 and Z_1). Gases and fluids have low impedances ($Z_{Water} = 1.5 \quad MRayl$) in comparison to solids ($Z_{Steel} = 46.9 \quad MRayl$). The choice

of front material is a compromise between reflectance and stability, as solids with low impedances, such as doped polymers, silicones or epoxies lack the chemical and physical resistance of metals [60].

The backing material regulates the damping of the wave and determines whether the transducer has a lower amplitude over a wide range of frequencies, or delivers high-intensity waves at a specific frequency vale (see Figure 3.17).

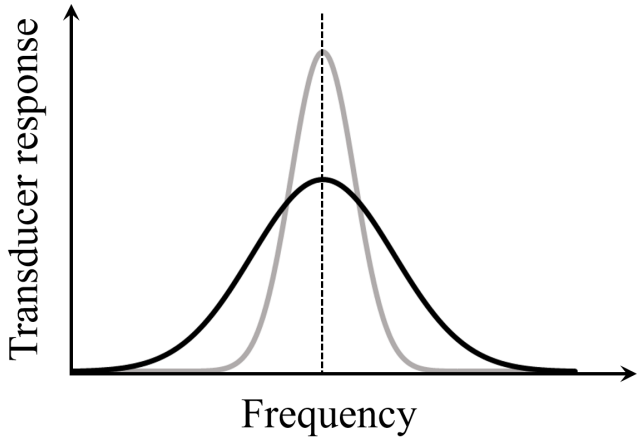

Fig. 3.17.: Backing material in a transducer determines whether it has a wide-bandwidth and low intensity (black line), or high intensity in a limited frequency range (gray line).

High-amplitude ultrasound can influence granular matter through different mechanisms. If a consolidated packing is subjected to ultrasound, the waves behave similarly as with mechanical vibration, causing a compaction of the structure through force-chain breakage and particle movement [47]. If there is a slurry of non-contacting particles in an ultrasonic field, other effects take place: acoustic radiation forces and acoustic streaming.

The propagation of pressure waves arises from the small but non-zero compressibility of the propagation medium. By solving the compressible Navier-Stokes equation with a high-frequency pressure source it is possible to calculate the resulting first order (nanosecond time-scale) pressure field. In the case that the geometry and acoustic properties of the system result in a resonant field, it is possible to calculate a second order (microseconds time-scale) field. For a particle in the resulting acoustic field, it is then possible to calculate an acoustic potential (equation 3.15) and with it, the acoustic radiation forces acting on the particle [61, 62].

$$F^{Rad} = -\nabla U^{Rad} \tag{3.14}$$

$$U^{Rad} = \frac{4\pi}{3}a^3\Big[f_1\frac{1}{2}K_0\langle P^2\rangle - f_2\frac{3}{4}\rho_0\langle v^2\rangle\Big] \tag{3.15}$$

The magnitude of the forces depends on the acoustic potential, which depends on the intensity of the acoustic field as well as particle and medium properties (a , f_1 and f_2 in Equation 3.15 [61]). In general terms, the more different a particle is in comparison to the surrounding media in density and impedance, the stronger will it be affected by the acoustic field. Acoustic radiation forces are commonly used for the acoustophoretic motion of particles and cells through frequency modulation [63]. This however is done for diluted suspensions, since transducers with the required bandwidth are usually too weak to handle dense suspensions or consolidated packings due to the bandwidth-intensity trade-off explained in Figure 3.17.

Acoustic streaming also occurs in an ultrasonic field, and depending on the geometry of the system and ultrasound properties, several types can be defined [64]. The most relevant in this work is Eckart streaming, which arises from the attenuation of sound waves as these propagate in the medium. The front of the transducer forms a high pressure zone. As acoustic energy diminishes along its trajectory, zones of low pressure are formed. Thus a net flow takes place from high to low pressure regions.

Use of ultrasound for column packing

Ultrasound has been previously employed during the packing of chromatographic columns. Most approaches can be divided in two groups: the first one uses it to disperse the particle slurry and keep it homogeneously suspended in an external container before it enters the column itself, as shown schematically in Figure 3.18. An ultrasonic horn is inserted from the top into a chamber through which the particle slurry travels before exiting through a bottom port into the column. A well mixed suspension ensures a homogeneous distribution of particles of different sizes in the solution. Furthermore, prevention of agglomeration and breakage of clumps can potentially improve packing.

The second approach employs common ultrasonic baths during packing, a setup shown in Figure 3.19. Packing under ultrasonic irradiation has been studied for capillaries in the micrometer range [53, 66] up to 4.6 mm in diameter [20], and in lab-on-chip devices at the micrometer scale [67]. Some authors found that denser, more efficient and stable columns could be packed with ultrasound, while others found that the column

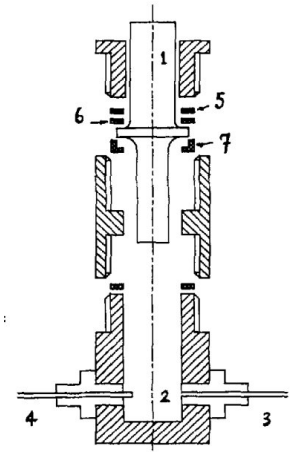

Fig. 3.18.: Ultrasonic transducer used for the dispersion of chromatographic slurry before packing [65].

could settle heterogeneously and become inhomogeneous [20]. Moreover, while some authors carried out a simultaneous ultrasound irradiation of the capillaries with flow packing [19, 66], others separated both steps [53].

An advantage of this approach is the considerable power-to-volume ratio (approximately $1 \cdot 10^6$ $^{\text{Watt}}/_{\text{l}}$) that can be achieved due to the small volume of the capillary. Furthermore, ultrasonic waves enter the column from all directions and can be assumed not to be considerably attenuated by the packing due to its small volume, resulting in an homogeneous vibration of the entire structure.

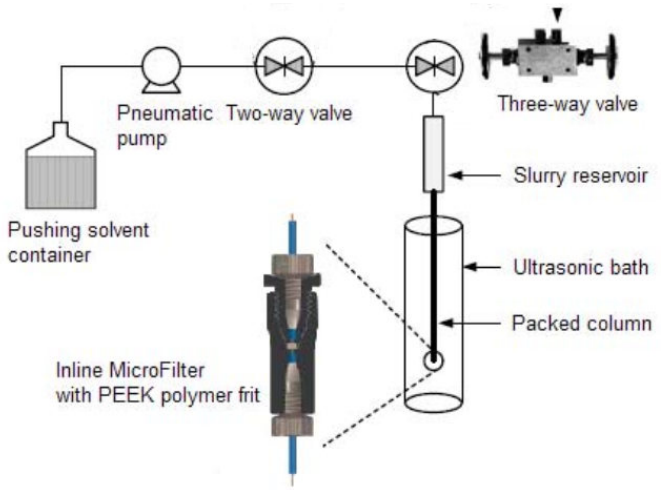

Fig. 3.19.: Approach to packing chromatographic capillaries under ultrasound [68].

While adequate for thin capillaries which can be bent to fit into the bath volume,

this approach is limited for longer, wider and rigid columns employed for preparative purposes. Moreover, most ultrasonic baths employ transducers in the range between 20 - 80 kHz, which makes them prone to generate inertial cavitation if the ultrasonic power is increased to compensate for larger column volumes. These frequencies, while useful for cleaning which is the original purpose of these baths, can also result in particle damage or breakage. Figure 3.20 shows the pressure threshold at which cavitation can take place depending on the ultrasound frequency when the medium is water. Under the curve, acoustic pressure is not strong enough to generate inertial cavitation.

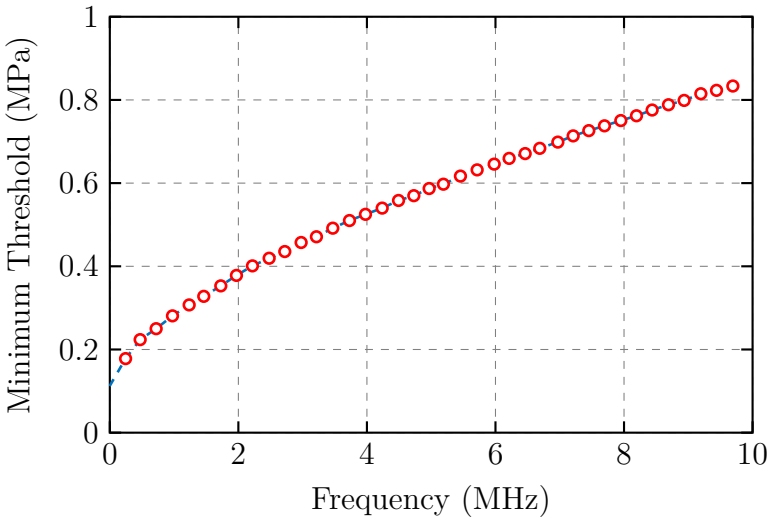

Fig. 3.20.: Measured pressure threshold above which cavitation can take place as a function of ultrasonic frequency (reproduced from [69])

3.3. 3-dimensional reconstruction of chromatography columns

It has been previously established that the microstructure of the particle packing plays a critical role in the efficiency of chromatographic columns [17], affecting the fluid dynamics inside the column and overall process mass transfer (see Figure 3.21 for a schematic of involved phenomena).

The need for real structural data of packed columns has been partially fulfilled through the use of diverse optical methods [6, 17]. These techniques were developed for the imaging and reconstruction of silica based media [70], and cannot be applied for particles conventionally employed in biochromatography, which are mostly based

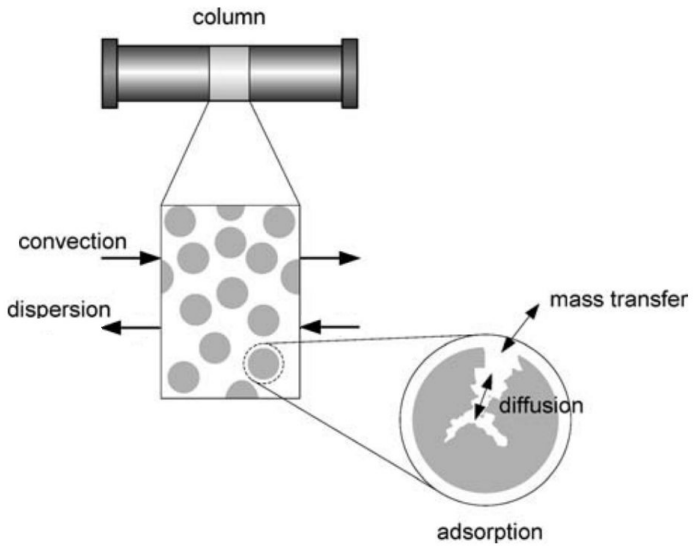

Fig. 3.21.: Overview of solute mass transfer phenomena in a chromatography packed column [5]. For a general model of chromatography it is necessary to know the exact geometry of the packed bed at the microscopic level.

on organic polymers. Although impressive resolutions in the order of nanometers can be achieved, optical methods can only be carried out in systems in which the refractive indexes of the packing, column, mobile phase and optical equipment can be matched and are optically clear, severely limiting material choice. There is currently no imaging method that can be employed for the reconstruction of packed columns used in biochromatography or packings contained in opaque columns.

3.3.1. X-ray computed tomography

X-ray computed tomography is an imaging technique widely employed across several sectors such as hydrology, petroleum engineering, soil science, etc. [71, 72]. It is characterized by being versatile, robust and non-destructive. It is often used for the reconstruction of microscopic porous samples to study flow properties [71, 73]. It permits a non-destructive measurement of non-clear samples and is able to reconstruct 3-dimensional data of the material. Several micro-CT layouts exists, with some where the sensor array rotates around the material to be measured, or where X-ray lenses focus the X-rays similarly to optical lenses in order to obtain higher resolutions. A layout where the X-ray source and detector remain stationary and the sample rotates can be seen in Figure 3.22.

The measurement principle of micro-CT is based on the interaction of high energy

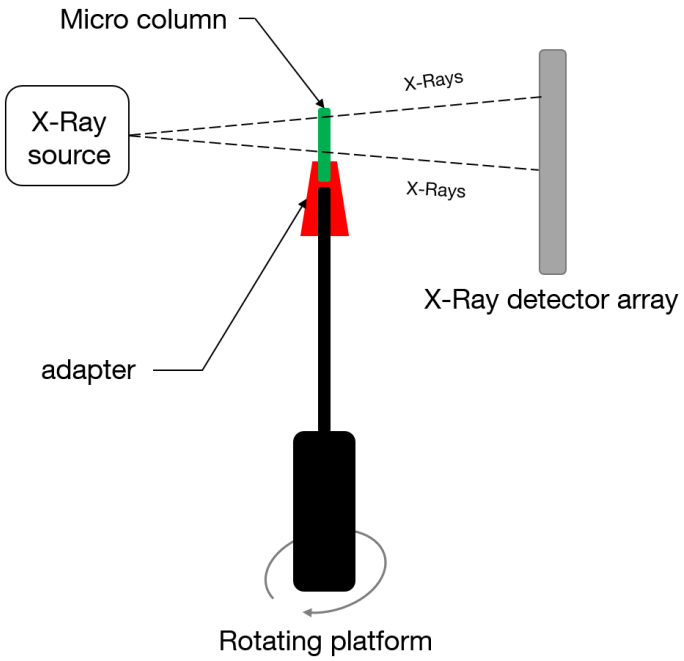

Fig. 3.22.: Schematic of the employed X-ray computer tomography system. The sample (green) is held in place with an adapter. The sample holder (black) is attached to a rotating platform which makes a revolution per measurement. As the sample rotates, the X-ray absorption is measured by a 2-dimensional sensor array. Form these the 3-dimensional data can be obtained through a tomographic function.

photons with the atoms in the material, and the measurement of the radiation after attenuation. X-rays act on matter as an electromagnetic wave, with the dominating phenomenon depending on the photon energy level of the rays. At high energy levels between 5 - 10 MeV, the attenuation is dominated by Compton scattering while at lower energy levels (50 - 100 keV), the attenuation depends mostly on photoelectric absorption [71]. Commonly, industrial X-ray tomography equipment work at the lower energy level. It is then a reconstruction technique based on the different absorption properties of dissimilar materials and the contrast in the measured attenuated rays. Materials composed of high atomic numbers (Z) usually have high X-ray absorption properties compared to lighter atoms [71]. Specially in the case of samples composed of water, air, and organic materials, the low absorption characteristics make it challenging to distinguish individual components.

The main obstacle for the use of X-ray CT for reconstruction of chromatographic columns lies on the lack of contrast between the highly porous chromatographic beads and the inter-particle voids filled with the mobile phase [74]. The particles hold a significant amount of the surrounding liquid phase inside their internal structure [75],

and the atoms composing the matrix usually have low atomic numbers, since these are often organic polymers (Z = 8, 6, 1, for oxygen, carbon and hydrogen, respectively).

X-ray micro-CT has been previously used for the 3-dimensional measurement of cellulose- and ceramic-based chromatography packings [74]. The authors focused on the variation of X-ray parameters and explored different energy levels between 60 - 225 KeV, exposure times between 0.254 - 1 s, radiating filaments, and two different X-ray tomographic equipment. The ceramic packing could be reconstructed in both employed tomographic machines using optimized radiation parameters. A tomographic slice of a capillary packed with the cellulose-based material can be seen in Figure 3.23. This capillary could however only be measured with one of the tomographic instruments even with the optimized X-ray parameters, due to the low attenuation of the low atomic number material.

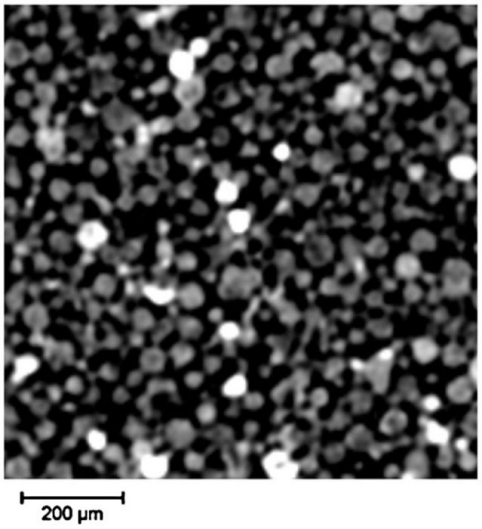

Fig. 3.23.: Tomographic image of biochromatography cellulose media [74]

A second approach is the measurement of columns at resolution scales larger than individual particles [76, 77]. With this technique, it is possible to obtain local column properties such as porosity, homogeneity and hydrodynamic dispersion. Moreover, it is also possible to inject a pulse of a radiocontrast agent and measure its concentration as it breaks through the column. This information can be then used to calculate the efficiency of the column. Another possibility is to include measured macroscopic porosity properties in CFD simulations, and compare these with experimental values. However, following this technique individual particles remain unresolved and the microstructure cannot be derived.

4. Materials and Methods

4.1. Chromatographic media and mobile phases

All media employed during this entire work are listed below. Each individual section states which specific particle was used.

Toyopearl SP 650 M (Tosoh Bioscience GmbH, Stuttgart, Germany) is a strong cation exchange resin with a porous polymethacrylate base matrix with a functionalized sulfopropyl ($-CH_2-CH_2-CH_2-SO_3$). It has a mean particle diameter of 65 µm, mean pore size of 100 nm and an internal porosity of 63% [75]. It is a compressible media employed for biomolecule purification with chemical stability in the pH range between 2 - 13. Due to its compressibility it has a non-linear pressure-flow behavior, and is rated to a work pressure of up to 3 bar or superficial velocities of up to 1000 $^{cm}/_{h}$. The storage and packing buffer were 10 mM NaOH in de-ioinized (DI) water to prevent microbial growth.

Capto Q ImpRes and CM Sepharose 6 FF particles were obtained from GE Healthcare GmbH (Munich, Germany). Capto Q ImpRes is a strong anion exchange resin commonly employed during intermediate purification and polishing in biomolecule production. It has an agarose base matrix with a quaternary amine ligand ($-CH_2-N-(CH_3)_3$), and a mean particle diameter of 40 µm. There is no published data on its intraparticle porosity. However, similar agarose-based resins such as the Sepharose series have been reported to have an internal porosity in the range of $79 - 84\%$ [78]. Recommended maximal work pressure and flow rates are 3 bar and 300 $^{cm}/_{h}$, respectively.

CM Sepharose 6 FF is a weak cation exchanger designed for the steps of capture and intermediate purification of proteins. Its matrix is composed of a 6% cross-linked agarose matrix and carboxymethyl groups ($-O-CH_2-COO^-$) as ligands. It is a compressible media and is rated for velocities up to 700 $^{cm}/_{h}$. The mean particle diameter is 90 µm. The storage buffer was an aqueous solution of 20 % ethanol to prevent microbial growth, and the packing buffer was 10 mM NaOH.

Ceramic hydroxyapatite (CHT) particles were obtained from Bio-Rad Laboratories

GmbH (Munich, Germany). CHT is an incompressible mixed-mode chromatography media made of a spherical, macroporous form of hydroxyapatite. Sample interaction is modulated by two types of binding sites; phosphate groups interact with the sample through cation exchange while calcium groups interact through metal affinity. In this work, CHT particles a mean particle diameter of 40 µm were used. CHT media is delivered and stored in dry state before use. A working buffer of 500 mM NaOH and 50 mM NaH_2PO_4 was used.

Sodium di-hydrogen phosphate monohydrate were purchased from Carl Roth GmbH & Co. (Karlsruhe, Germany). Sodium hydroxide was acquired from NeoFroxx GmbH (Einhausen, Germany).

4.2. Ultrasound equipment

Ultrasonic waves were generated with an ultrasonic transducer type E/805/T/M/S powered by a signal generator type MFG (Meinhard Ultraschalltechnik GmbH, Leipzig,Germany). The transducer had a stainless steel active face with a diameter of 15 mm (see Figure 4.1). Its resonant frequencies were 835, 1350 and 2500 kHz and the signal generator was set up to deliver a maximal power of 125 Watt. The frequency with the highest measured acoustic intensity was 837 kHz which was used for all experiments.
Besides a constant signal and frequency, the generator can also deliver sweeping signals. These consists of the continuous change of frequency in a pre-determined range, and is the basis of several ultrasound-based acoustophoretic motion methods (see Section 3.2.2). It is also possible to generate pulse signals, consisting in the turning on and off of the ultrasound at determined time intervals.

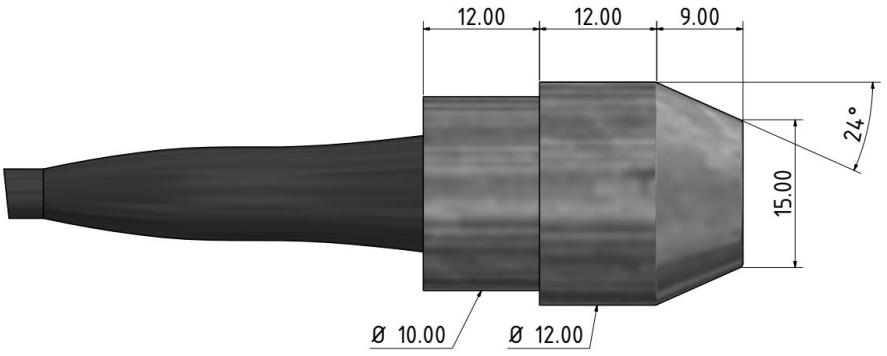

Fig. 4.1.: Dimensions of employed ultrasonic transducer. Body and active face made of stainless steel. All units in millimeters.

The active area of the ultrasound transducer is made of chemically inert stainless steel. This enables a direct contact with the mobile phase, but causes high acoustic reflection at the steel-water interface due to the difference in acoustic impedances, Z = 1.5 MRayl and Z = 46.9 MRayl for water and steel respectively [79]. Wave reflection is given by Equation 3.13 and amounts to 88 % of the ultrasonic wave in this case, in which the transducer was built to be chemically and physically robust at the cost of acoustic efficiency.

4.3. Pneumatic vibrators

Vibrators type K-8, FP-12-S and FP-35-S were acquired from Aldak Vibrationstechnik (Troisdorf, Germany). Industrial pneumatic vibrators operate with pressurized air between 2 - 6 bar. The vibrators were run with pressurized air which was first filtered through a bronze-sinter with a 50 µm pore size, and lubricated with a mist oiler. Pressure was controlled with a precision valve. When using more than one vibrator at a time, the air line was divided as near as possible to the vibrators, with each end having the same elements to guarantee equal air distribution.

4.3.1. Rotational ball vibrators

K-8 is a ball-type vibrator based on the rotational movement of a steel ball along a circular guide. Vibrations arise from the centrifugal force of the rotating mass (see Figure 4.2).

(a) Employed K-8 ball vibrator.

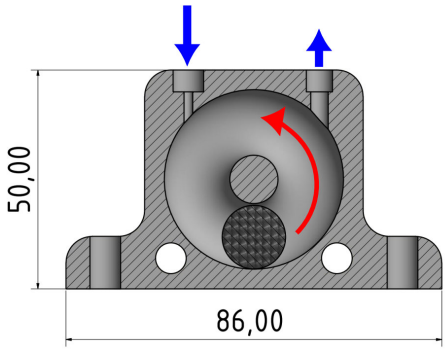

(b) Internal arrangement of ball vibrators. Rotation of the steel ball generates the vibration.

Fig. 4.2.: Rotational vibrator. Internal detail of vibrator shows vibration principle, which causes the non-perpendicular wave propagation from the active face.

Rotational vibrators usually operate at higher frequencies and forces than linear vibrators of comparable size, and require comparatively larger air volumes to function. Commonly employed for gravity-assisted chute flow and clean outs, the tangential element of the vibrations can also be used to assist by directing flow in direction of rotation [80]. Ball vibrators are usually noisier and less efficient than other types of pneumatic vibrators.

4.3.2. Linear piston vibrators

FP-12-S and FP-35-S piston vibrators generate purely linear vibrations by the vertical movement of an oscillating piston inside the vibrator housing (see Figure 4.3). Air entering the vibrator accelerates the piston, which is propulsed to one of the ends. As it approaches, a pocket of pressurized air decelerates the mass and accelerates it towards the other end, where the process repeats itself. As a result, the vibration has a sinusoidal profile which propagates perpendicularly from the active face.

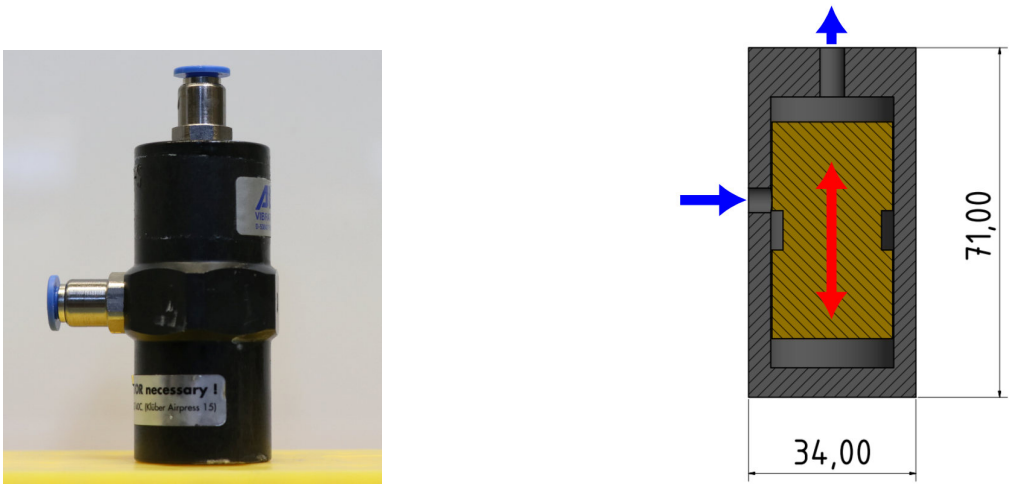

(a) FP-12-S vibrator with intake and venting ports.

(b) The moving mass oscillates between both ends of the housing

Fig. 4.3.: Linear vibrator. Internal detail of vibrator shows the oscillating mass and its movement direction.

Piston vibrators are commonly employed for hopper flow or lower angle chutes. Due to the air cushion principle which forgoes the extra force of impacts, their frequencies and forces are reduced in comparison to other vibrators of similar size [80]. These vibrators require less air volume to operate, are more efficient and generate less noise.

4.3.3. Vibrator characteristics

The basis for the choice of vibrators (listed in Table 4.1) were the force to bed volume ratios available in the literature (listed in Table 4.2). Vibrators were chosen so that these values were well within the range of forces in our setup, taking into account the available forces at different air pressures. The second criterion were the vibrators'

Vibrator	**2 bar**			**6 bar**		
	Freq (Hz)	Force (N)	Air use ($^{l}/_{min}$)	Freq (Hz)	Force (N)	Air use ($^{l}/_{min}$)
K-8	425	130	83	583	360	195
FP-12-S	103.3	34	0.8	155	92	25
FP-35-S	63	294	23	97	1038	162

Table 4.1.: Parameters of employed vibrators.

dimensions, which determine the possibility of attaching the vibrators to the columns.

Column (Diameter, H/D)	**Vibrator(s) configuration**	**Vibration characteristics**	
		Freq (Hz)	Force-ratio (N/l)
400 mm, $H/D = 0.5$ [81]	OT16, **6 bar**	350	105
1000 mm, $H/D = 0.5$, estimated from [5]	4x OLI OR65, **6 bar**	316	100
50 mm, $H/D = 0.5$	FP-12-S, **2 bar**	103	692
50 mm, $H/D = 2$	K-8, **2 bar**	416	662
200 mm, $H/D = 0.5$	4x FP-35-S, **2 bar**	100	374
400 mm, $H/D = 0.5$	4x FP-35-S, **6 bar**	100	165

Table 4.2.: Combination of bed volumes and employed vibrator configurations. The first two items correspond to reported setups in the literature. Our own configurations employed at the institute of biochemical engineering and at the research center for industrial biotechnology (FZWB) are located on the bottom.

4.4. Chromatographic set-ups

4.4.1. 50 mm column

Custom-built chromatography columns were used for all 50 mm experiments (Figure 4.4 shows the standard column configuration). A polymethylmethacrylate cylinder was used as the main body of the column with flow distributors machined from stainless steel fitted with stainless steel frits with a mean pore size of 8 µm (Tridelta Siperm GmbH, Dortmund, Germany) to retain the particles. O-Rings were placed in the distributors, acting as moving seals with the column. The column was kept in place using one disc at each end fastened to each other with M5 threaded rods. The column could be configured so that one or both of the distributors could be moved (Figure 4.4 shows a movable top distributor). This was achieved employing a trapezoidal screw and nut system, in which the screw was kept in place with an indentation, guaranteeing that there was no rotation as the assembly moved vertically.

Each flow distributor had a M6 port which was used to fasten HPLC fittings and connect the column to the hydraulic circuit. The bottom disc had openings for the

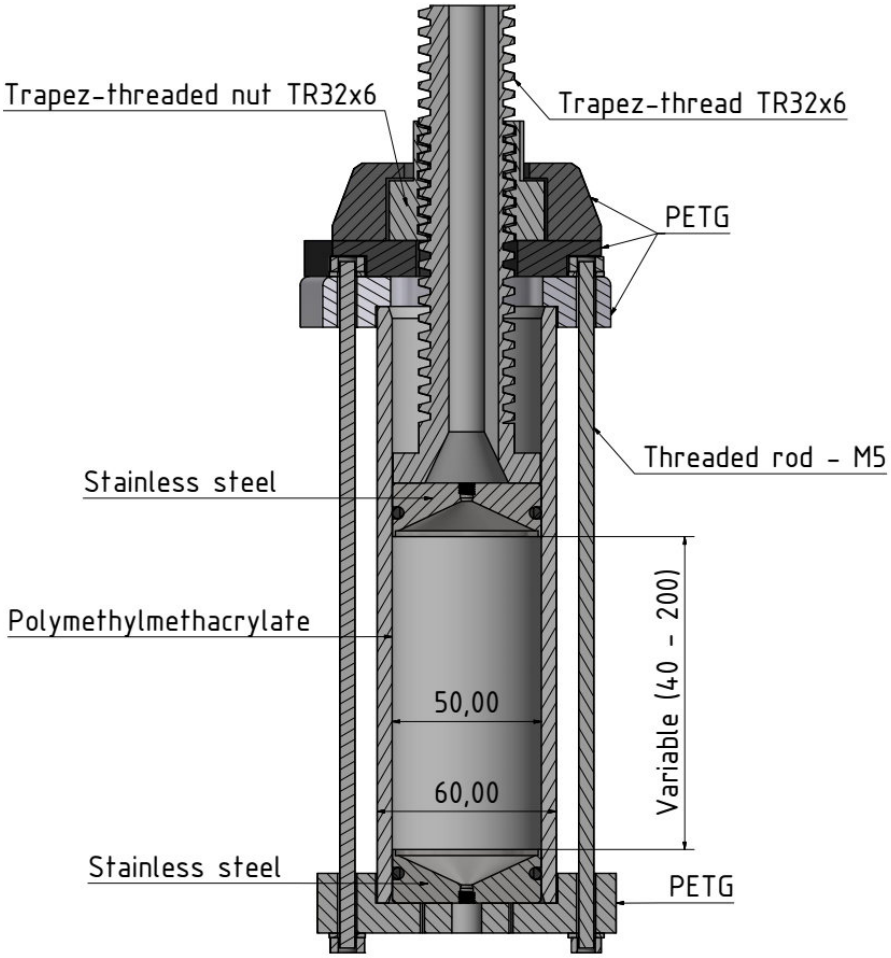

Fig. 4.4.: Schematic drawing of a custom built chromatographic column with movable top flow distributor.

attachment of the steel clamp used during linear vibration experiments (detailed in Figure 4.7a). All 3D-printed parts were printed with PETG and the setup was able to withstand pressures of up to 4 bar.

All solutions were kept in a KISS K25 bath thermostat (Huber Kältemaschinenbau AG, Offenburg, Germany) at 25°C. Flow after the pump was directed in the thermostat with a spiral tubing to further guarantee that flow temperature was regulated. The height of sedimenting slurries and the compression behavior of the chromatographic beds were tracked by photographs taken with a Canon EOS 80D equipped with a Canon EF 100/2.8 L IS Macro USM objective. The images were calibrated using markings on the column of known length and analyzed using MATLAB 2017b.

A computer-controlled precision gear pump (Micropump GB-P25.JVS.A, Idex Health

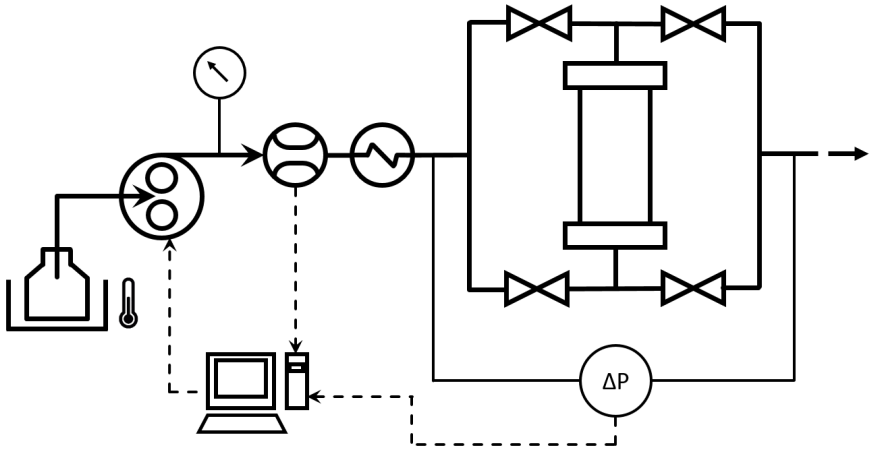

Fig. 4.5.: Diagram of the hydraulic setup employed for the packing of the 50 mm columns.

& Science, Oak Harbor, WA, USA) was employed for beds re-suspension and packing. Flow was controlled with a PID control system implemented in LabView (National Instruments, Austin, Texas) which enabled the setting of either a pressure drop or flow rate profile. Flow rate was measured with an in-line inductive flow meter (Promag 60 H, Endress+Hauser, Weil am Rhein, Germany). All elements of the control circuit were connected to the computer with an USB-6008 data acquisition interface from National Instruments (Munich, Germany).

Flow distributor with ultrasound transducer

The ultrasound transducer was coupled to the column using a custom flow distributor machined from stainless steel (detail in Figure 4.6). The transducer was placed in the distributor and in direct contact with the interior of the column. The area between the tapering of the transducer and the inner face of the housing was sealed with an o-ring. The transducer was kept in place with a nut which had an opening to allow the electric lines to reach the signal generator.

Mobile phase flowed through the ring-shaped section of the distributor around the central area. A ring-shaped stainless steel frit was fitted to retain the particles. Flow was collected through three M5 ports with attached HPLC fittings connecting the column to the hydraulic circuit.

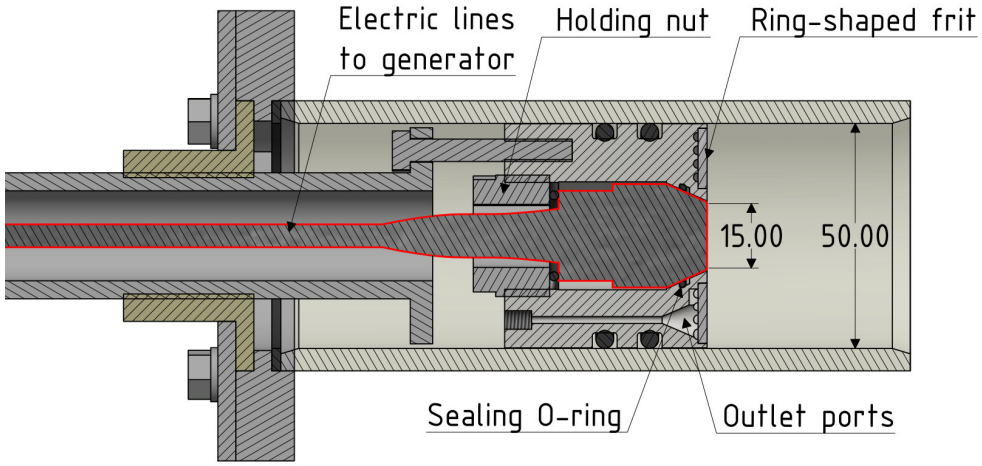

Fig. 4.6.: Schematic drawing of the built flow distributor with ultrasound transducer in its center.

Attachment of vibrators

The vibrators were attached either vertically or horizontally. Vertical vibration was accomplished with a steel bracket directly fastened to the bottom flow distributor (Figure 4.7a). The bracket had openings to which either two FP-12-S or one K-8 vibrator could be attached.

For the vertical case, PMMA clamps were machined so that these could be tightly fastened to the exterior of the column (Figure 4.7b). Vibrators could be attached to the clamps using screws previously tapped into them. The clamps were designed to maximize contact area and avoid gaps with the column.

For both cases, the material of the fastening element was chosen as to minimize energy losses with the column element at which it was attached according to Equation 3.13.

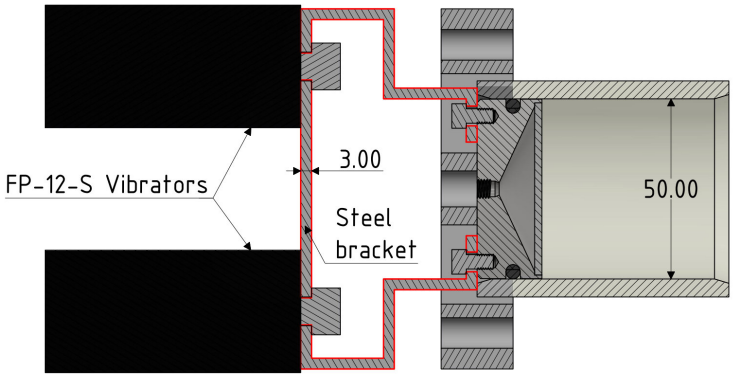

(a) Attachment of two FP-12-S vibrators to the bottom flow distributor with a steel bracket.

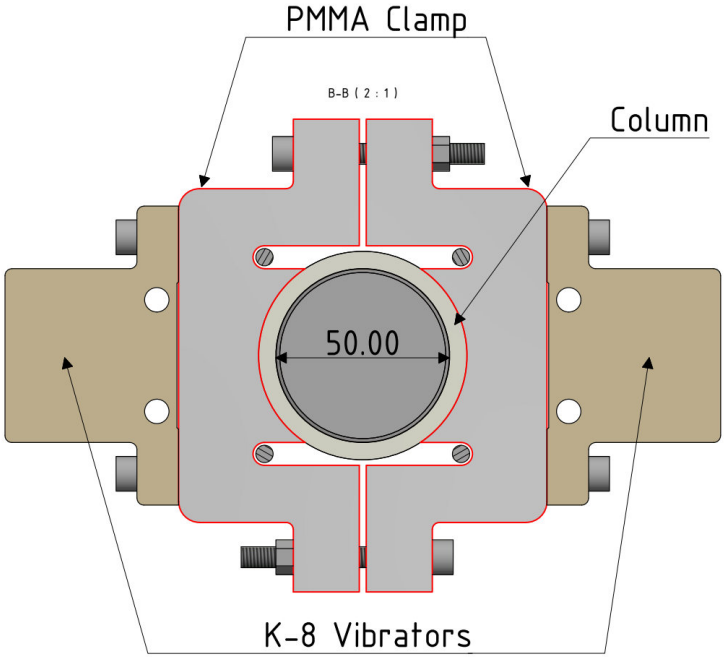

(b) Two K-8 vibrators attached horizontally to the column with two PMMA clamps.

Fig. 4.7.: Mechanical elements for the generation of lateral and vertical vibration in a 50 mm column.

Pulse experiments for the 50 mm column

For the 50 mm column, acetone (Carl Roth GmbH, Karlsruhe, Germany) was used as the tracer substance. An aqueous solution of 2 % $^{v}/_{v}$ acetone [9, 10] in the respective media working solution was injected into the packing using an injection loop with a constant volume of $\sim$ 2 % of the column volume.

A second flow circuit was employed for the injection of samples and generation of chromatograms (seen in Figure 4.8). This was done since the Micropump pump in

the first circuit was designed to deliver large flow rates even high back-pressures, but was not able to deliver exact flow rates at low velocities. Instead, a pulse-free gear pump type Tuthill DGS.19PPPT2NNBG45 (Wagner Mess- und Regeltechnik GmbH, Offenbach, Germany) was employed. The Flow was controlled and measured by a Coriolis-type Bronkhorst High-Tech M13-RAD-22-K-S. The pressure was controlled by a digital pressure controller type Bronkhorst High-Tech P-502C-21KR-RAD-33-V (Wagner Mess- und Regeltechnik GmbH, Offenbach, Germany).

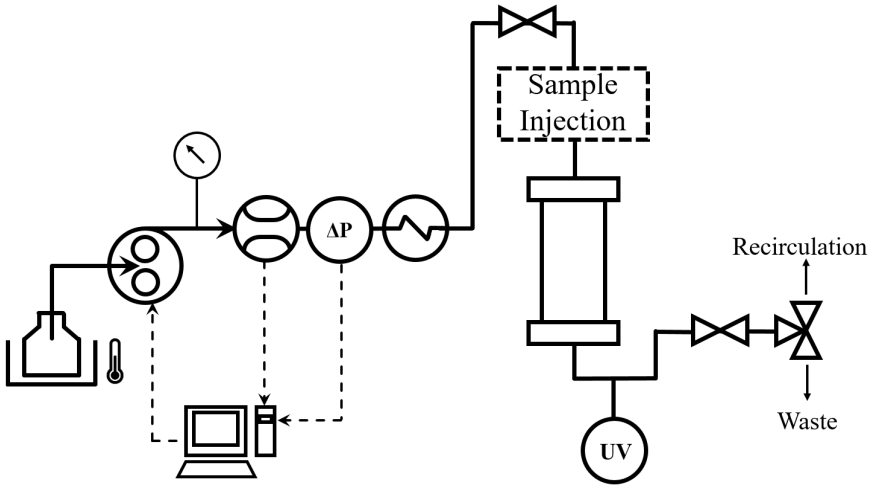

Fig. 4.8.: Hydraulic setup for the analysis of packed beds.

The elution of the substance was monitored with a UV-spectrophotometer (SPD-20A, Shimadzu Deutschland GmbH, Neufahrn bei Freising, Germany) fitted with a preparative flow cell (228-23406-91, Shimadzu) with a total volume of 6.5 µL. The photometer delivered analogue absorption data, which was gathered employing a 16-bit analogue-to-digital converter ADS1115 (Adafruit Industries, New York, USA) connected to a Raspberry Pi (Raspberry Pi Foundation, Cambridge, United Kingdom). Data logging was controlled employing a script written in Python 3.0.

The injection was done with two 4/2 valves with double bore type KH 144 H PP (Landefeld Druckluft und Hydraulik GmbH, Kassel, Germany) to achieve a constant injection volume, which could be changed by attaching larger or smaller tubing lengths (dashed line in Figure 4.9). Sample injection was done in three steps; loading, closing sample loop and injection. The starting state can be seen in Figure 4.9a, in which mobile phase fills the entire system and the valves are in a position to be loaded. Figure 4.9b shows the loading of the sample into the system, with excess solution flowing into waste. The loop is closed in Figure 4.9c and is ready for injection in Figure 4.9d. User-independent injection was guaranteed with the python script, which indicated the user

when to turn the right valve for injection.

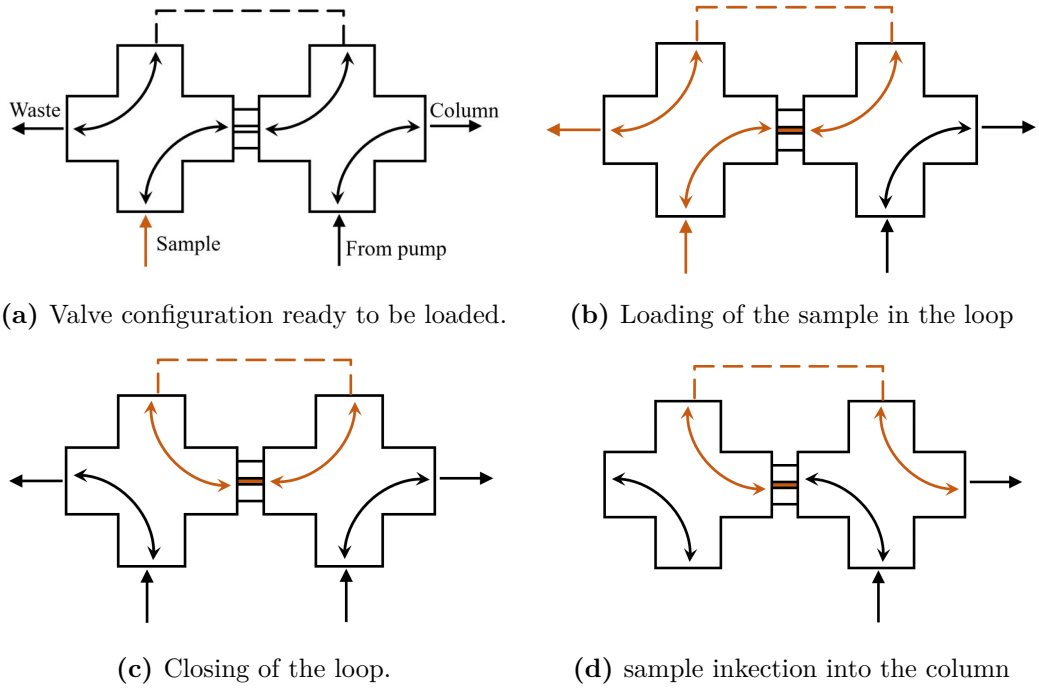

(a) Valve configuration ready to be loaded.

(b) Loading of the sample in the loop

(c) Closing of the loop.

(d) sample inkection into the column

Fig. 4.9.: Schematic of the injection system

This injection setup enables flow into the column at all times as the sample is loaded, avoiding variations which take place during other methods, such as manual injection of the sample into the column during flow interruption. All chromatograms were carried out at a velocity of 100 $^{cm}/_{h}$.

4.4.2. Process columns

Process columns were operated with a chromatographic skid type 02 from Bio-Rad Laboratories GmbH (Munich, Germany). It is a turnkey system including mechanical and control components (see Figure 4.10 for the PID of the skid). Flow is generated by two gear pumps (Figure 4.11a) which allow step or gradient mixing of two components in the mobile phase with a maximal flow of 600 $^{l}/_{h}$.

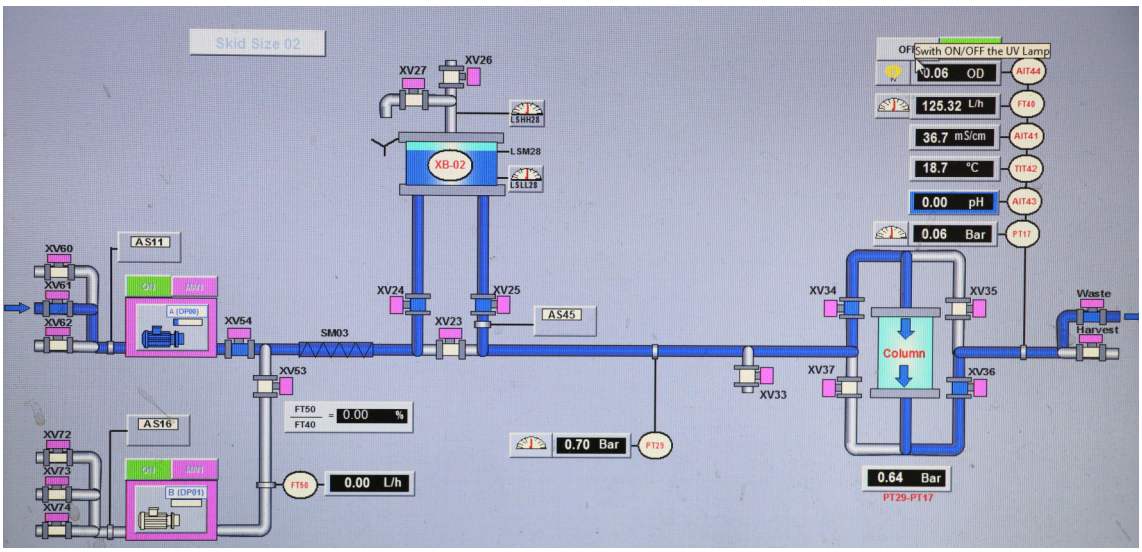

Fig. 4.10.: PID diagram and control software of the chromatography skid.

The employed configuration includes pressure sensors before and after the column, bubble sensors, bubble trap, UV and conductivity sensors, and ultrasonic flow meters. Process lines are made from stainless steel 316L and the layout is rated for up to 6 bar. Fluid path is set with pneumatic valves (denominated XV in Figure 4.10) operated with pressurized air at 6 bar.

Solutions were prepared in agitated stainless steel 200 l tanks, which were connected to the intake of the column. During packing and normal operation, the outgoing flow was fed into the tank to limit material use.

200 mm and 400 mm Bio-Rad columns were employed. The cylinder of both columns was made from PMMA with stainless steel bodies. Flow distributors were machined from stainless steel and had stainles steel meshes for particle retention. In both cases, plungers were moved with an electrical motor controlled with the provided software, and all seals and valves were operated with pressurized air. Both columns were fitted with slurry lines which were used for the initial insertion of the slurries.

For the initial particle insertion in both columns, a tank holding the particles was attached to the column through the slurry lines. The particle slurry was re-suspended in the tank and kept in suspension with manual low shear agitation. The plunger was lowered until about $\sim$ 5 cm above the bottom distributor and the column filled with mobile phase. Once full, the seal of the plunger was inflated and the slurry valves opened. The tank was connected to the column through a port located at the bottom with a valve. The plunger was driven upwards and the tank valve opened. The seal

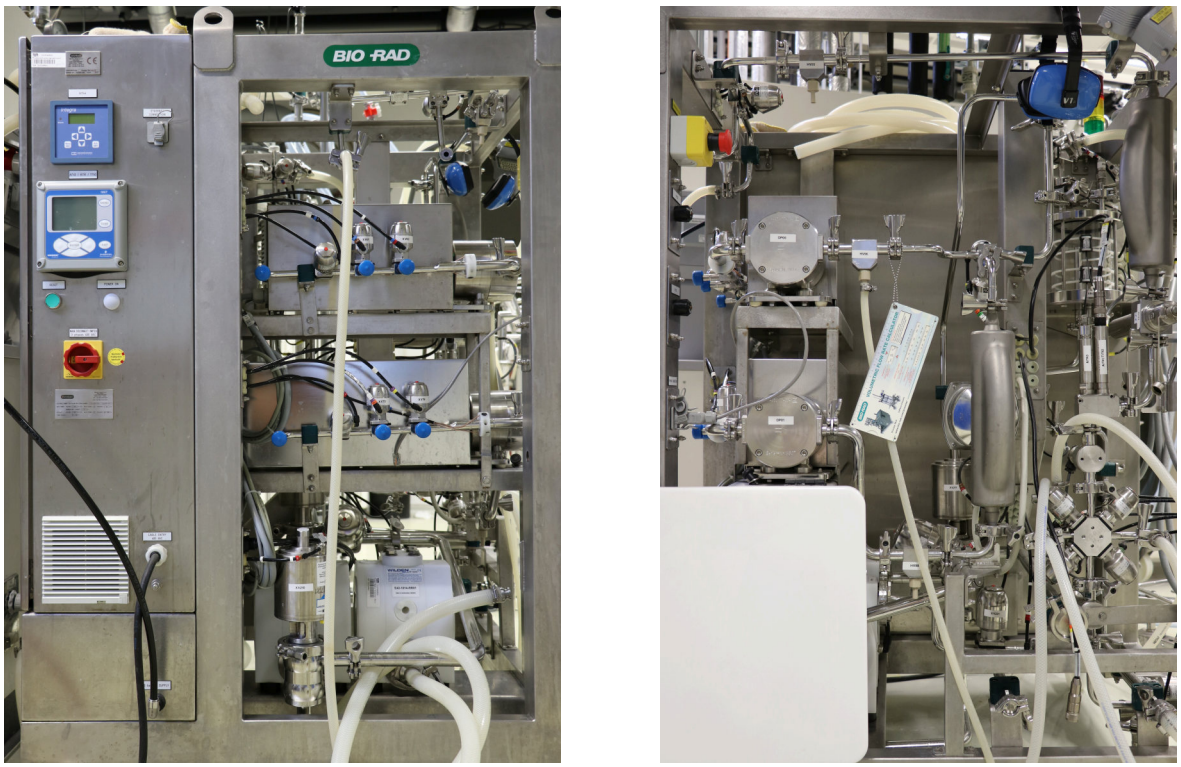

(a) Intakes and outtakes of the chromatographic skid covered by blue protective sleeves.

(b) Dual pump layout including double ultrasonic mass flow meter. Bubble trap can be seen in the top right.

Fig. 4.11.: Frontal and lateral view of Bio-Rad chromatography skid type 02.

of the plunger and its movement upwards act as syringe and draw the slurry into the tank.

Once the media was inserted, the attachment of the FP-35-S vibrators was done similarly for both columns by fastening one vibrator to each of the four legs (Figures 4.13 and 4.14). For the 200 mm column this could be achieved with the boring of a hole for a M12 bolt which was used to fasten the vibrators. A direct connection was not possible for the 400 mm column. Instead, an aluminum plate was used to act as a bridge connecting the vibrator to the column foot. Furthermore, the slurry lines had to be dismantled since they would otherwise collide with the vibrators.

In both columns, the presence of process lines and other elements on the underside of the column prevented the attachment of the vibrators directly to the flow distributor in an analogous manner to the FP-12-S vibrators on the 50 mm column.

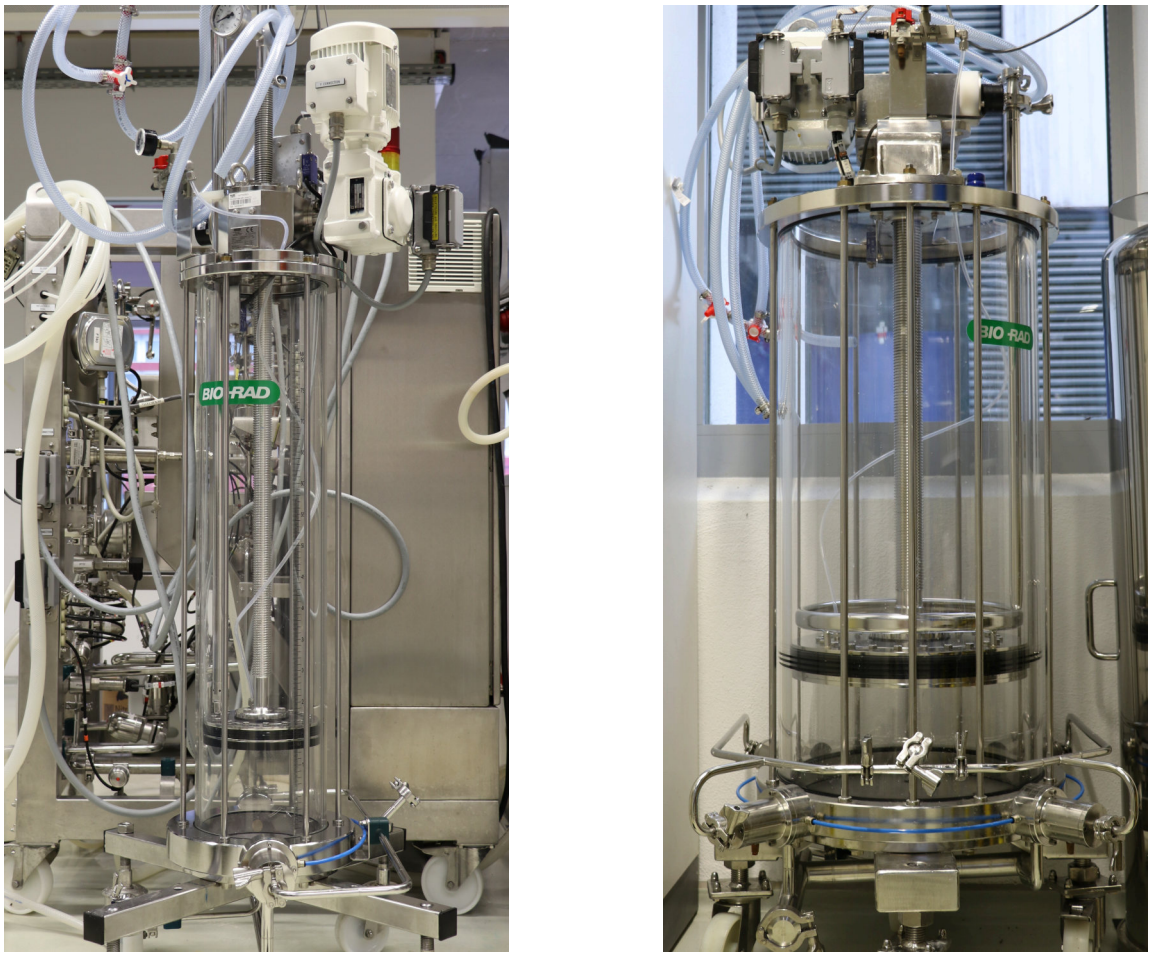

(a) Bio-Rad 200 mm column.

(b) Bio-Rad 400 mm column.

Fig. 4.12.: Bio-Rad 200 mm and 400 mm preparative column

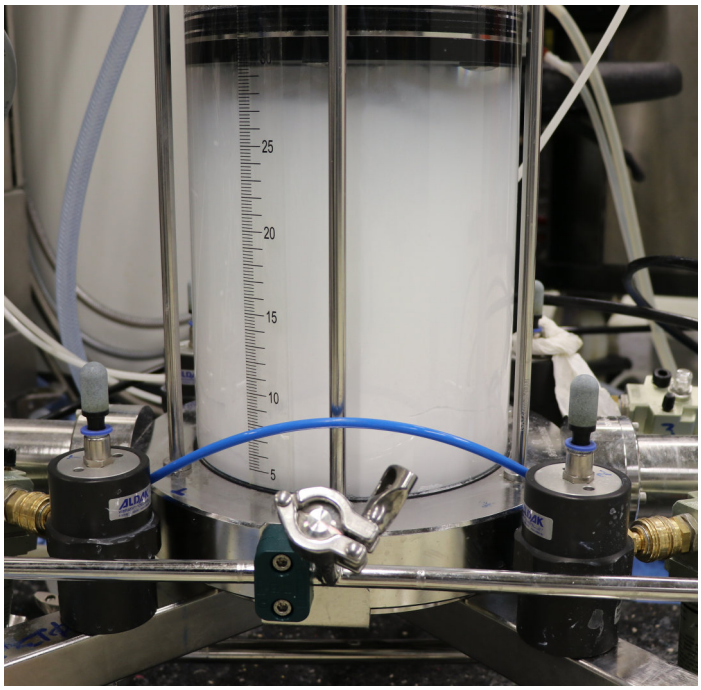

Fig. 4.13.: Two of the four FP-35-S vibrators visible on one side of the 200 mm column. The feet length in the 200 mm column allowed the vibrators to be directly attached with M12 bolts.

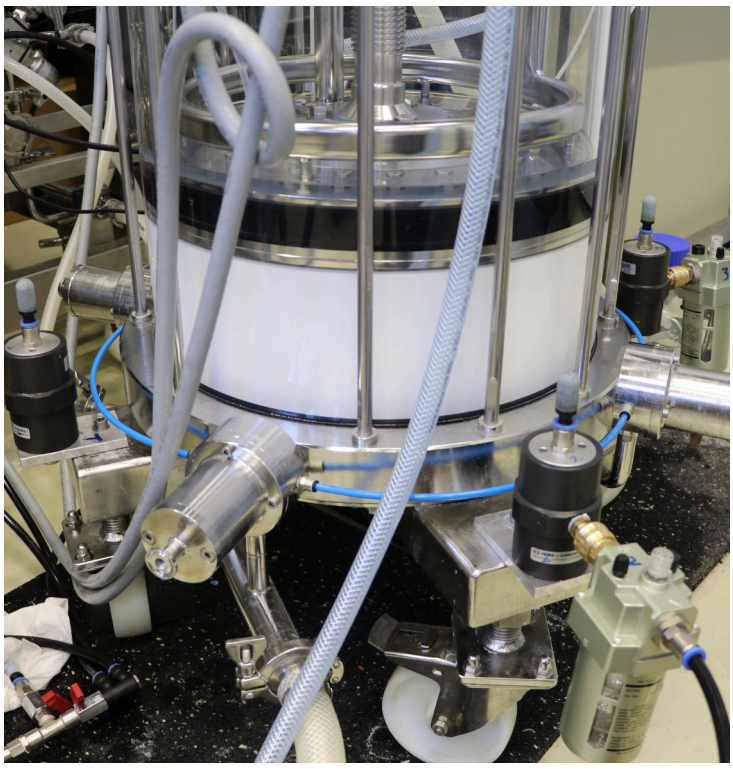

Fig. 4.14.: 400 mm column with three of the four fastened FP-35-S visible. A small aluminum plate was placed between legs and vibrator.

The unpacking of the 200 mm column could take place with the vibrators still attached. The 400 mm column required the removal of vibrators, and the reattachment of the slurry lines. Both columns were unpacked with a similar process, the particles inside the column were resuspended to form a $\sim$ 20% slurry by applying alternating upward and downward flow, after which intake and outtake column valves were closed. The air seal of the top distributor was opened and an air gap was created by elevating the plunger. The slurry lines were connected ahead of time to the tank which had previously contained the particles. The seal of the top distributor was filled and moved downwards, while the slurry vales were simultaneously opened. Plunger movement creates an inner pressure which pumps the slurry into the tank through the slurry valves.

Pulse experiments for process columns

Analogously as in the 50 mm column, pulse injection experiments were used for the calculation of the rHETP. For the process columns a solution adjusted to 1 M NaCl in the respective working buffer was employed. The injection volume was approximately 2 % of the respective column volume and the peak was monitored through the conductivity of the eluate. A setup similar as for the 50 mm column was employed for the injection of the sample. During pulse experiments the eluate was diverted into waste to prevent drift of the conductivity baseline of the solution in the 200 l tank.

Raw conductivity and time data were downloaded from the Bio-Rad PID control software as *.txt files and analyzed in MatLab 2017b.

4.5. X-ray computed tomography

X-ray tomographic measurements were carried out with a Micro Computed Tomography (Micro-CT) type XCT-1600HR (seen in Figure 4.16) from Matrix Technologies (Feldkirchen, Germany) at the institute of Process Systems Engineering of the Technical University of Munich. The X-ray source is located of the left of the picture, while the detector array is on the right. The sample cylinder can be seen between and is fixed to a holding chuck, which carries out the 360° rotation. Export of the tomography data as DICOM files was carried out using VGstudioMAX (Volume Graphics GmbH, Heidelberg, Germany).

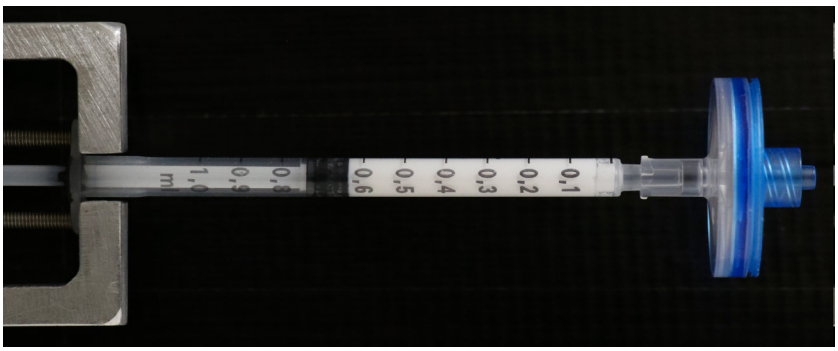

Fig. 4.15.: 1-ml Syringe containing CHT-Hydroxyapatite

4.5.1. Preliminary measurement

A preliminary measurement of CHT particles was made in a 1-ml syringe with an inner diameter of 3 mm. The syringe was kept in place with a custom aluminum holder (see Figure 4.15). The mobile phase was 10 mM NaOH in deionized water.

4.5.2. Main measurements

All other micro-CT measurements were made in two types of chromatographic columns. Columns with an inner diameter of 0.76 mm were used to develop the contrast-enhancing method, while 3 mm diameter columns were employed to compress the particle packings and reconstruct the microstructure using micro-CT after applying the contrast-enhancing method.

The employed tomographic parameters are listed in Table 4.3. Due to the larger volumn of the 3 mm columns, the working resolution was 4 µm, double that of the 760 µm columns.

Property	760 µm **column**	3 mm **column**
Voltage	60 kV	60 kV
Current	60 µA	60 µA
Exposure time	5945 ms	2007 ms
Number of projections	400	2000
Measured dimensions (X, Y, Z)	4 mm × 4 mm × 2.5 mm	8 mm × 8 mm × 4.8 mm
Pixel resolution	2 µm	4 µm

Table 4.3.: Employed micro-CT parameters for each column type.

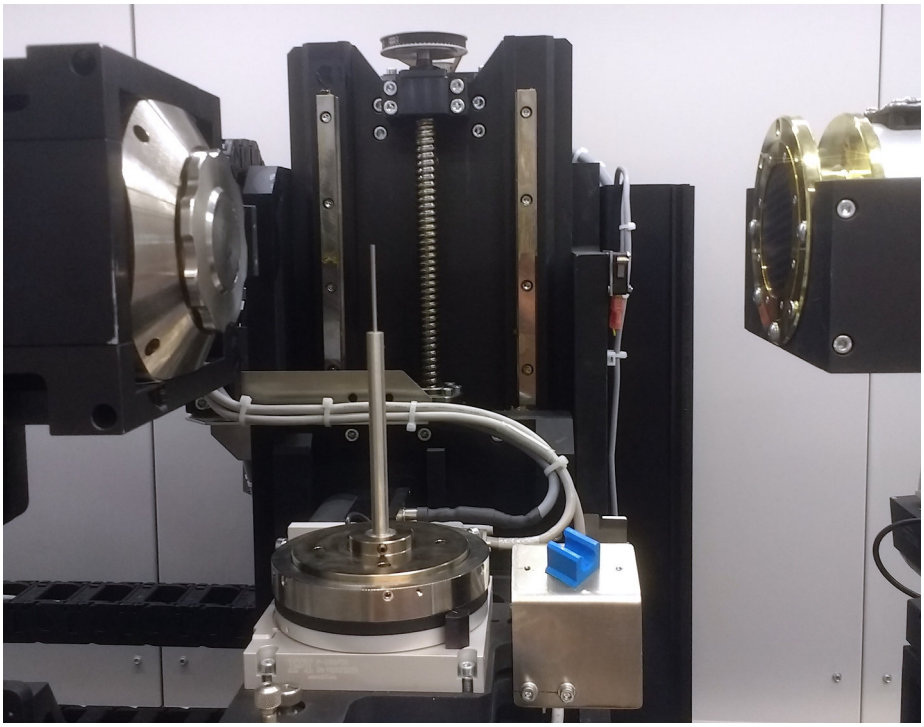

Fig. 4.16.: XCT-1600HR micro-computer tomography machine (Matrix Technologies, Feldkirchen, Germany).

N-decane, isopropanol, and sodium diatrizoate hydrate (SDH) were obtained from Sigma-Aldrich Chemie GmbH (Taufkirchen, Germany). Potassium iodide (KI) and silver nitrate were obtained from Carl Roth GmbH (Karlsruhe, Germany). Different pumping equipment was used for each column type.

4.5.3. Chromatographic columns for X-ray measurements

4.5.4. 0.76 mm capillaries

PEEK tubing with an internal diameter of 0.03 inches (0.76 mm) and an external diameter of 1/16 inch (1.59 mm) was purchased from Postnova Analytics GmbH (Landsberg, Germany). A 3D-printed adapter made of polylactic acid was employed during the screening studies to attach and actuate 10 mL or 20 mL B.Braun Omnifix polypropylene syringes (Carl Roth GmbH, Karlsruhe, Germany). For the final selective particle filling method, an ÄKTA purifier station (GE Healthcare GmbH, Munich, Germany) was used (both shown in Figure 4.17). The outlet of the columns was connected to a porous polypropylene frit with a thickness of 2 mm and a mean pore size of 25 µm (Bekolut GmbH, Hauptstuhl, Germany).

For insertion of particles into the capillary, the particles were suspended in the storage buffer to form a slurry concentration of $\sim$ 50 % and inserted into 8 cm long sections of PEEK micro columns using a 20 ml syringe. The particles were retained inside the micro column by the outlet frit. When using the ÄKTA, the filled columns were detached at this point from the syringe and connected to the ÄKTA station.

(a) 3D-printed syringe adapter for the manual packing and pumping of PEEK capillaries. A green capillary can be seen attached to the end of the syringe

(b) ÄKTA Purifier ©HPLC (GE-Healthcare) station employed for the packing and preparation of final samples of PEEK capillaries.

Fig. 4.17.: Employed equipment for the packing of 760 µm PEEK capillaries.

Once the pore-blocking method took place, the columns were removed from the mounts and cut into approximately 30 mm long pieces. Both ends were sealed with epoxy glue. For the measurement of the capillaries, a custom adapter 3D-printed with

poly-lactic acid was used to attach them to the sample holder of the micro-CT and prevent sample displacement. The measurements were carried out using the 2 µm sample holder supplied by the micro-CT manufacturer. With this configuration, the resolutions reached a voxel-to-diameter ratio of 20 and 32 for Capto Q ImpRes and Toyopearl SP-650M particles, respectively. The total measured volume corresponded to approximately 4 × 4 × 2.5 mm in the X, Y and Z dimension, respectively.

4.5.5. 3 mm column

Columns with the possibility of dynamic axial compression were designed and built (Figure 4.18). The columns have an internal and external diameter of 3 mm and 5 mm respectively, and are made of polymethylmethylacrylate(PMMA). In micro-CT, the achievable resolution is inversely proportional to the diameter of sample at its widest point. The column has a maximal diameter of ∼ 6 mm (black regions in Figure 4.18b), which enabled micro-CT measurements at a resolution of 4µm per pixel.

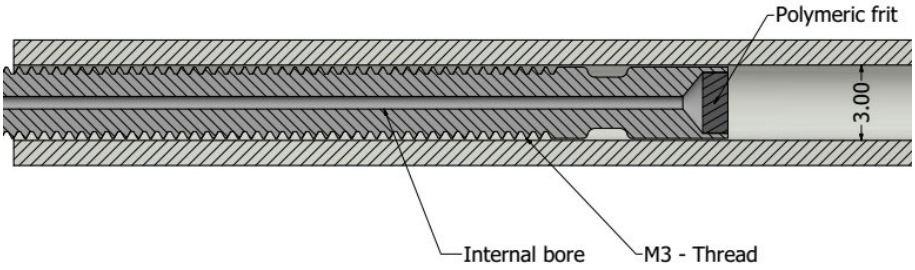

(a) Internal view of the column plunger.

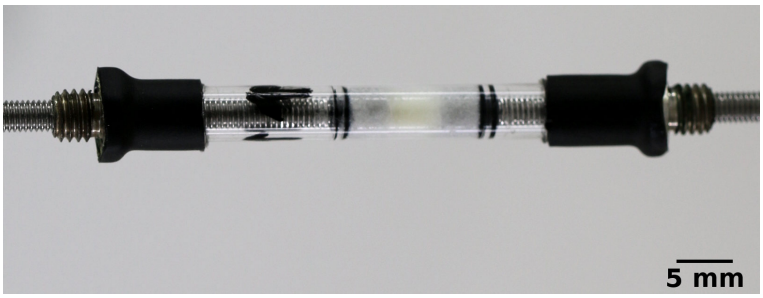

(b) Micro-column built for micro-CT measurements.

Fig. 4.18.: Design and construction of 3 mm column

The flow distributors are made from stainless steel tubes (EHM Edelstahl GmbH, Duisburg, Germany) with an outer diameter of 3 mm with an internal bore of 0.25 mm for the passage of the fluid phase. The tubes were machined for the inclusion of a

porous polypropylene frit with a thickness of 2 mm and a mean pore size of 25 µm. Additionally, each distributor was sealed with two NBR O-rings (1 mm x 1 mm) and a standard M3 thread was cut on the outer wall of the tubes.

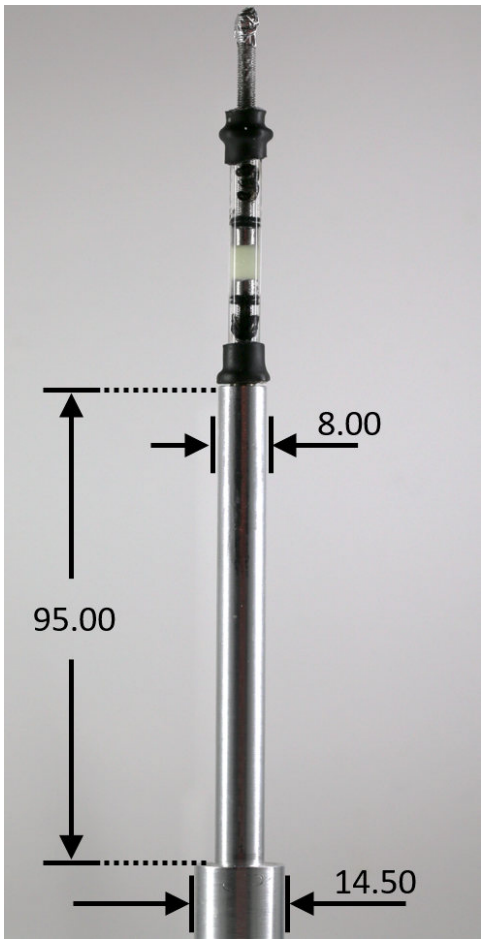

Fig. 4.19.: Custom-holder. Dimensions in millimeters.

An internal M3 to external M5 thread adapter is positioned on each of the column and held in place with a glued shrink-tube (10 mm x 10 mm, Sintron Connect). The flow distributors can be rotated to set the column height. A push fitting with an internal M3 thread port (Landefeld gmbH, Kassel, Germany) is connected to each distributor and to the pumping equipment.
Sample holding is a critical step during micro-CT measurement, since minute movements at the micrometer scale prevent a successful reconstruction. Moreover, measurement time is a function of the number of projections and exposure time, with measurements of the 3 mm column regularly taking over one hour.

The external M5 thread enables the attachment of the column to a custom built sample holder (shown in Figure 4.19) with an internal M5 thread machined from aluminum. The column can then be measured in its compressed state in the micro-CT.

4.5.6. Image processing and analysis

DICOM files were loaded in FIJI, processed and binarized [82]. Algorithms and parameters selected during image processing steps were chosen by visual inspection. The exact image processing operations were used for all packing materials, although adaptation of brightness/contrast and other filter parameters were required in each case.

The data-sets were cropped to the area of interest before carrying out brightness and contrast adaptation. Speckle and noise removing filters based on the median and Kuwahara operators were employed, after which binarization was applied using Otsu's [83] thresholding method with an automatic local thresholding approach. After this, a watershed algorithm was implemented to separate merged particles, after which erosion and subsequent dilation operations were used to remove leftover noise and imaging artifacts.

As final step, a dilation operation followed by a final watershed were implemented. A complete measurement data-set was composed of 1240 DICOM slices, on which the operations were applied. The resulting stack was saved as a TIFF file sequence. 3-dimensional renderings of the packing structures were generated by loading the TIFF stacks into Paraview 5.2.0 (Kitware Inc. und Los Alamos National Laboratory, USA).

MatLab 2017b (MathWorks, Natick, Massachusetts, USA) was used for the digital processing and data analysis based on the TIFF stack images. The initial step of the analysis was to correct any inclination of the column by finding the center of the column and aligning all tomographic slices. This was done by finding the extreme-most points in each slice and deriving the center of the column by fitting the inner capillary wall.

The local external porosity was calculated by dividing each tomographic slice in concentric rings, each having a fixed width, and whose centers were aligned with the column center point. This point had been found for each slice during the first centering step. Starting from the center of the packing, the analyzed ring region was iteratively expanded until it reached the column wall. The total amount of pixels located inside each ring and the number of pixels corresponding to particles were saved. This process was repeated for all TIFF slices, after which the data for identical radial positions were summed up and the external porosity was derived using the equation

$$\varepsilon = \frac{Pix_{Total} - Pix_{Particle}}{Pix_{Total}} \tag{4.1}$$

4.5.7. Syringe pump

A custom syringe pump was employed to pack and carry out the pore-blocking method in the 3 mm columns. It consisted of several aluminum 40x40 aluminum extrusions (Alvaris Profile systems GmbH, Suhl, Germany) forming the support structure for the mechanics and electronics (see Figure 4.20). 3D-printed parts were attached to the frame and used to hold the motor, syringe and other mechanical elements. A standard NEMA17 motor rotated an M6 threaded rod, which went through a nut embedded in

3D-printed piece translating rotation into linear movement. A steel cylinder was used as guiding rail to prevent torsion of the system.

The motor was driven with an Arduino Uno, a Big Easy Driver (Schmalz Haus LLC) and an LCD shield. Flow rate and injected volume were a function of syringe size, motor velocity and total rotation. The smallest reliable volume that could be pumped was 40 µL and the pump could deliver flow at pressures up to 3 bar.

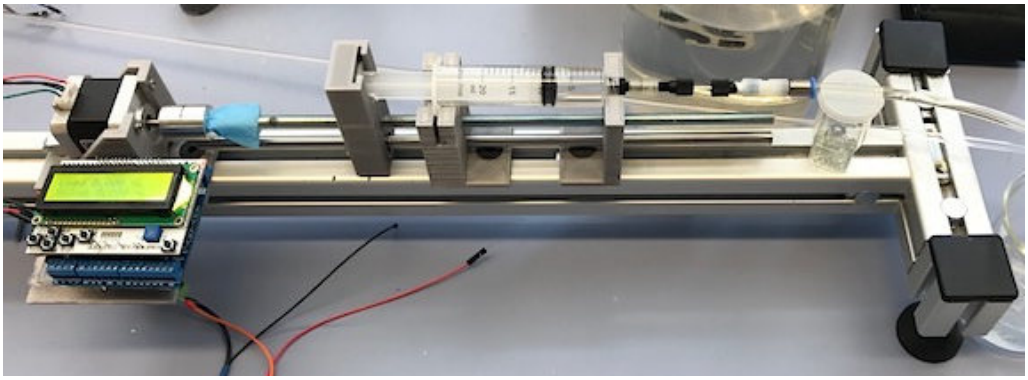

Fig. 4.20.: Developed automatic syringe pump for the packing and preparation of 3 mm columns.

4.6. Software

The code used in this work is contained in the accompanying DVD or in the appendices.

4.6.1. Image Processing

Analysis of particle size distributions and basic image processing (brightness, contrast, cropping) were carried out in FIJI [82], an image processing distribution based on ImageJ.

4.6.2. HETP calculation and column analysis

Data from pulse experiments for all three columns was analyzed with custom scripts written in MatLab 2017b (Mathworks, Natick, Massachusetts, USA)

4.6.3. Ultrasound simulation

The K-wave Toolbox [84] for Matlab was employed for the simulation of ultrasound propagation and acoustic fields. Pressure and velocity fields were used for the calcula-

tion of the Gorkov potential employing Matlab 2017b. The forces obtained through the gradient of the Gorkov potential could be passed on to LIGGGHTS-PUBLIC (LAMMPS Improved for General Granular and Granular Heat Transfer Simulations) Version 3.6.0 (DCS Computing GmbH, Linz, Österreich) [85] to carry out a granular simulation. The assignment of the forces acting on each particle was kept updated by employing a coupling script written in Python Version 2.7. (Python Software Foundation, Wilmington, Delaware, USA). ParaView Version 5.2.0 was employed for the visualization of granular simulations.

5. Tomographic X-ray measurement of chromatographic columns [1]

This chapter describes the development of a particle X-ray contrast enhancing method for column measurement and reconstruction employing micro-computed tomography (micro-CT). An algorithm was developed to binarize this data and obtain the final 3-dimensional reconstructions. Based on this information, different geometrical properties were calculated; axial and radial porosity, and the presence of void spaces in the packing.

Following the establishment of the method, a novel column was developed to study the compression behavior of chromatographic packings under mechanical stress. This column enables to carry out the contrast-enhancing method on already packed beds, and is specifically designed to be fixed in the probe holder of the employed micro-CT machine.

Additionally, a particle tagging method was developed by precipitating a silver salt inside the particles.

5.1. Enhancement of X-ray contrast of chromatographic columns

5.1.1. Preliminary measurements

The goal of micro-CT measurements of chromatographic columns is to study the influence of packing parameters and steps on the final bed structure. The first approach was the measurement of a ceramic hydroxyapatite (CHT) column with an inner diameter of 3 mm. It was assumed that due to the presence of calcium (atomic number = 20)

[1] This chapter contains information published in: A. Martinez, M. Kuhn, H. Briesen, D. Hekmat (2019). Enhancing the X-ray contrast of polymeric biochromatography particles for three-dimensional imaging. J. of Chromatography A 1590 (2019) 65-72. DOI:10.1016/j.chroma.2018.12.065

and phosphorus atoms (atomic number = 15) in the matrix, the particles would absorb enough X-ray to be differentiated from the mobile phase containing mostly water.

The effect of the high particle porosity on micro-CT measurements of ceramic hydroxyapatite media can be seen in Figure 5.1. The ceramic material contains and thus has a higher x-ray absorption than deionized water (atomic number = 1 and atomic number = 8 for hydrogen and oxygen respectively). However, due to the internal porosity of the media, the volume occupied by the particles is mostly composed by the mobile phase. There is thus not enough void spaces and individual particles. No structures can be discerned either in radial or axial direction.

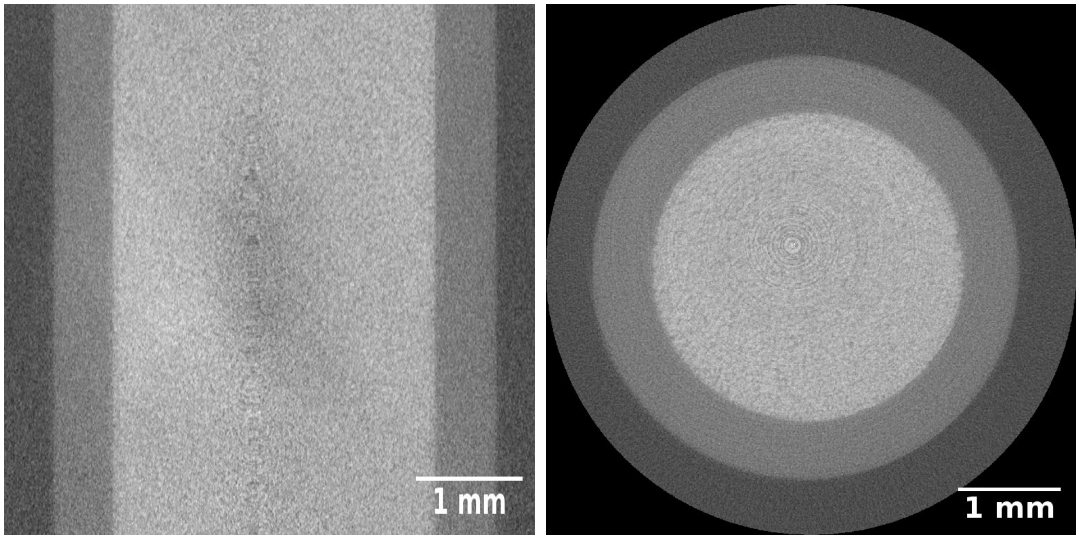

(a) Vertical cut of the sample **(b)** Horizontal slice

Fig. 5.1.: Micro-CT measurement of a ceramic hydroxyapatite packing. The contrast factor of CHT chromatography media is not high enough to determine the geometric structure of the bed.

It was thus identified that before packing parameters could be studied, it would be necessary to develop a method to make chromatographic particle discernible from the void spaces. It was also identified that the main obstacle was the high internal porosity of the media, which rendered even materials composed by heavy atoms too similar to the mobile phase.

5.1.2. Selective particle filling

In this section polymethylacrylate (PMA) particles with a median size of 65 µm, and agarose media with a median size of 40 µm were employed. The main obstacle for the X-ray imaging is the diffusion of the interparticle phase into the intraparticle volume.

It was necessary to establish a method for the selective filling of the particles with a phase which was non-miscible with the fluid surrounding them. By dissolving a contrast media into one of the phases, it is possible to choose which domain will absorb X-ray radiation, the particles or the void spaces.

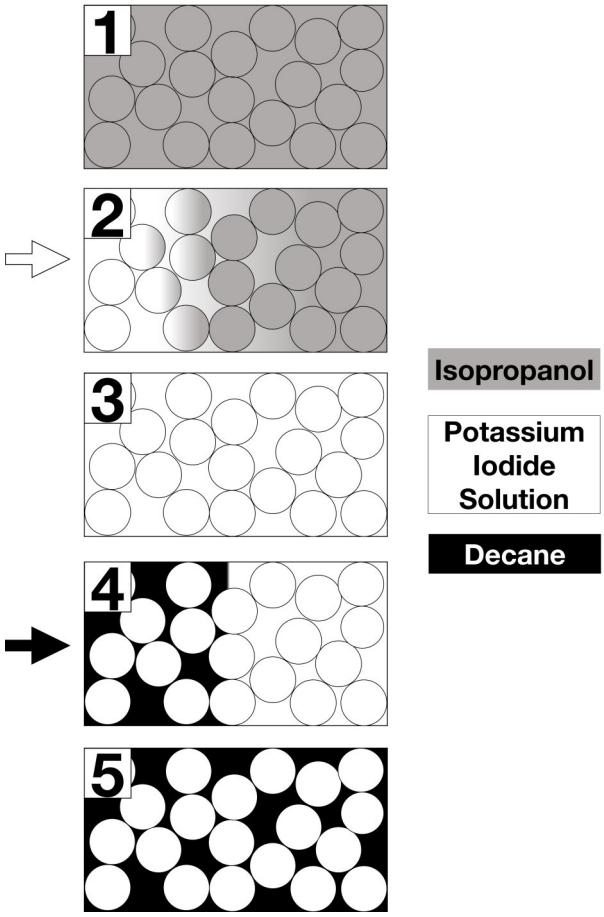

Fig. 5.2.: Schematic representation of the modified pore blocking method (PBM) originally developed by Cabooter et al. (2007) [86]. 1) The packed column is filled with isopropanol. 2) An aqueous solution of potassium iodide is pumped into the column. 3) Due to their miscibility, isopropanol mixes with and is eventually displaced by the aqueous solution of potassium iodide which then fills all spaces. 4) N-decane is pumped into the column, displacing the immiscible aqueous solution from the extraparticle void space. 5) Particles remain filled with the aqueous potassium iodide solution while the extraparticle space contains n-decane.

Figure 5.2 shows an overview of the developed selective filling process, based on [86]. The basic principle relies on the non-miscibility of hydrophobic and hydrophilic phases. This is achieved by pumping each phase in a specific succession through an already packed bed.

The first step was to find adequate flow rates and times for each phase, as well as an

adequate X-Ray contrast additive.

Screening study

Polymethylacrylate particles were chosen for the initial study of the method. The particle slurry was manually packed into PEEK capillaries employing a 3D-printed adapter (seen in Figure 4.17a). Micro-CT measurements of the manually prepared samples with the two contrast media sodium diatrizoate hydrate (SDH) and potassium iodide (KI) were carried out at concentrations of up to 0.3 and 1.2 g/mL, respectively. The best improvement of particle X-ray contrast was observed at the higher concentrations. When employing SDH as the contrast media, the hydrophilic phase formed liquid bridges between the filled particles (Figure 5.3).

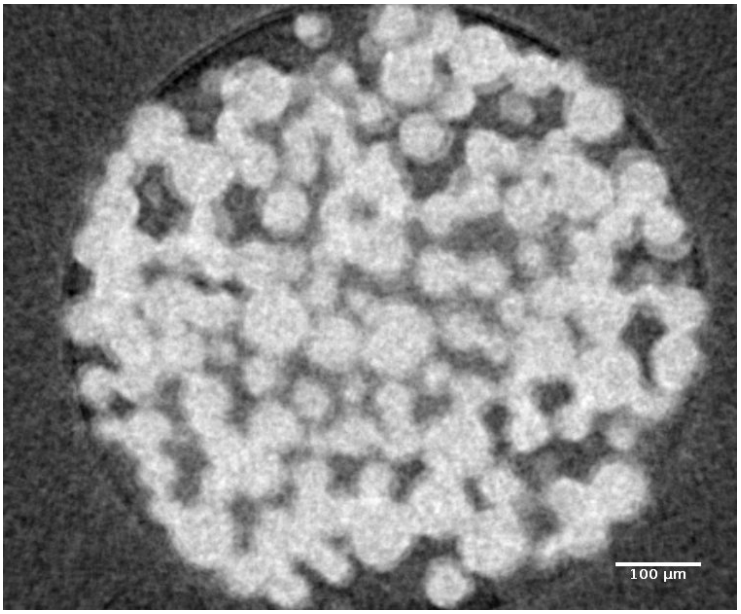

Fig. 5.3.: Tomographic segment of a PMA packing after SDH hydrophilic pore blocking. Interparticle spaces contain decane. SDH builds bridges between the particles which obstruct the segmentation and reconstruction of the particles.

When using aqueous potassium iodide as the contrast solution, no liquid bridging between particles could be observed (see Figure 5.6a). The comparatively better particle filling observed when using KI solutions could have been caused by the increase in surface tension of the solution induced by the dissolved inorganic salt. In comparison, SDH solutions had a decreased surface tension, this property being a common characteristic of water-soluble radiocontrast agents used in medical CT ([87], pp. 513-520). KI solutions of 1.2 g/mL were thus employed as the hydrophilic phase in the further

experiments. Once the pore-blocking process was terminated, the frit on the column outlet was removed and the column packing was carefully pushed out using the corresponding void-filling phase. The suspended blocked particles were analyzed by light microscopy.

It was observed that the pore-blocking of the particles could be visually inspected under the microscope due to the change in refractive index caused by their filling solution. This can be seen in Figure 5.4. The success of the particle filling as a function of the employed flow rates could thus be quickly verified without requiring equipment- and time-intensive micro-CT measurements. It was observed that inadequate handling, for example by bending the column, or too high intermediate flow rates caused a "squeezing-out" effect of the solution inside the particles. This resulted in partially filled particles, regions of the column containing no filled particles, or regions in which the aqueous phase coalesced and occupied both particles and void spaces. Additionally, the swelling or shrinking behavior of PMA and agarose particles in the employed solvents was studied. No visible change in the size of both particle types was observed in the aqueous phases, in pure isopropanol, and in pure n-decane.

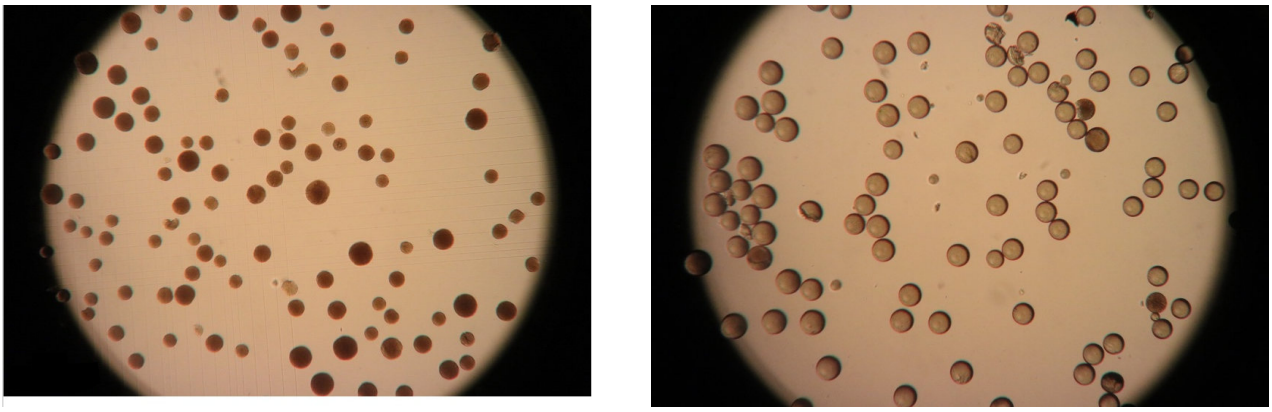

(a) PMA packing before hydrophobic filling. Particles are filled with the surrounding solution, aqueous 10 mM NaOH.

(b) PMA particles after undergoing hydrophobic pore blocking. Particles contain n-decane and are surrounded by aqueous 10 mM NaOH.

Fig. 5.4.: Visual inspection of the pore-blocking method on PMA particles.

Additionally, it could be established that particles could be filled with either the hydrophobic or hydrophilic phase. Since the contrast agent was soluble only in the hydrophilic phase, this meant that either the X-Ray absorption of the particles or the void-spaces could be selective increased. The steps for the hydrophobic pore-blocking can be seen in Figure 5.5

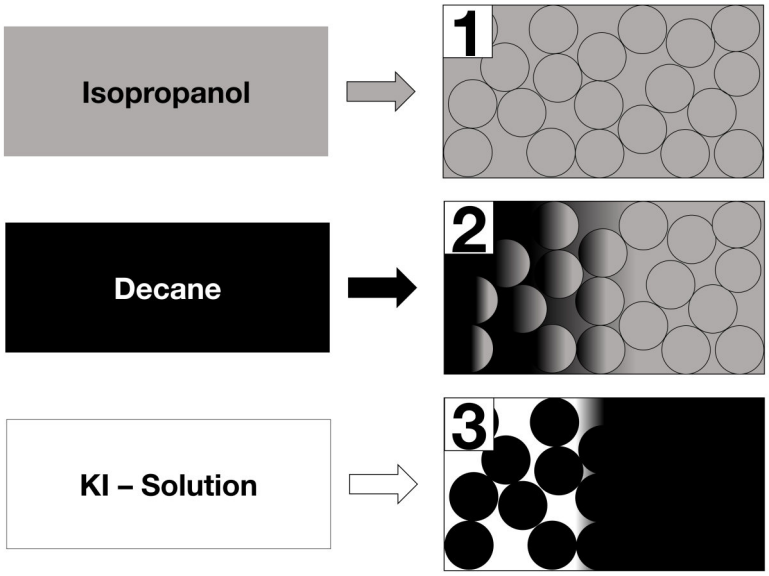

Fig. 5.5.: Hydrophobic pore-blocking method. The particles are filled with decane while the inter-particle space contains a potassium iodide solution.

Figures 5.6a and 5.6b show an hydrophilic and hydrophobic blocked packing respectively. The shadowing seen in the right pictures is caused by movement of the column during CT measurement.

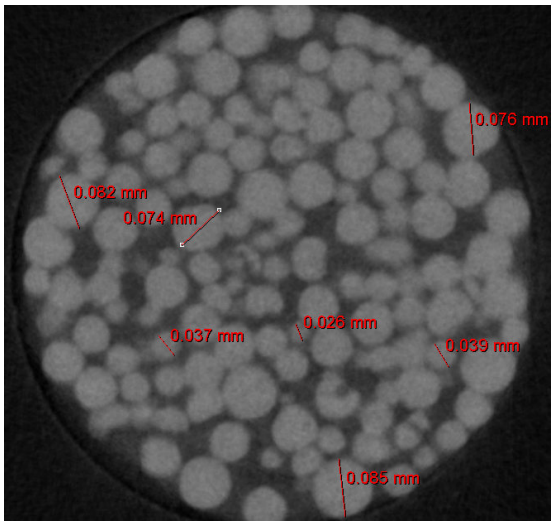

(a) PMA packing after hydrophilic pore-blocking.

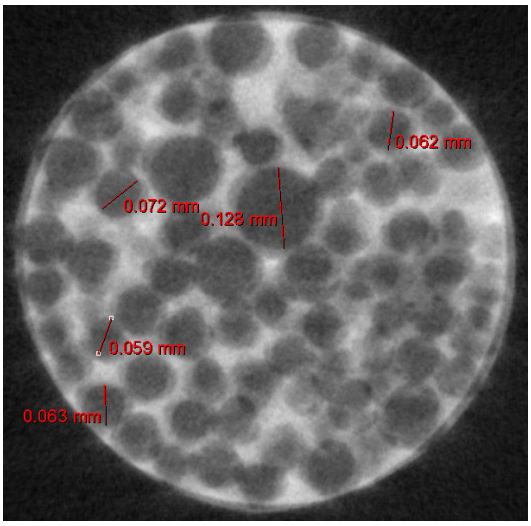

(b) PMA packing after hydrophobic pore-blocking.

Fig. 5.6.: The pore blocking method enables the selective enhancement of X-Ray absorption of either particles or voids.

Finally, the possibility of removing the pore blocking agents from the micro columns

was studied. A micro column packed with PMA particles was subjected to hydrophilic pore blocking as previously described. After this, the column was flushed with isopropanol at 0.3 $^{ml}/_{min}$ for 12 min, after which an aqueous 10 mM NaOH solution was pumped at 0.3 $^{ml}/_{min}$ for 12 min. The micro column was then sealed. No residual radiocontrast agents were appreciable in a subsequent micro-CT measurement (Figure 5.7). Thus, a differentiation of particles and surrounding fluid was no longer possible. This indicated that the micro column was successfully returned to its original state (except non-detectable residual traces of pore blocking agents).

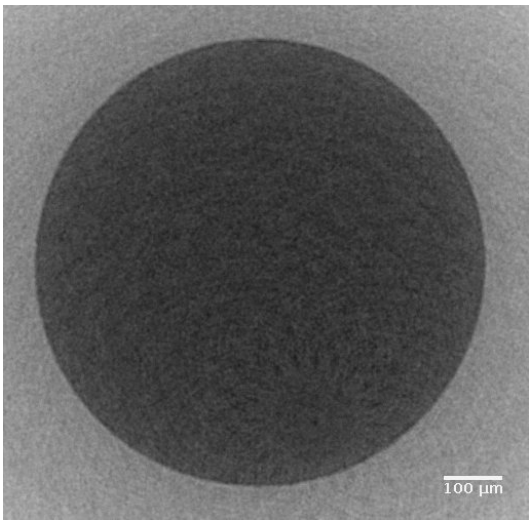

Fig. 5.7.: Tomographic segment of a PMA packing after SDH hydrophilic pore blocking and subsequent washing. The packing was washed with isopropanol and deionized water after pore blocking. No contrast media remains in the particles, and these are thus unidentifiable.

Agarose and polymethylacrylate packing micro-CT measurements

The developed method consisted of the use of a HPLC pumping system for the packing and selective filling. Isopropanol was used as packing solution. PMA particles were packed at a flow of 1 $^{ml}/_{min}$ for 15 minutes, while agarose particles were packed at 0.5 $^{ml}/_{min}$ due to their smaller size, which could cause a higher pressure drop and damage them due to their higher compressibility. For each media KI solution was pumped at 0.4 $^{ml}/_{min}$ for 10 minutes, after which n-decane was pumped at 0.1 $^{ml}/_{min}$ for 20 minutes. To avoid disrupting the initial structure achieved during packing, all flow rates during application of the pore-blocking method were well below the packing flow rate. Additionally, flow rates were slowly increased and lowered during all steps to prevent particle damage, abrupt packing compression or decompression, and

subsequent "squeezing-out" of the liquid phase from the pores of the particles due to their viscoelastic property. Columns were prepared as described in Section 4.5.4 and measured in the micro-CT. Tomographic results for agarose and PMA packings can be seen in Figure 5.8.

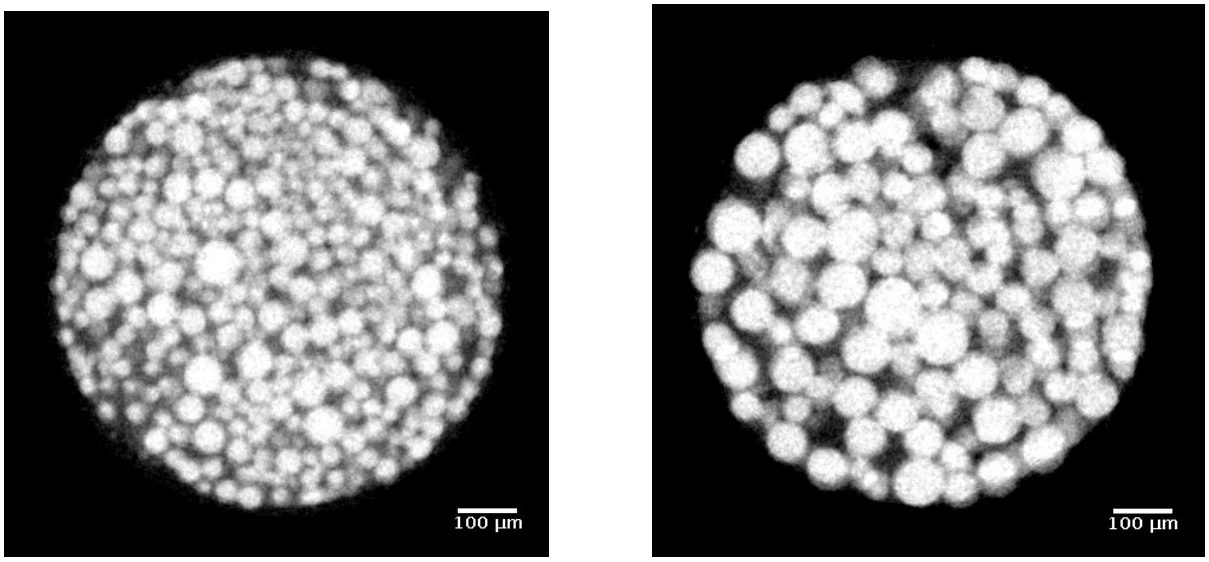

(a) PMA packing. **(b)** Agarose packing.

Fig. 5.8.: Tomographic segments of two chromatographic packings modified with the developed contrast-enhancing method. The particles contain dissolved potassium iodide, while the interparticle spaces contain n-decane.

5.2. Binarization and 3D-reconstruction algorithm

The succession of tomograph processing steps for a PMA packing can be seen in Figure 5.9. The initial step consisted of cropping, applying filters to reduce noise and balancing of the picture histogram. Particles were differentiated from void spaces using a watershed algorithm, and particle centers found by applying erosion functions, which were complemented with dilation steps. The same series of steps were carried out for agarose packings, albeit with different function parameters due to the different particle size. The stack of binarised images was used to generate 3-dimensional reconstructions of the measured packings. Figure 5.10 shows the reconstructed beds for both materials.

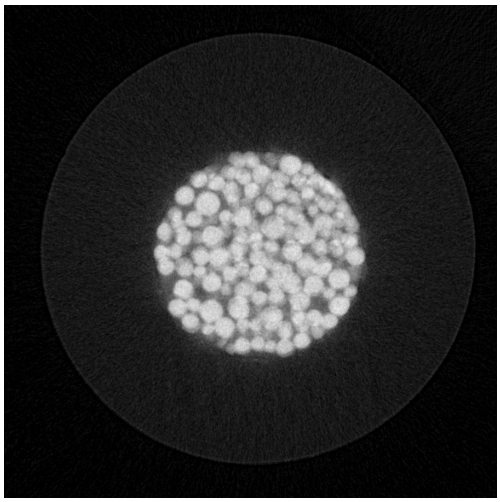

(a) Raw tomographic slice of a PMA packing.

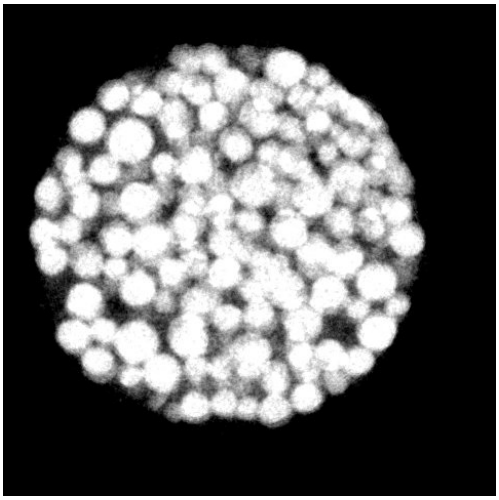

(b) After balancing contrast and brightness.

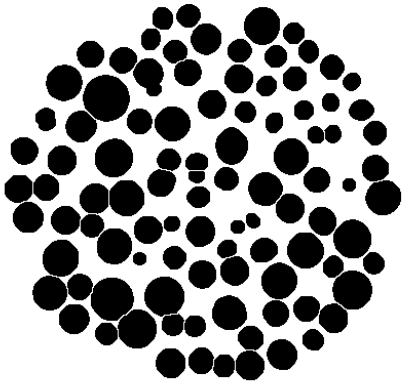

(c) After finding particle centers and dilation.

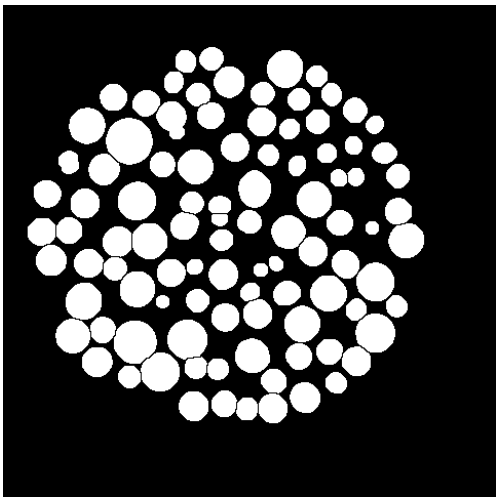

(d) Final binarised image.

Fig. 5.9.: Overview of the main binarization steps. Measurement of a PMA packing after hydrophilic pore-blocking.

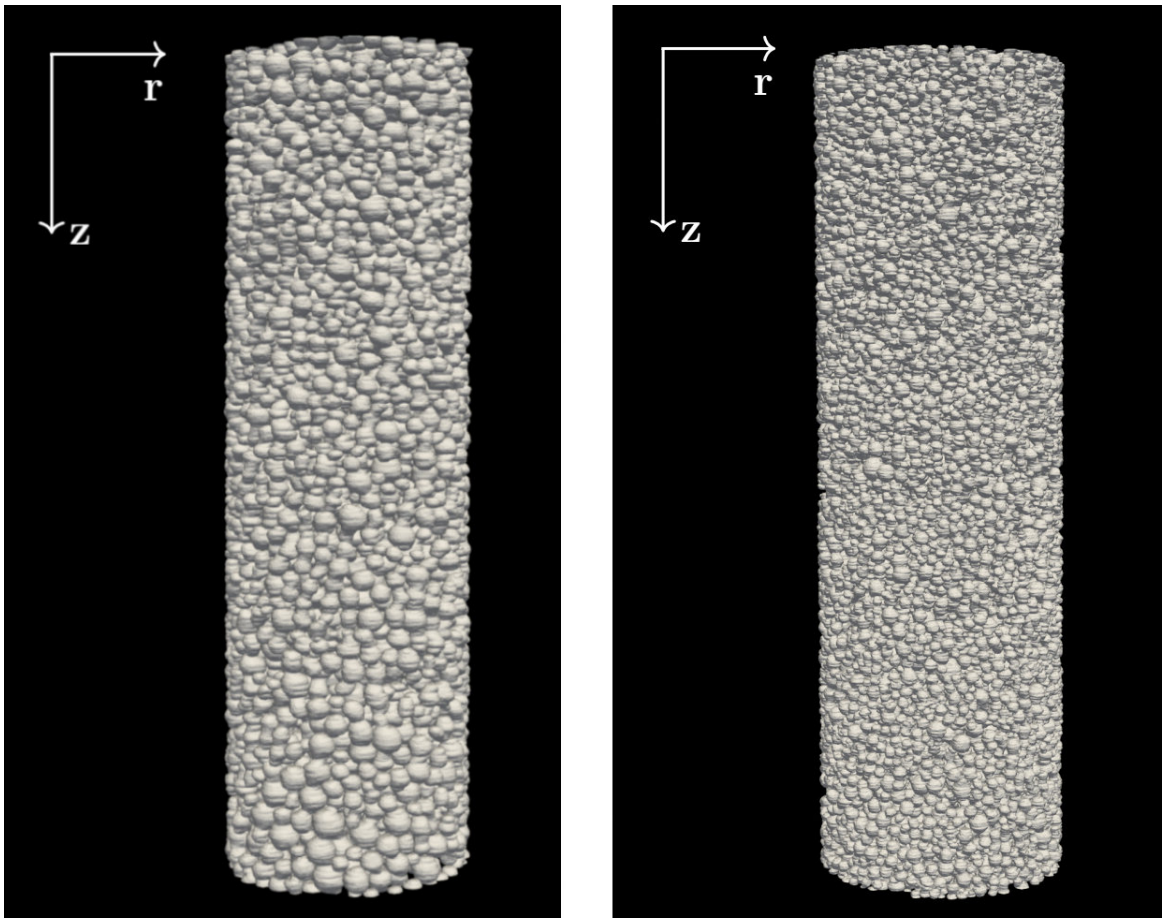

Fig. 5.10.: 3-dimensional reconstruction of (left) PMA and (right) Agarose packings. Height and diameter are respectively 2.5 mm and 760 µm for both packings.

The size difference between both media can be well appreciated. Moreover, it is possible to analyze the packings and obtain structural properties from the 3-dimensional reconstruction.

5.3. Packing analysis

5.3.1. Polymethylacrylate packing

The porosity profile of the packing in the axial direction can be seen in Figure 5.11. The top of the packing corresponds to X = 0 µm. Overall, porosity is mostly constant along the packing length. This was due to the fact that, although the bed was tightly packed, it was not in a compressed state. The variations and spikes of the profile can be explained by the relatively large size of the particles in comparison to the column. Since the $^{d_p}/_{D_{Col}} \sim 12$, stochastic variations of individual particle positions have a large impact on the porosity. This is particularly evident in comparison with the axial porosity profile of the agarose packing, which has smaller spikes due to a smaller particle size distribution (seen in Figure 5.14).

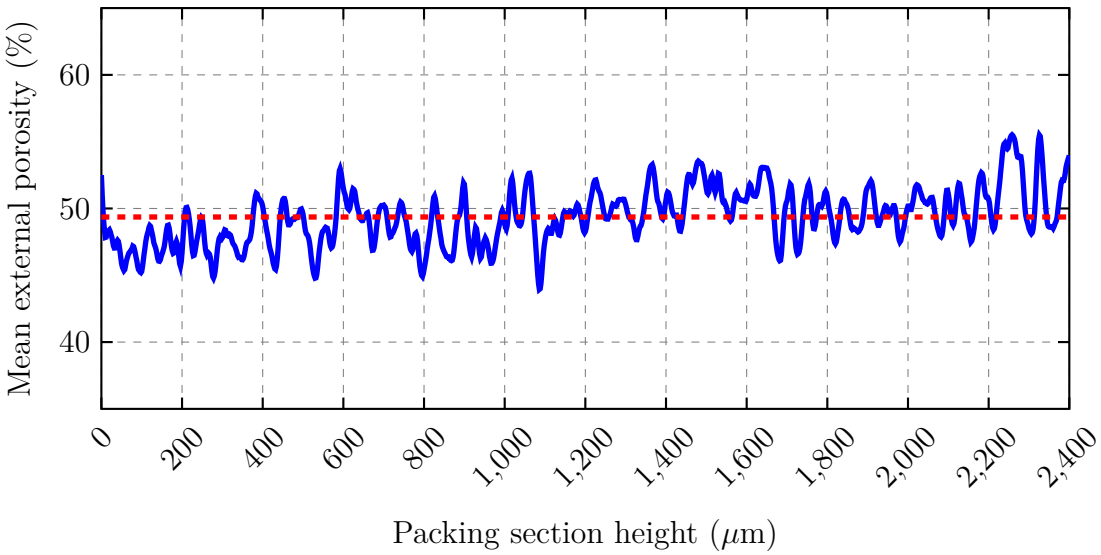

Fig. 5.11.: Porosity profile of the PMA packing along its length. Dashed line indicates overall packing porosity of 49.5 %.

The radial porosity profiles of the reconstructed PMA packing can be seen in Figure 5.12. The profile had its minimum at $r \sim 35$ µm which approached the median radius of the particles. The oscillating profile near the column wall shows the first highly

ordered layer. The overall mean porosity value of the complete analyzed reconstruction of 49.5 % is indicated by the dotted red line.

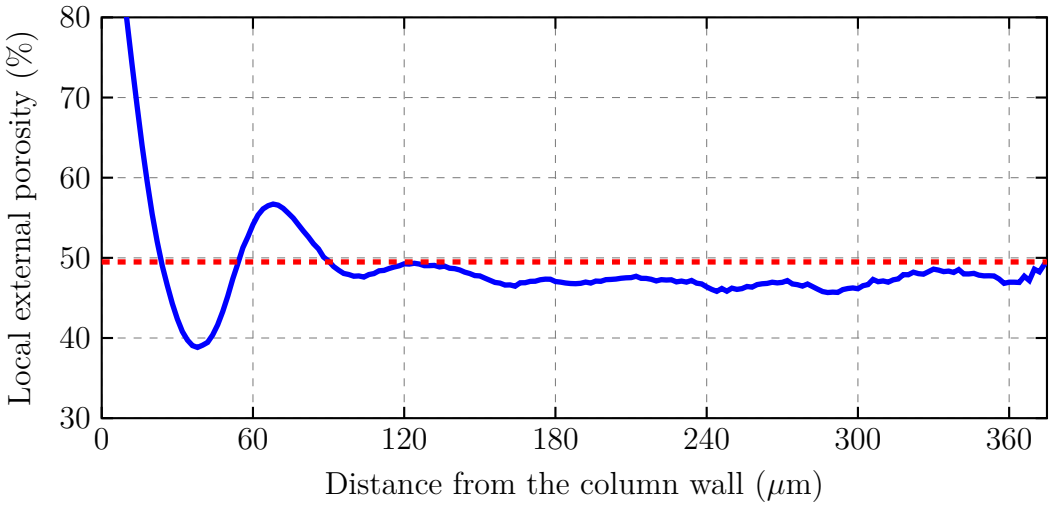

Fig. 5.12.: Radial porosity profile of the PMA packing. Blue line represents the smoothed profile ($r = 0$ corresponds to the column wall), while the dashed line indicates the overall packing porosity of 49.5 %.

The presence of voids in the top 200 µm was exemplarily determined. Void regions with a distance equal to or lager than the mean particle radius (~ 30 µm) are highlighted in red in Figure 5.13.

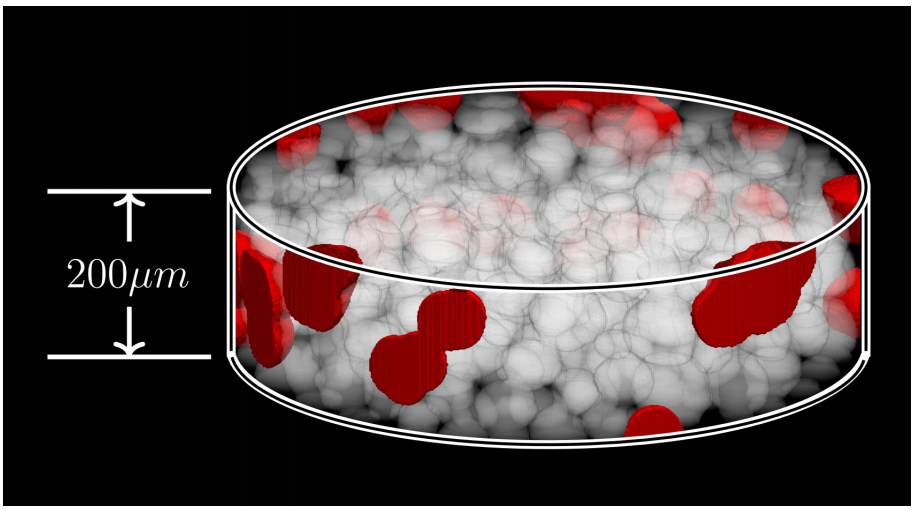

Fig. 5.13.: 3D reconstruction of the top 200 µm section of the PMA packing shown in translucent gray. Void spaces with a 3D distance equal to or lager than the mean particle radius to the nearest particle are shown in red.

It can be seen that largest voids are predominantly located on the column wall. This

agrees with previous research which indicates that the wall region has a lower efficiency, partially due a high mobile phase velocity gradient caused by the voids.

5.3.2. Agarose packing

Figure 5.14 shows the porosity profile along the packing length. As with the PMA packing, porosity remains constant through the bed due to its relaxed state. The smaller particle size implies that more particles can occupy the cross section of the column, and that each particle occupies less of the axial length. Thus, the random location of individual particles has less of an impact in the variation of the porosity. This can be seen as the profile being more uniform.

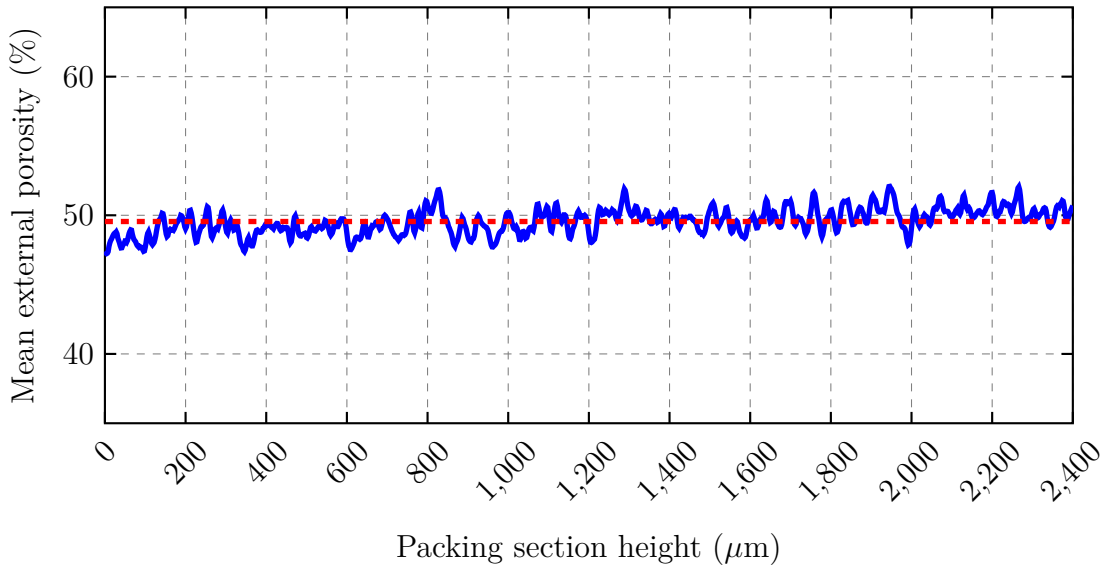

Fig. 5.14.: Porosity profile of the agarose packing along its length. Dashed line indicates overall packing porosity of 48.4 %.

The computation of the radial porosity is shown in Figure 5.15. Similarly to the PMA packing, the profile had its minimum at the respective mean radius of the particles, which in this case corresponded to $\sim 20\,\mu m$. Corresponding to the smaller particle size, the highly ordered section at the column wall is smaller and does not reach so deep into the packing. The overall mean porosity value of the complete analyzed reconstruction of 48.4 % is indicated by the dotted red line.

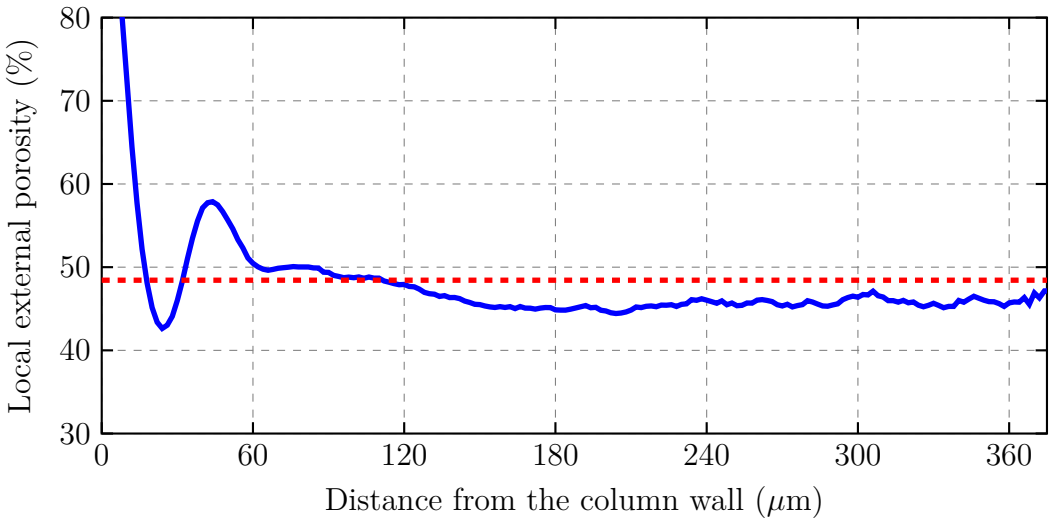

Fig. 5.15.: Radial porosity profile of the agarose packing. Blue line represents the smoothed profile ($r = 0$ corresponds to the column wall), while the dashed line indicates the overall packing porosity of 48.4 %.

The presence of voids in the top 200 µm was also exemplarily determined. Void regions with a distance equal to or lager than the mean particle radius ($\sim$ 20 µm) are highlighted in red in Figure 5.13. As with the PMA packing, it can be seen that most large voids are predominantly located on the column wall.

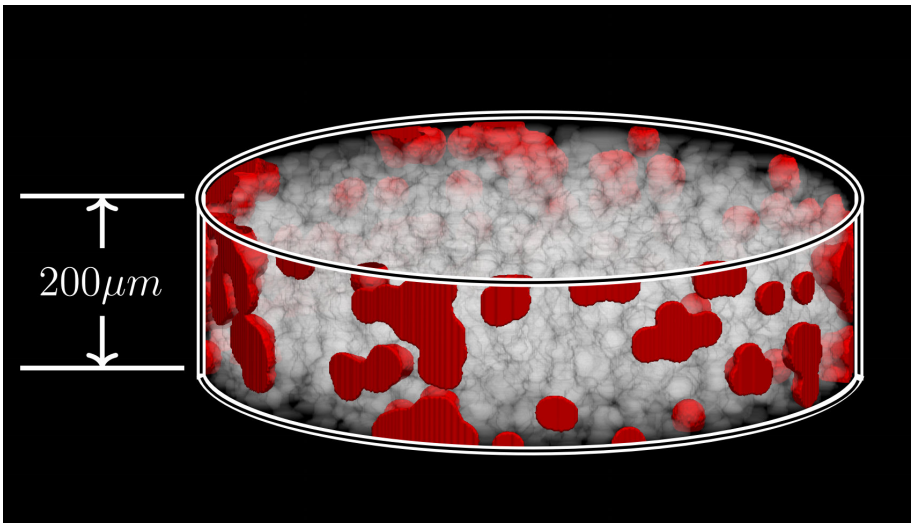

Fig. 5.16.: 3D reconstruction of the top 200 µm section of the agarose packing shown in translucent gray. Void spaces with a 3D distance equal to or lager than the mean particle radius to the nearest particle are shown in red.

5.4. Measurement of 3mm columns

The selective pore-blocking method has been successfully established at this point. The next step consisted of the use of the developed method for the measurement of bed properties under different conditions.

To do this, the custom made 3 mm column (Section 4.5.5) was employed. The initial measurement consisted of filling the column with PMA particles and flow packing the bed as previously described. The entire experiment series in the 3 mm column was carried out using the developed syringe pump (Section 4.5.7). Once flow-packed, the top flow distributor was placed on the top of the column slightly compressing it to keep it from shifting. The column was then attached to the custom-built probe holder and measured in the micro-CT. The height of the packing was 4 mm.

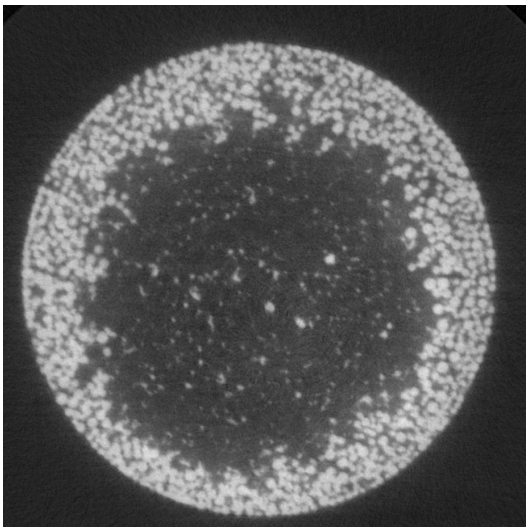

(a) Top region of the packing in direct contact with the top flow distributor. Black central region corresponds to a portion of the polymeric frit protruding from the distributor.

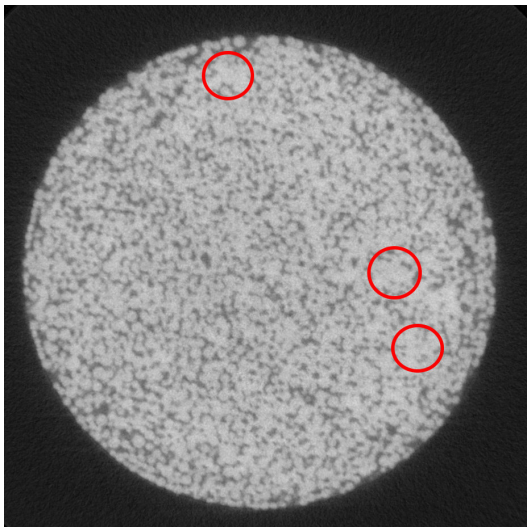

(b) Cross-section tomographic slice of the PMA packing in the 3 mm column. Pockets of coalesced hydrophilic phase can be observed.

Fig. 5.17.: Tomographs of the 3 mm column with a slightly compressed PMA packing.

Resulting tomographs can be seen in Figure 5.17. The left tomographic slice shows the intrusion of a portion of the frit into the packing apparent as the dark central region. Since the frits are manually cut and attached to the plunger, it is possible that the surface exposed to the packing is not perfectly flat. Alternatively, a steel frit with the right size can be used in the future to avoid this.

Figure 5.17b shows a cross-section of the column with several clusters of coalesced hydrophilic phase containing the contrast agent. This could be explained by the em-

ployed syringe pump. Although it was exact and able to pump against pressure drops up to 3 bar, it was not possible to set the ramping down and up of the flow as exactly as in a commercial HPLC system. This is coupled to other imitations. On one side, the maximum total volume of any phase is limited by the size of the employed syringe. Additionally, each time that the phase is to be changed, the entire column has to be manually decoupled from the syringe. In future experiments, it would be preferable to use HPLC pumping system for any procedure.

Due to the increased size of the sample in comparison to the 760 µm, the resolution was reduced to 4 µm per voxel. The images were binarised following the same steps as in the previous columns, and the porosity profiles were computed. Figure 5.18 shows the axial porosity profile. As in previous cases, there is no major deviation from the mean porosity of the packing of 50.1 %. Moreover, due to the larger amount of particles that can occupy the column cross-section, the stochastic variation of the porosity is much smaller than in narrower columns.

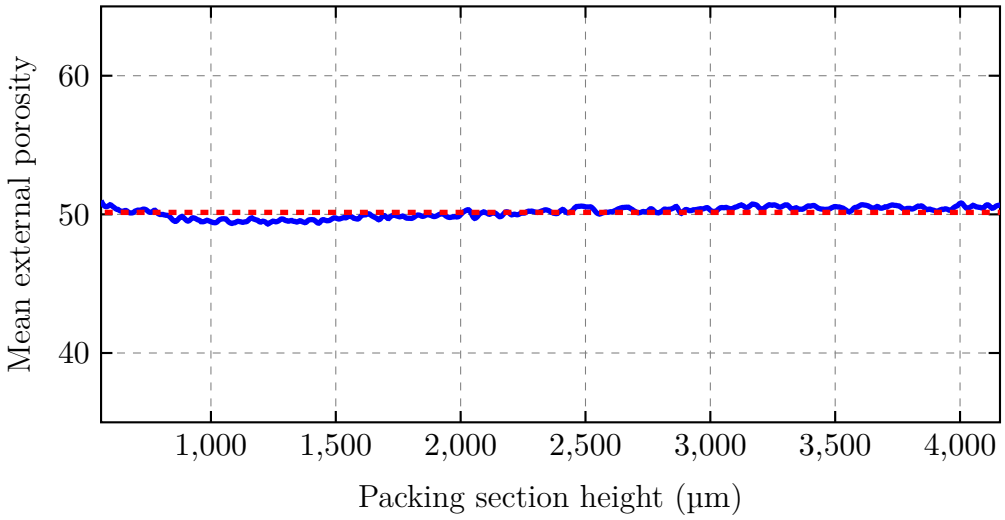

Fig. 5.18.: Axial porosity profile of a PMA packing in the 3 mm column. Dashed line represents the mean porosity of of 50.1 %.

The radial profile can be seen in Figure 5.19. Porosity oscillations can be seen at the column wall ($r = 0$), with a minimum approximately corresponding to the mean particle radius at 36 µm. These oscillations reach up to a depth of $\sim$ 300 µm, the distance at which the porosity reaches a local minimum before approaching the mean global porosity.

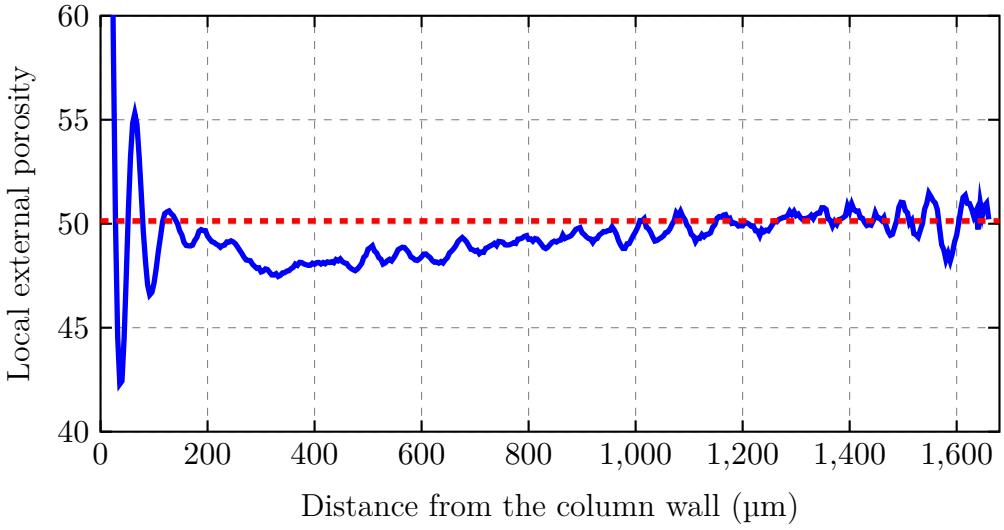

Fig. 5.19.: Radial porosity profile of a PMA packing in the 3 mm column. Dashed line represents the mean porosity of of 50.1 %.

5.4.1. Columns under mechanical compression

In this section agarose particles with particle sizes between 45 - 165 µm were used to further establish the pore-blocking method with a new particle type. The particle slurry was inserted in the column and flow-packed as in previous sections.

Two packings were made; a standard and a compressed one. In the standard case, the column was packed up to a height of 4 mm, after which the top flow distributor was placed on top of the packing with a gentle compression to keep the bed from shifting during pore-blocking and micro-CT measurement. The compressed bed was made by packing the column up to a height of 7 mm, and moving the plunger 3 mm into the bed for a final packing height of 4 mm. Both packings underwent hydrophilic pore-blocking and were measured in the micro-CT.

A comparison between the compressed and uncompressed packings can be seen in Figure 5.22. On the left, three tomographic slices of the standard bed can be compared to the same positions in the compressed bed on the right.

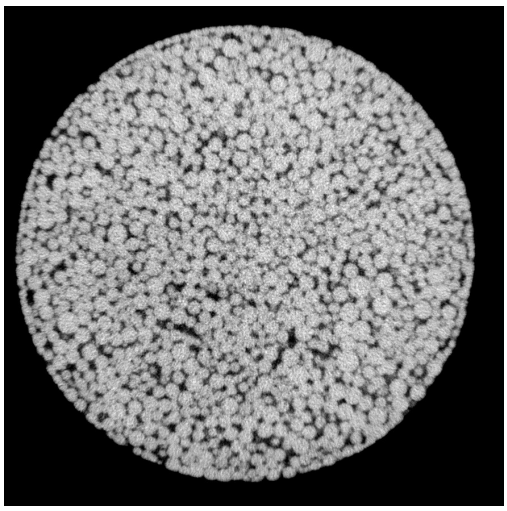

Top of the packing just under the plunger

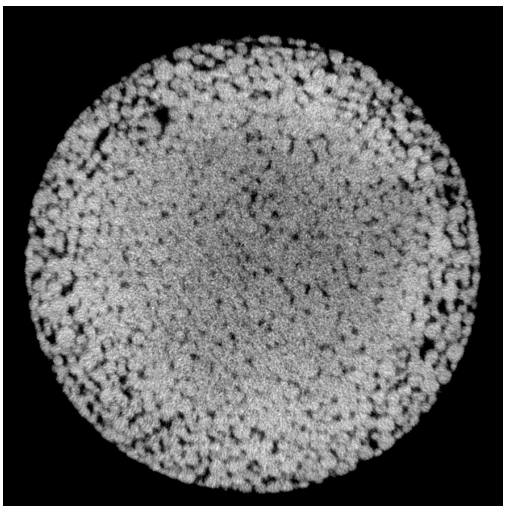

Top of the packing just under the plunger

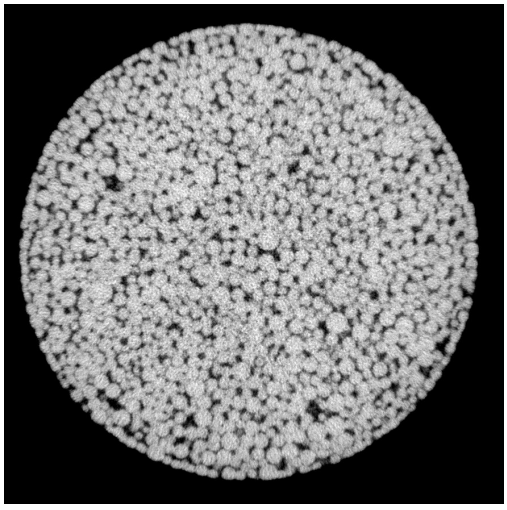

Middle of the packing

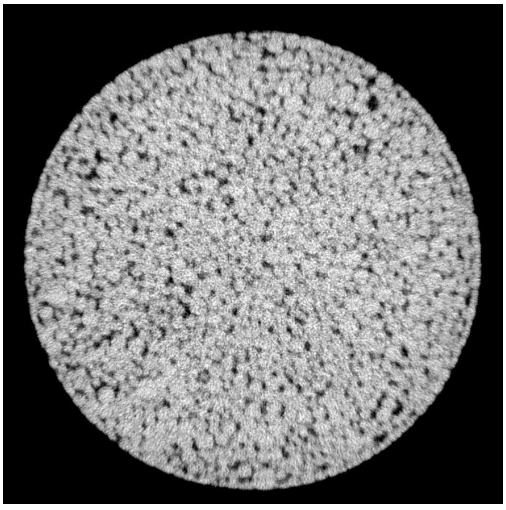

Middle of the packing

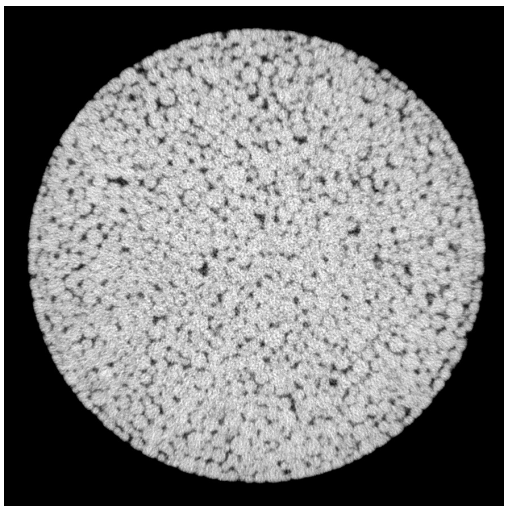

(a) Bottom region of the uncompressed packing

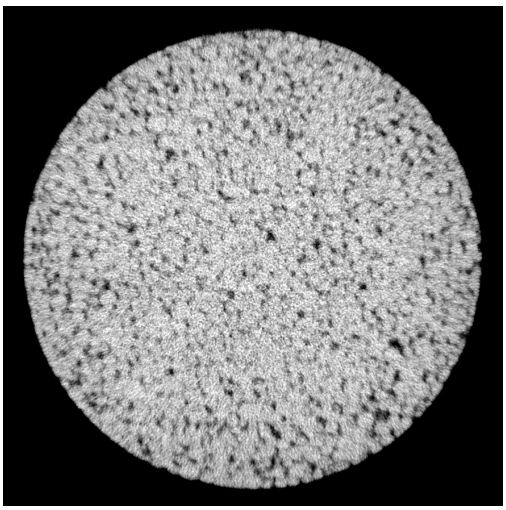

(b) Bottom region of the Compressed packing

Fig. 5.20.: Tomographic segments of two agarose packings in a 3 mm column. tomographic slices on the left correspond to a flow-packed uncompressed packing. Right tomographic slices were taken from a packing under mechanical compression from the plunger.

The most considerable difference lies in the top section of the packing, right under the plunger. In the standard bed the structure appears homogeneous in the entire cross-section. In contrast, the right tomograph shows a center region more tightly packed than a ring-like section near the column wall. This can be explained by the mechanical action of the plunger. As it is driven into the bed, the packing section under it becomes denser and pushes the particles outwards. It was observed that during the mechanical compression, a significant portion of the particles were pushed out of the packing and positioned themselves above the packing in the space between the plunger wall and the inner column wall as can be seen in Figure 5.21. This is also evident in the radial porosity profile plotted in Figure 5.22.

Fig. 5.21.: Agarose packing under mechanical compression. Particles have moved towards the gap between plunger and column wall.

The highly ordered layer at the column wall can be observed, however the entire region appears to be much less dense in comparison to the bulk of the packing, which reaches a porosity of approximately 25 %. This agrees with the observed tomographic slices showing a less dense ring-like region near the wall.

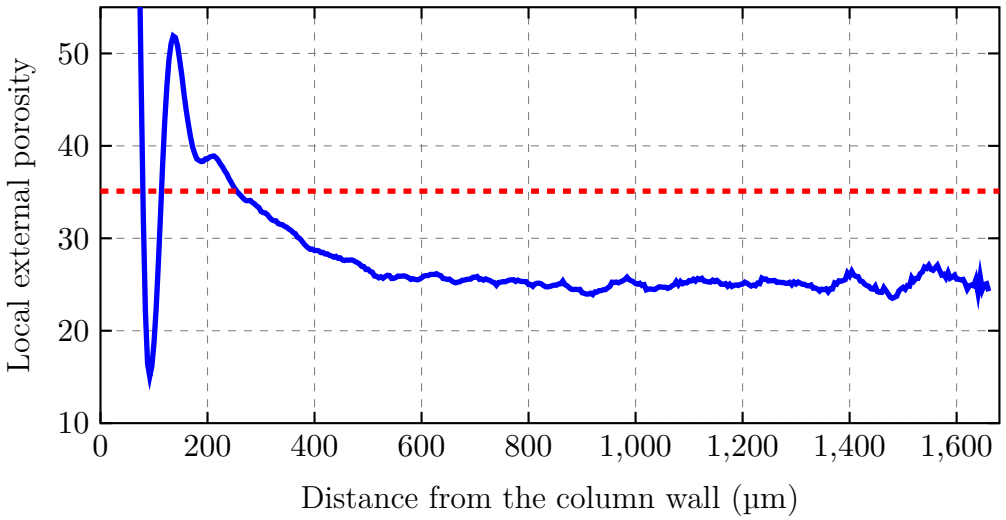

Fig. 5.22.: Radial porosity profile of the compressed agarose 3 mm column. Dashed line corresponds to the mean global porosity of 35.1 %

5.5. Particle tagging through salt precipitation

While the pore-blocking method enables the measurement of entire particle packings, the tracking of individual particles inside a packing is also of interest for the study of phenomena such as particle migration and its associated effects. With this goal a particle-tagging method based on the precipitation of a heavy X-ray absorbing silver salt inside the particle pores was developed. The particles are first saturated with a concentrated $AgNO_3$ solution. After which by addition of KI the following reaction takes place:

$$AgNO_3 + KI \quad \rightarrow AgI + KNO_3 \tag{5.1}$$

This salt is insoluble in water and precipitates forming a brown-yellow solid. Ag and I are highly X-ray absorbing atoms and should enable the measurement and tracking of salt-containing particles using the micro-CT. Disadvantages of this method are the permanent change of the particle properties, and the presence of considerable amounts of precipitated salt pieces in the initial suspension (see Figure 5.23), which prevents its use in already-packed columns.

A possible use for this technique is the permanent tagging of a small amount of particles for their posterior tracking during long-term experiments. The experimental procedure consists of filtering the unmodified particles in a vacuum filter until a wet cake is formed. The cake is washed 3 times with a 1 M $AgNO_3$ solution and vacuum

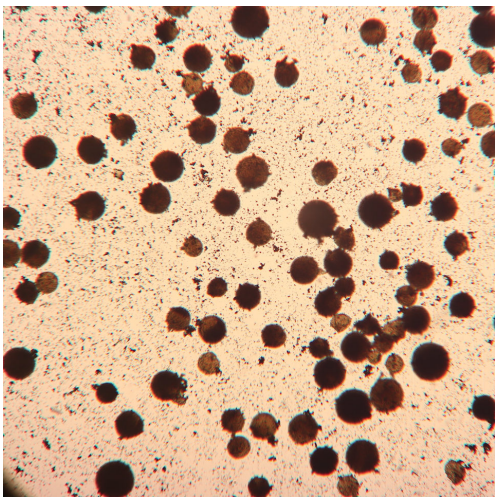

Fig. 5.23.: Initial suspension after silver iodide precipitation.

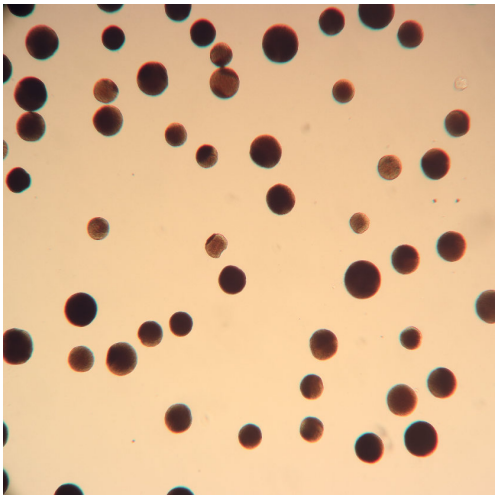

Fig. 5.24.: Cleaned suspension of tagged particles after washing.

filtered after each washing as to obtain a wet compact cake. The same procedure is repeated with a 1 M KI solution, during which the precipitation reaction takes place. At this point the cake has a yellow appearance, and is resuspended in a 10 mM NaOH solution forming a particle slurry. AgI precipitates in and between the particles (Figure 5.23).

To remove the salt pieces, the particle slurry containing tagged particles and salt precipitates is diluted one to ten with a solution of 10 mmol NaOH. The diluted slurry is resuspended and allowed to sediment for one minute, after which the supernatant is removed. This washing step is repeated 10 times to achieve a suspension of tagged particles with little to none salt precipitate (Figure 5.24).

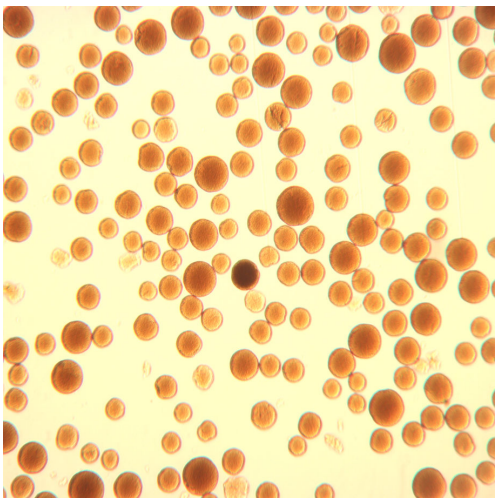

Fig. 5.25.: Suspension containing 1 % of tagged particles.

With this cleaned suspension it is potentially possible to follow changes in the microscopic structure by tracking individual particles and study migrating behavior. This can be achieved by combining a small set of AgI-tagged particles with the bulk of unmodified ones (e.g $< 0.1\%$ of modified particles as seen in Figure 5.25), the changes in position and trajectories of the marked particles can be followed as the column experiences simulated separation cycles.

6. Novel methods for packing of chromatographic columns [2]

6.1. Ultrasound-packing

A 50 % slurry of polymethylacrylate (PMA) particles (d_p = 65 µm) in the 50 mm column was allowed to sediment to form a bed with a column height to diameter ratio $^{H}/_{D}$ = 1. Once the particles settled, the ultrasound transducer located in the bottom flow distributor (as seen in Figure 4.6) was turned on and the compaction monitored optically.

The application of ultrasound caused no change in the packing. Additional experiments with ceramic hydroxyapatite (CHT) particles also showed no or very little effect of ultrasonic vibrations in already consolidated beds.

A possible explanation is that the magnitude of the generated ultrasonic waves was not high enough to overcome the frictional resistance of the particles in the consolidated packings to accomplish particle rearrangement. It was however noted that, although ultrasound irradiation has no effect on the compaction of an already settled packing, it has an effect on the behavior of a sedimenting slurry.

6.2. Ultrasound-assisted sedimentation

The behavior of a suspension of chromatographic particles was studied during sedimentation in an ultrasonic field. PMA particles were chosen due to their slower gravity settling velocity of 20 $^{cm}/_{h}$ [9] in comparison to ceramic hydroxyapatite (CHT) particles at 180 $^{cm}/_{h}$ [10] which would settle too quickly. Enough particles to achieve a packed

[2] This chapter contains information published in: A. Martinez, K. Knaub, M. Monter, D. Hekmat, D. Weuster-Botz. Improved packing of preparative biochromatography columns by mechanical vibration. Biotechnology Progress. 2020;36:e2950. DOI: 10.1002/btpr.2950

bed height H = 50 mm ($^{H}/_{D} = 1$) were introduced in the column containing the flow distributor with the ultrasound transducer. Column height was set to 100 mm to achieve a slurry concentration of 50 % after resuspending the packing which was achieved by applying flow in the upward direction and slightly tapping the outer column wall. Upward flow was stopped once the slurry reached a distance of around two millimeters below the top flow distributor. Once a homogeneous suspension was achieved, the particles were allowed to settle either by gravity only or in the presence of an ultrasonic field. The settling of the particle slurry was followed optically (see Figure 6.1).

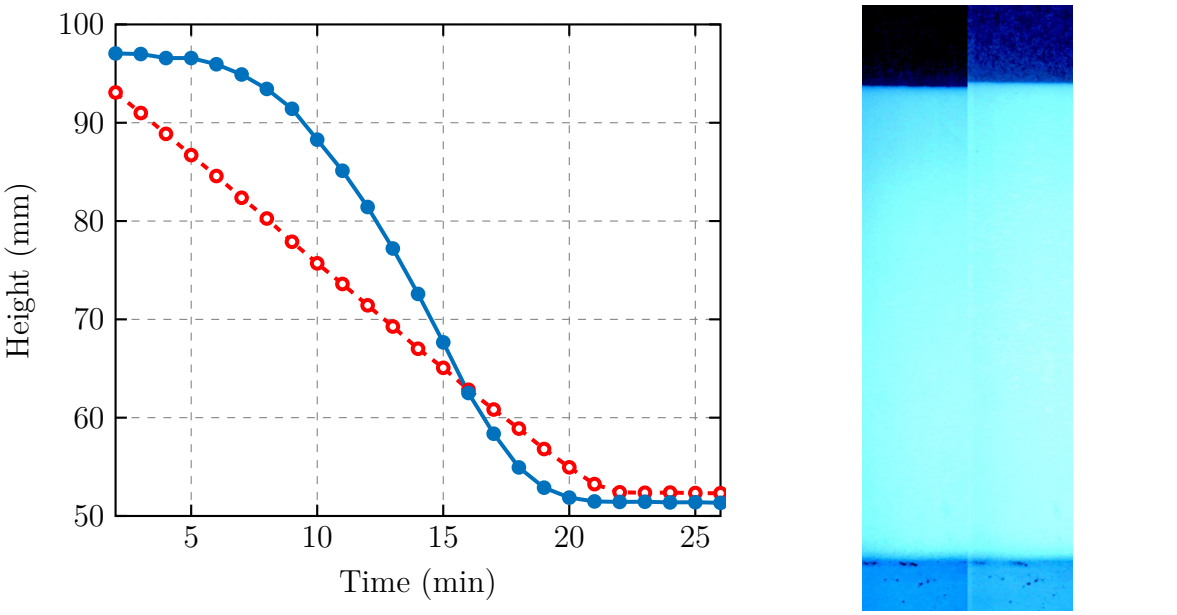

(a) Settling curve with (solid line) and without ultrasound (dashed line) for a PMA particle slurry.

(b) Final settled bed. LEFT: settling under ultrasound, RIGHT: gravity-only.

Fig. 6.1.: Sedimentation progression and end state for ultrasound and gravity-only settling. Note the final height difference in both figures.

The time course during ultrasound settling was sigmoidal. Sedimentation was slow in the beginning and increased with time. A relatively high sedimentation rate was observed before the final packing height was reached. In contrast to this, the time course of the gravity settling was linear at a lower sedimentation rate until the final packing height was reached. The obtained ultrasound-assisted packing consolidation was $\sim$ 1 % higher compared to gravity settling (see Figure 6.1b)

The change in sedimentation velocity can be seen in Figure 6.2. In the ultrasound case, the velocity is approximately zero for the first five minutes of settling, after which it starts increasing until reaching and surpassing the gravity-only velocity.

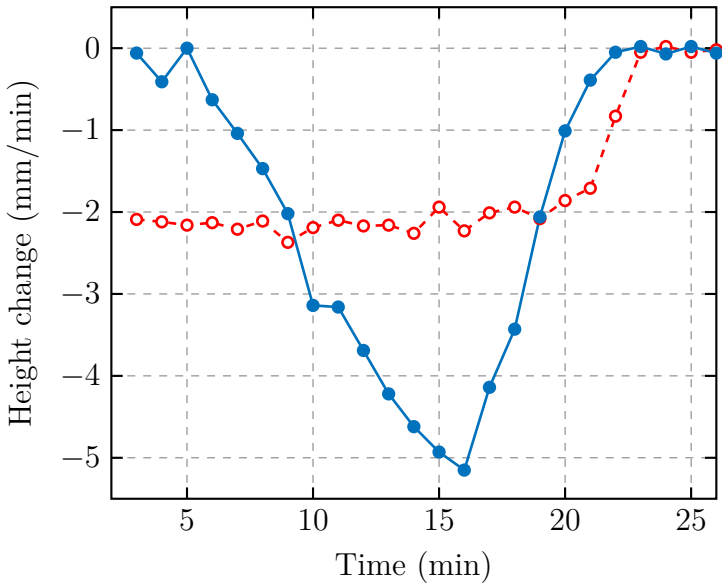

Fig. 6.2.: Settling velocity of (solid line) ultrasound-assisted sedimentation, and (dashed line) gravity-only.

As the slurry settles, horizontal planes parallel to the ultrasonic active face in which the particles accumulated were observed (see Figure 6.3). These planes correspond to the Gorkov potential nodes of the generated acoustic field. It was observed that the clustering of the particles in the planes eventually reached a point in which weight of the clusters overcame the acoustic field, and the particles sedimented. If the ultrasonic transducer was turned off, the acoustic field would disappear, and all particles held in the planes would sediment.

6.2.1. Mechanism of action

The ultrasound-assisted settling behavior can be explained by the acoustic effects. In general, the application of an ultrasonic field in a fluid can generate two distinct phenomena: acoustic streaming and acoustic radiation forces [88]. Both arise from the propagation of the waves, and the formation of pressure and velocity fields inside the column.

Acoustic streaming

Acoustic streaming corresponds to fluid movement which arises from the attenuation of sound waves as these propagate in the medium. Such attenuation causes a decrease of the wave pressure as its energy is transformed into heat. A simulation of the pressure

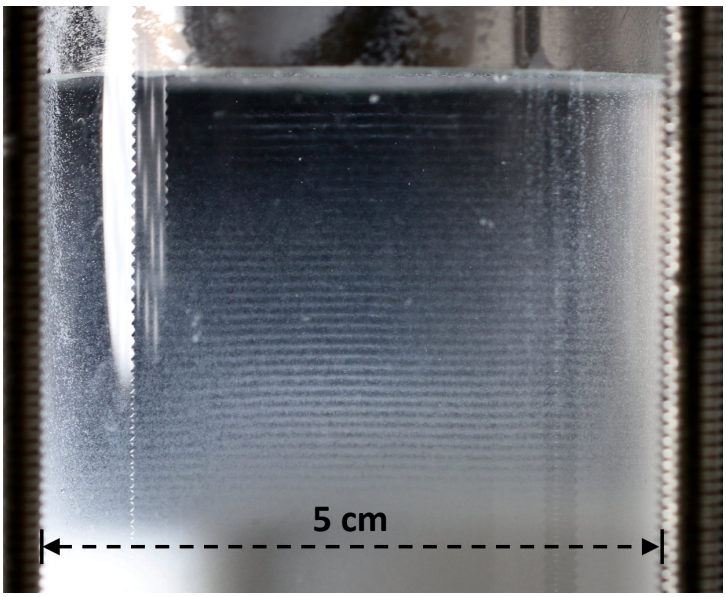

Fig. 6.3.: Particle suspension settling under ultrasound. Particle layers accumulate along pressure planes.

field in the 50 mm column caused by the employed transducer can be seen in Figure 6.4 and was done using the software from Section 4.6.3.

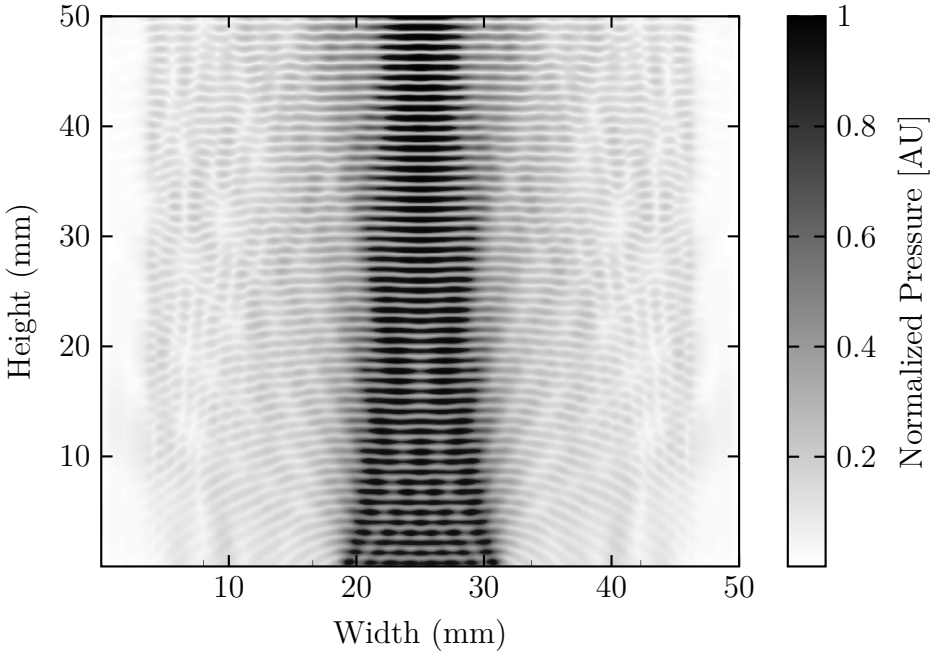

Fig. 6.4.: Pressure field generated by the ultrasonic transducer inside the 50 mm column.

The front of the transducer forms a high pressure zone (bottom region). As acoustic energy diminishes along its trajectory, zones of low pressure are formed. Thus, a net

fluid movement from high to low pressure regions is created with an orientation perpendicular to the transducer face. Since in our case the transducer was located at the bottom of the column with an upward propagation direction, acoustic streaming acted against gravity and resulted in a delayed initial settling behavior.

Additional flow circulation takes place from the central high-pressure axis towards the outer region of low acoustic pressure. Due to the resonant characteristics of the system, it is to be expected that fluid convection also takes place from the horizontal high pressure planes (black and gray horizontal regions in Figure 6.4) towards the lower pressure planes (white regions). Overall, the combination of different types of convection keeps the particles in suspension longer through viscous drag, allowing for a longer working time before settling fully takes place.

Acoustic radiation forces

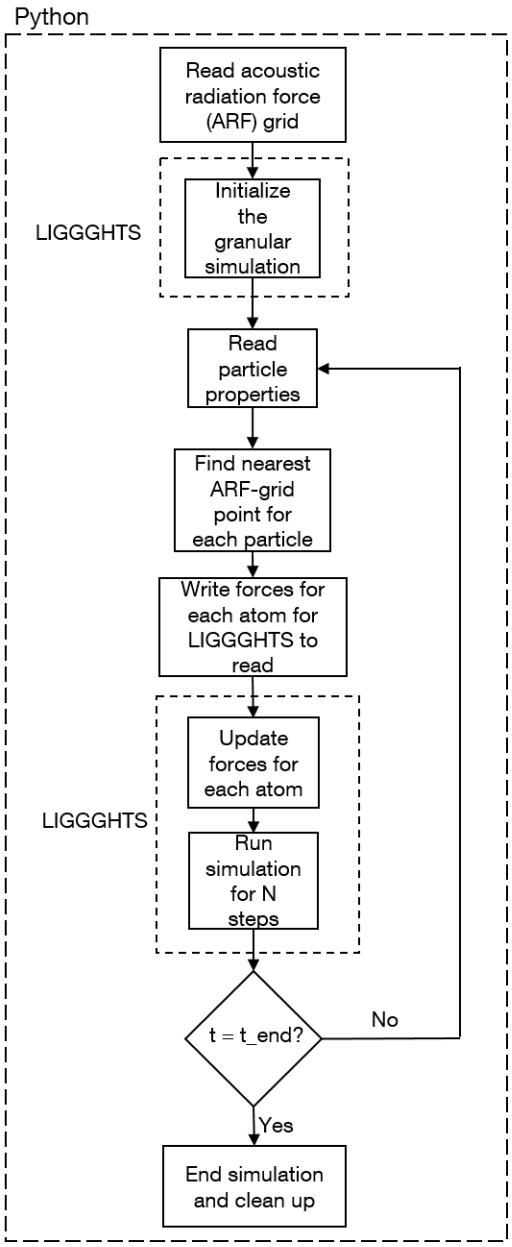

Fig. 6.5.: Simulation algorithm.

An algorithm for the simulation of granular behavior in ultrasonic fields was developed with the software from section 4.6.3. The algorithm relies on a python script that reads the properties of each particle (radius, position and contrast factor) and calculates the acoustic radiation force according to a previously simulated Gorkov potential. No analytical solution of the wave-equation is required to find the second-order acoustic field. This algorithm is laid out in Fig. 6.5 and consists of:

- **(a)** Simulation of the first-order acoustic field in Matlab
- **(b)** Calculate the second-order field based on the data from (a)
- **(c)** Taking the material properties into account, calculate the acoustic potential according to equation 3.15
- **(d)** Acoustic radiation forces are calculated based on the acoustic potential
- **(e)** The coupling of information obtained from ultrasound simulations and LIGGGHTS takes place using a python interface.

Using this algorithm, a granular simulation in LIGGGHTS including the acoustic radiation forces can be made. Exemplarily, the central high-pressure region was simulated reproduce the particle layering effect at the pressure planes (seen in Figure 6.6b).

Future scale-up of ultrasonic-assisted settling in larger industrial columns will most likely require the use of several ultrasonic transducers in a single column. The developed algorithm can aid the design of the position and size choice of the transducers, as well

as the signal strategies that can be employed. Explored ultrasonic signals so far have been continuous at a constant frequency. With the presence of several transducers in larger scale columns it is possible to employed delayed pulses to target a specific region of the packing. Such events can be modeled employing the developed algorithm.

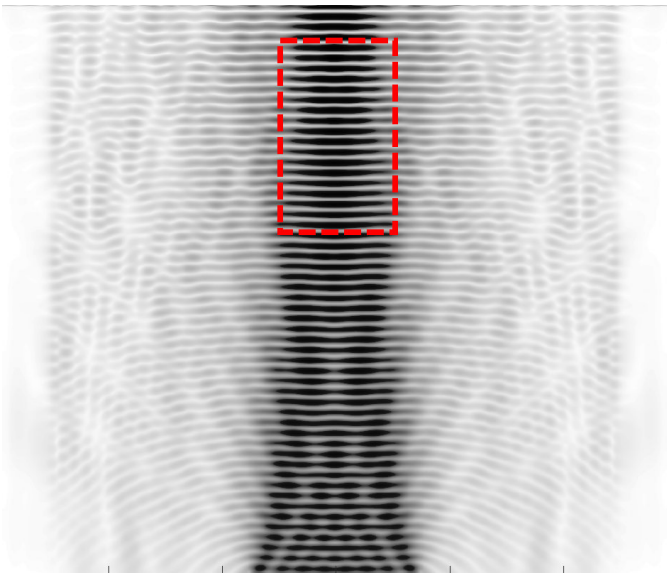

(a) Simulation of the pressure field generated by the ultrasound transducer. Pressure and velocity in the red dashed square are used in equation 3.15.

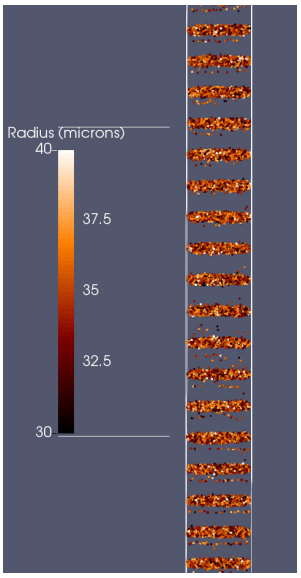

(b) Grain stratification in the pressure planes from **(a)** simulated by including acoustic radiation forces (see section 3.2.2) in LIGGGHTS.

Fig. 6.6.: Simulation of a granular suspension in a pressure field reproducing the indicated region in Figure 6.3

Overall, ultrasonic waves did not deliver enough energy to further compact settled beds. A possible explanation for this are the high acoustic losses at the transducer-mobile phase interface. Mainly due to the high reflection factor of 88 % (Equation 3.13), effective acoustic work in the column was approximately 76 $^{\text{Watt}}/_{\text{l}}$, based on the particle slurry volume, or 152 $^{\text{Watt}}/_{\text{l}}$ based on consolidated bed volume. Consequently, the application of mechanical vibration using pneumatic vibrators for the packing of already consolidated beds was explored. These not only have larger amplitudes than ultrasonic waves but also experience lower acoustic attenuation which is proportional to the wave frequency. While ultrasonic waves propagate at frequencies starting at 20 kHz, pneumatic vibrators commonly oscillate in the 100 Hz range. Hence, mechanical vibration can deliver higher energy and the mechanical waves are less attenuated as they propagate.

6.3. Mechanical vibration

Several approaches were explored, including direction (vertical and horizontal) and type (rotational and linear) of vibration. Horizontal vibrations enter through the walls of the column, while vertical vibrations do so through the bottom flow distributor.

6.3.1. Preliminary vibration experiments

Sedimented bed experiments

The first approach was to evaluate the maximal possible additional compaction achievable by lateral vibration. This was done by allowing the bed to sediment before applying vibration. After the suspension was homogenized, the particles were left to sediment under gravity. Pictures were taken every 2 minutes and the height was measured with help of previously engraved markings made at H = 8, 9, 10, 11, 12 cm (white horizontal lines in 6.7) and a Matlab script.

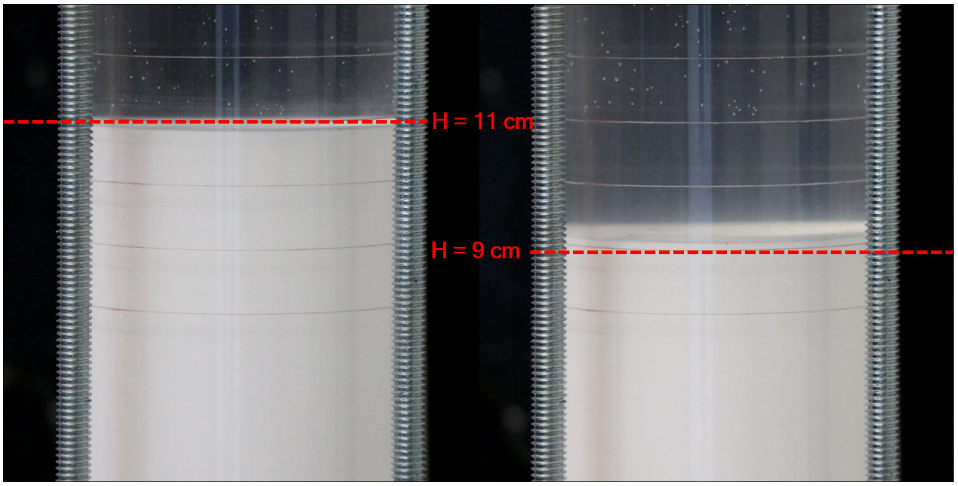

Fig. 6.7.: Final heights of a settled CHT column. **(left):** after settling. **(right):** after vibration.

Once the bed reached a constant height, vibration was started. Using the adapters shown in Figure 4.7, one K-8 ball vibrator was attached to the column at a height of $\sim$ 1 cm, and operated using pressurized air at 2 bar. This air entered and exited the pneumatic vibrator only and did not come in direct contact with the column or the packing. Vibration was applied until no appreciable bed compaction took place. The change in height in time can be seen in Figure 6.8 for CHT and in Figure 6.9 for PMA particles. The first height plateau near the 10 minute mark represents the settled bed

height. Vibration was turned on shortly before the 30 minute mark. After vibration started, the bed starts compacting and a linear compaction behavior appears near the 35 minute mark. The final compacted bed height is approached asymptotically after a total vibration time of 60 minutes. This behavior agrees with the granular compaction theory in Section 3.2.1.

The experiment was stopped when no appreciable additional compaction was observed. The settled bed height and the maximally compacted bed height achieved in the same experiment can bee seen in Figure 6.7. In average, the height compaction of gravity-settled beds employing vibration reached 15.6 %, which indicates a change of the porosity of 26 % from an assumed initial porosity of ~ 0.41 down to 0.3.

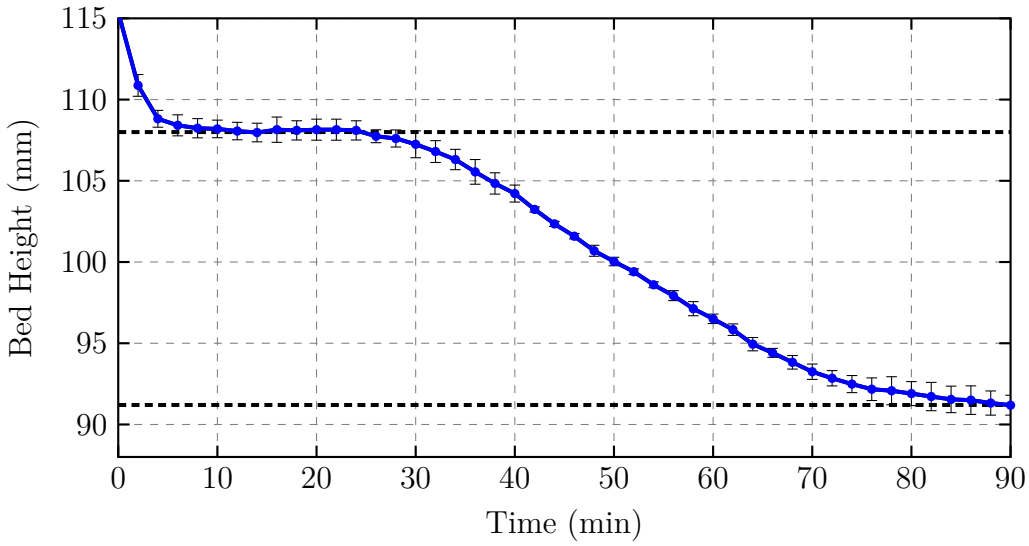

Fig. 6.8.: Compaction of a settled bed of CHT particles caused by external horizontal vibration of a single K-2 ball-vibrator (N=3). Vibration start at t = $\sim$ 30 min. $\Delta H = 17mm$ $(15,6\%)$.

The vibration compaction of a PMA packing (see Figure 6.9) is similar to the one shown by CHT packings. The total and relative compaction is larger, as well as the compaction time, which amounted to approximately 110 minutes. In average, the height compaction of gravity-settled beds employing vibration reached 17.3 %, which indicates a change of the porosity of 30 % from an assumed initial porosity of ~ 0.41 down to 0.29.

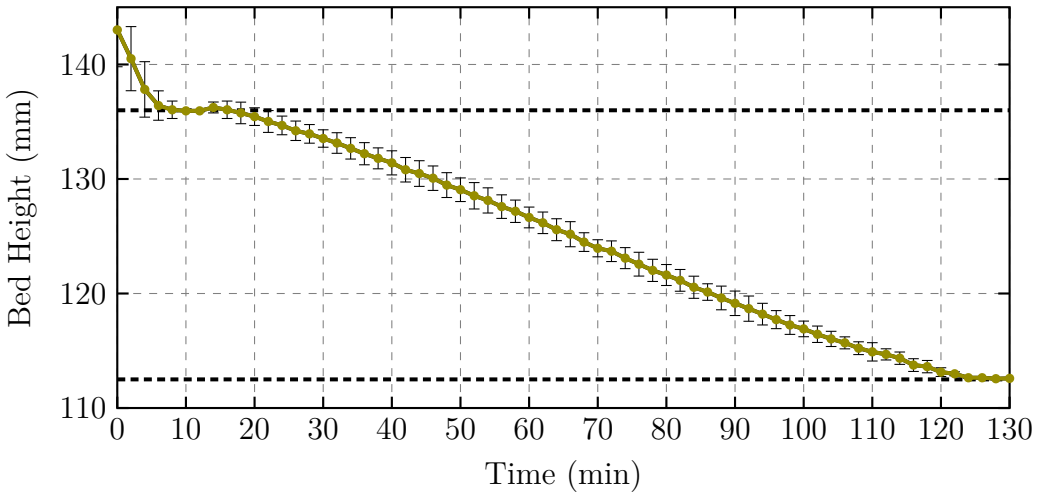

Fig. 6.9.: Compaction of a settled bed of PMA particles caused by external horizontal vibration of a single K-2 ball-vibrator (N=2). Vibration start at t = $\sim$ 15 min. $\Delta H = 23,5mm$ $(17,3\%)$.

It can be concluded that employing pneumatic vibration considerably compacted gravity-settled beds for both PMA and CHT particles. It is well understood that gravity settled beds have higher porosities than packings packed following conventional flow or mechanical compression mechanisms. Besides achieving denser beds, size segregation during sedimentation is avoided during such packing steps. Thus, the next step consisted of the use of pneumatic vibration on consolidated beds packed with conventional methods instead of gravity settling.

Consolidated bed experiments

To study more realistic and relevant packing methods, the particle suspension was immediately consolidated with a specific flow-rate after it was fully resuspended. Two cases were explored, de-coupled vibration and coupled vibration. The goal was to study the effect of simultaneous fluid flow through the bed as vibration was applied. During de-coupled vibration, the packing flow was held for 2 minutes after which it was stopped and the vibration started. During coupled vibration, the flow and vibration are started at the same time and are on during the complete experiment. Vibration was generated with one K-8 vibrator attached horizontally to the column and the same pressurized air parameters as the previous section.

Consolidation at 300 $\frac{cm}{h}$ - De-coupled - vibration after consolidation: After 2 minutes of flow packing, vibration was turned on. Compaction for CHT and PMA can be seen in Figure 6.10 and 6.11 respectively.

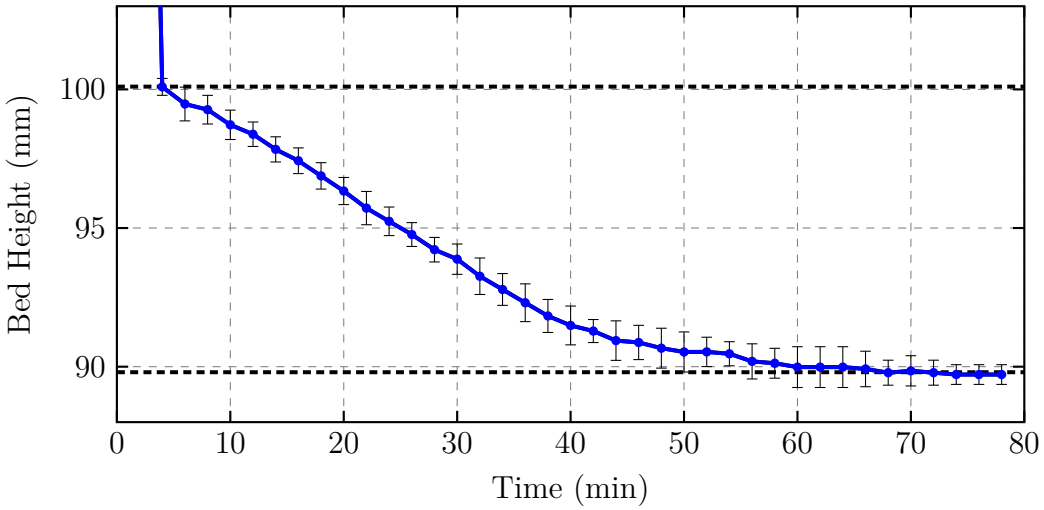

Fig. 6.10.: Compaction of a packed bed of CHT particles caused by external horizontal vibration of a single K-8 ball-vibrator (N=2). Vibration start at t = $\sim$ 5 min. $\Delta H = 10.9mm$ (10.2%).

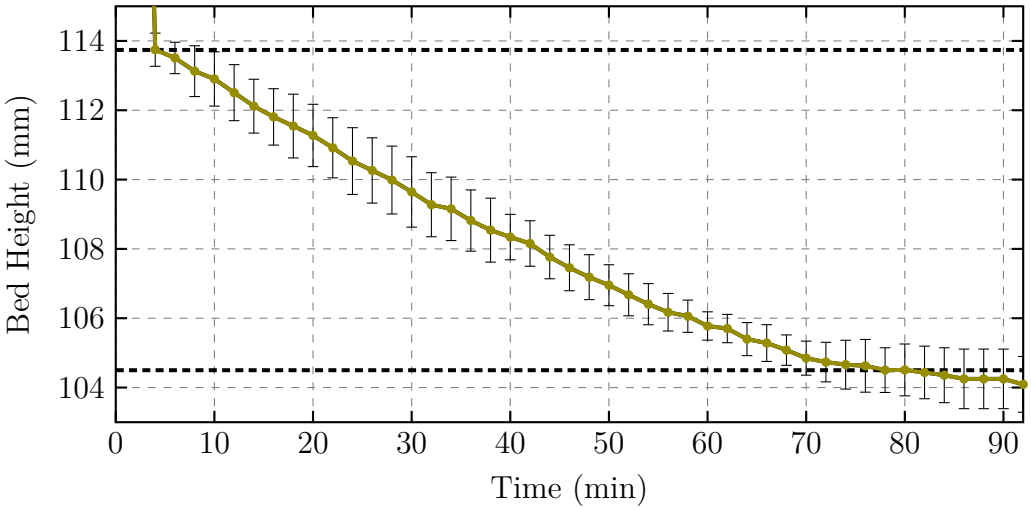

Fig. 6.11.: Compaction of a packed bed of PMA particles caused by external horizontal vibration of a single K-8 ball-vibrator (N=3). Vibration start at t = $\sim$ 5 min. $\Delta H = 9,6mm$ (8,4%).

For both particle types a considerable additional compaction through vibration was achieved. As was expected, the compaction was smaller in comparison to the gravity-settled case. This is explained by the initial state of the consolidated bed. Since this

packing was packed with flow, the porosity was smaller than in the gravity-settled case, thus having a smaller compaction potential. The contrast in compaction difference between packed and gravity-settled beds (from 15.6 % to 10.2 % for CHT and from 17.3 % to 8.3 % for PMA) can be explained by the difference in sedimentation velocity between them. As CHT has a fast settling velocity, the states of CHT packings obtained through flow and gravity packing are relatively similar in comparison to PMA. For the latter these states are widely different, as can be seen by the large change in vibration compaction.

Consolidation at 300 $\frac{cm}{h}$ - Coupled - vibration during consolidation: The flow and vibration were started at the same time and held during 90 minutes. No appreciable change in the column height could be observed, thus no height vs. time figure is made. The lack of any appreciable compaction for a CHT column can bee seen in Figure 6.12.

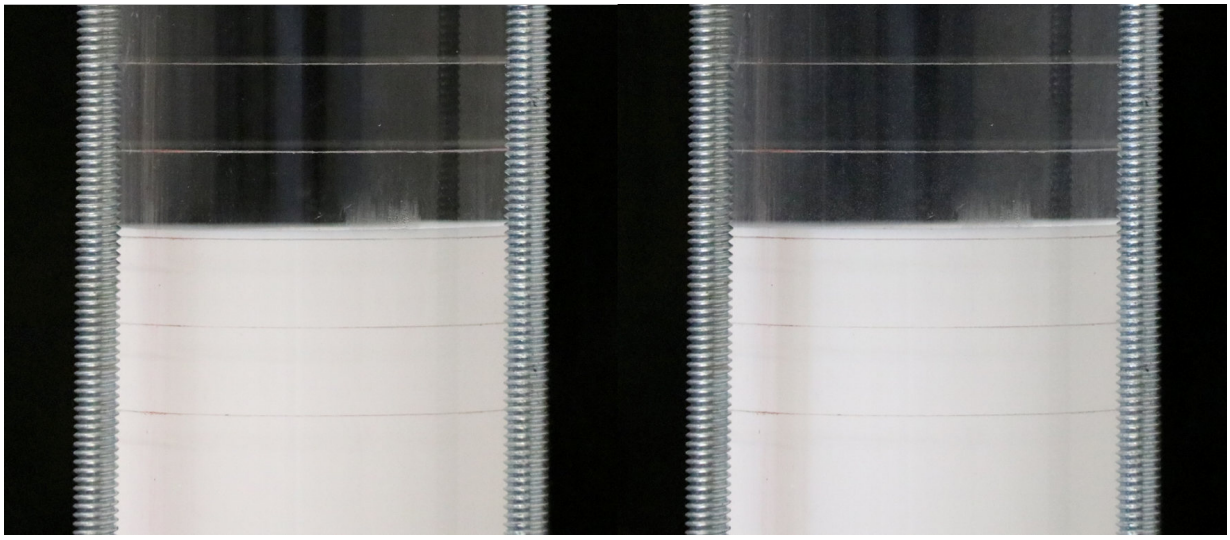

Fig. 6.12.: CHT column undergoing coupled flow-packing ($300\frac{cm}{h}$) and vibration. **(left):** initial bed height at t = 4 min. **(right):** final bed height at t = 60 min.

The lack of compaction with simultaneous flow indicates that the viscous drag of the fluid acted as a stabilizing force, keeping the packing in place due to increased particle-particle friction. Although initially counter-intuitive, this results complements existing literature which indicates that it is possible to further consolidate a packed bed by only applying a small *upward* flow through the packing [44].

Consolidation at 600 $\frac{cm}{h}$ - De-coupled - vibration after consolidation: Coupled and de-coupled vibration experiments were also carried out with an increased flow rate. The flow-packing volume rate was doubled and held for the same period of time (2 min).

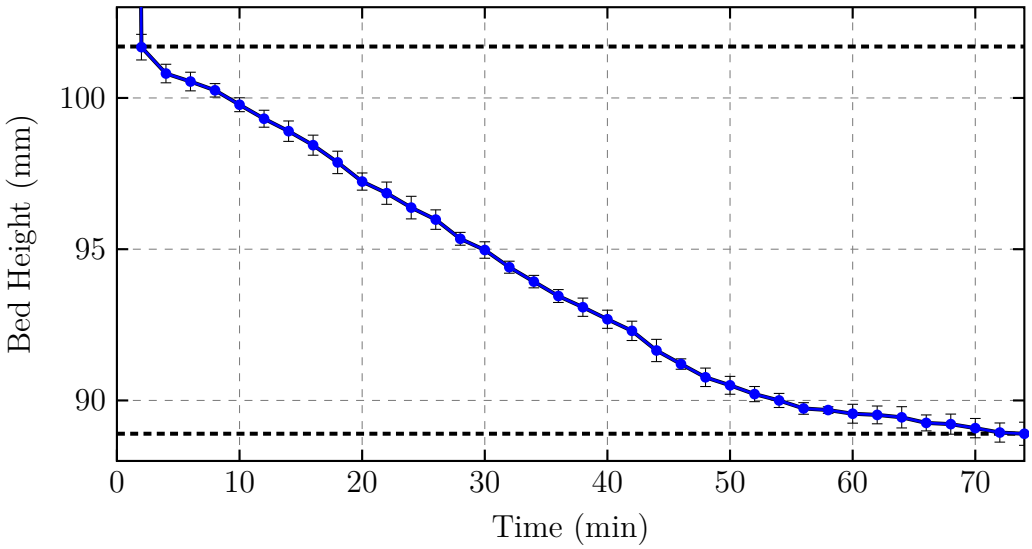

Fig. 6.13.: Compaction of a packed bed of CHT particles caused by external horizontal vibration of a single K-8 ball-vibrator (N=2). Vibration start at t = $\sim$ 5 min. $\Delta H = 12,8mm$ $(12,6\%)$.

Once flow stopped, vibration was turned on. Compaction for a CHT column can be seen in Figure 6.13.

The initial height of the bed consolidated at 300 $^{cm}/_{h}$ was larger than at 600 $^{cm}/_{h}$. Although also counter-intuitive, it is well understood that larger packing velocities do not necessarily deliver denser, better packed beds. As the packing velocity increase and the particles are pushed down onto the surface of the growing bed, these do not have enough time to impact and roll into an existing neighboring void space before other particles fall on them, locking them in place. Thus, the initial state has a larger of unoccupied void spaces, explaining why both the total and relative compaction increased in comparison to the 300 $^{cm}/_{h}$ flow-packing.

Consolidation at 600 $\frac{cm}{h}$ - Coupled - vibration during consolidation: The flow and vibration were started at the same time and held during 90 minutes. No appreciable change in the column height could be observed, thus no height vs. time figure is made. The lack of any appreciable compaction for a CHT column can bee seen in Figure 6.14.

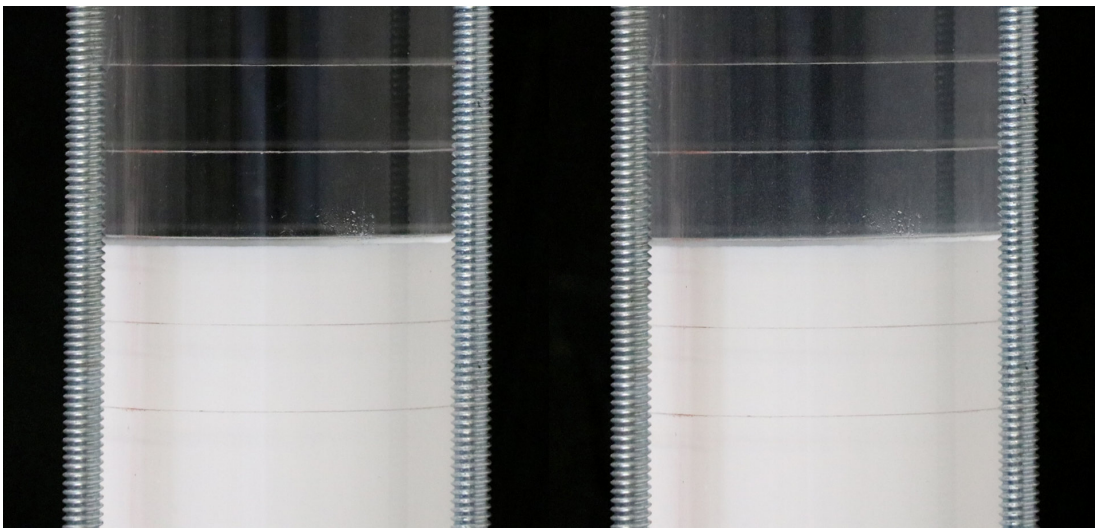

Fig. 6.14.: CHT column undergoing coupled flow-packing (600 $^{cm}/_{h}$) and vibration. **(left):** initial bed height at t = 4 min. **(right):** initial bed height at t = 60 min.

As in the coupled case with 300 $^{cm}/_{h}$, the packing undergoes no compaction and appears to be stabilized by the flow. Since the flow acts with a net downwards force, the granular arches support the bed structure by transmitting the force to the column wall. The increased granular pressure thus causes a higher friction force between the particles, which can not be overcome by the propagating wave.

Effect of vibration on packing homogeneity

The potential of additional compaction of conventionally packed beds employing pneumatic vibration was established. However, a more compact bed does not necessarily implies a more efficient bed. It is also necessary for the microstructure not to become heterogeneous through the compaction mechanism or at least retain its homogeneity. Thus the chromatographic efficiency of standard and vibration-packed beds were measured by carrying out pulse injection experiments and deriving the HETP. The focus was on the study of the effect of lateral or axial vibration, and the use of linear or rotational vibrators. All experiments in this and subsequent sections were carried out using de-coupled vibration and the vibrators were operated with pressurized ar at 2 bar unless stated otherwise.

Polymethylacrylate packings

Standard packing - no vibration - 300 $\frac{cm}{h}$: A standard bed was packed without any vibration. The bed was then left untouched for the same amount of time as if vibration took place before carrying out the probe injections.

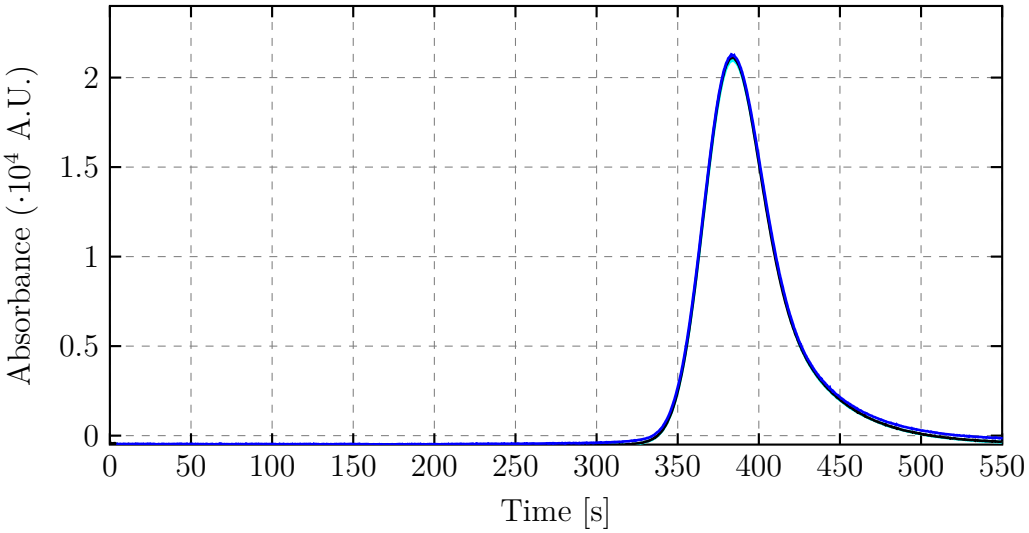

Fig. 6.15.: Elution chromatograms of a PMA bed packed using no vibration.

De-coupled vibration - 300 $\frac{cm}{h}$ - Lateral vibration: one K-8 rotational vibrator was attached laterally to the column and turned on as explained in the previous section. After the additional compaction was achieved, elution chromatograms were measured using the procedures explained in Section 3.1.2.

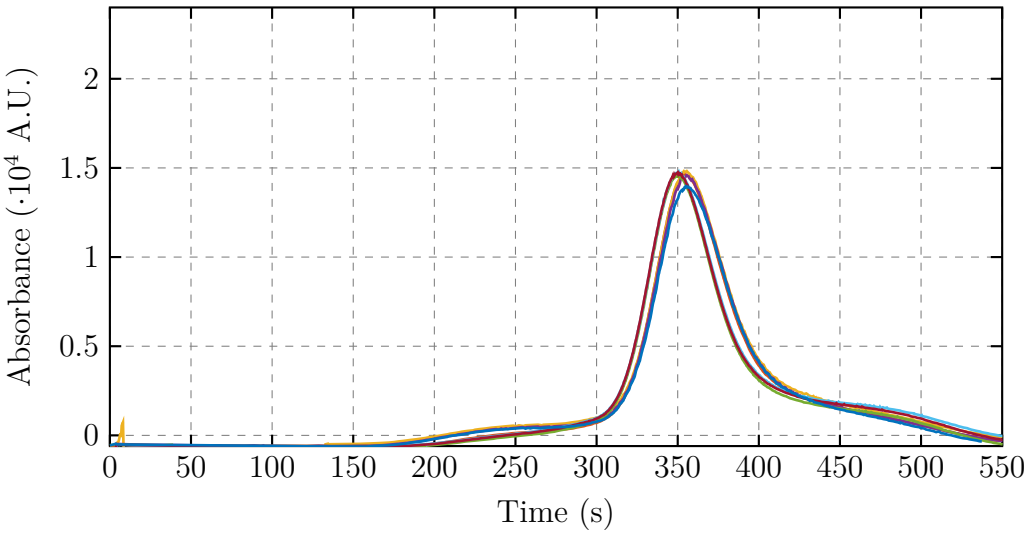

Fig. 6.16.: Elution chromatograms of a PMA bed packed using de-coupled vibration.

The resulting chromatograms appear to be the addition of two peaks, a broader one corresponding to a less dense and more heterogeneous region, and a narrower one possibly corresponding to a more homogeneous and denser region. This result indicates the presence of two distinct domains of the column with different micro-structural properties. Even though the vibrated beds are macroscopically denser and appear homogeneous, due to the apparent microscopic heterogeneities, these are not more efficient than conventional packed columns.

Ceramic hydroxyapatite packings

Standard packing - no vibration - 300 $\frac{cm}{h}$: A standard bed was packed without any vibration. The bed was then left untouched for the same amount of time as if vibration took place before carrying out the probe injections.

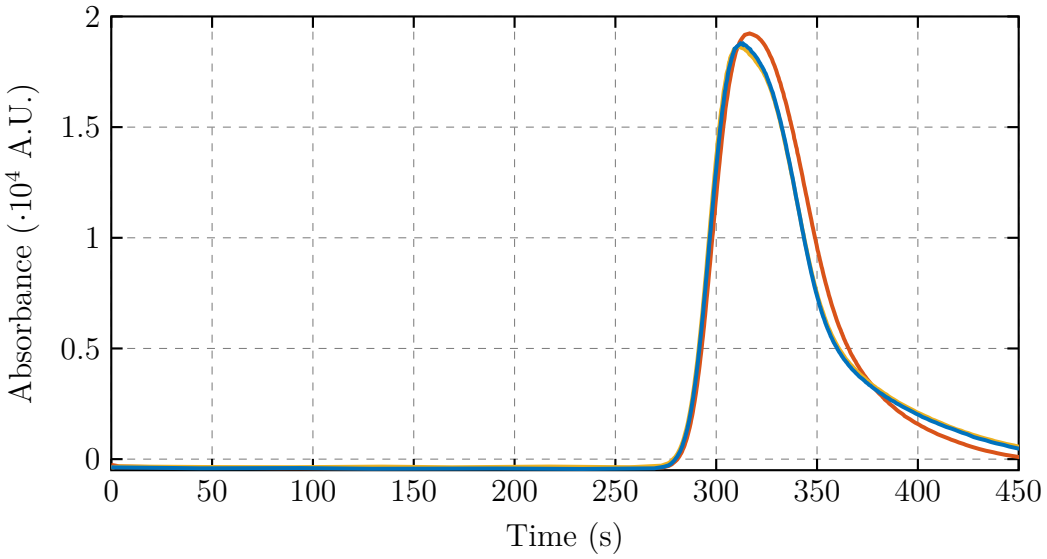

Fig. 6.17.: Elution chromatograms of a CHT bed packed using no vibration.

As expected, the peak has the characteristic shape of an unretained compound, albeit with a slight tailing due to the extra-column volume in the system.

De-coupled vibration - 300 $\frac{cm}{h}$ - Lateral vibration:

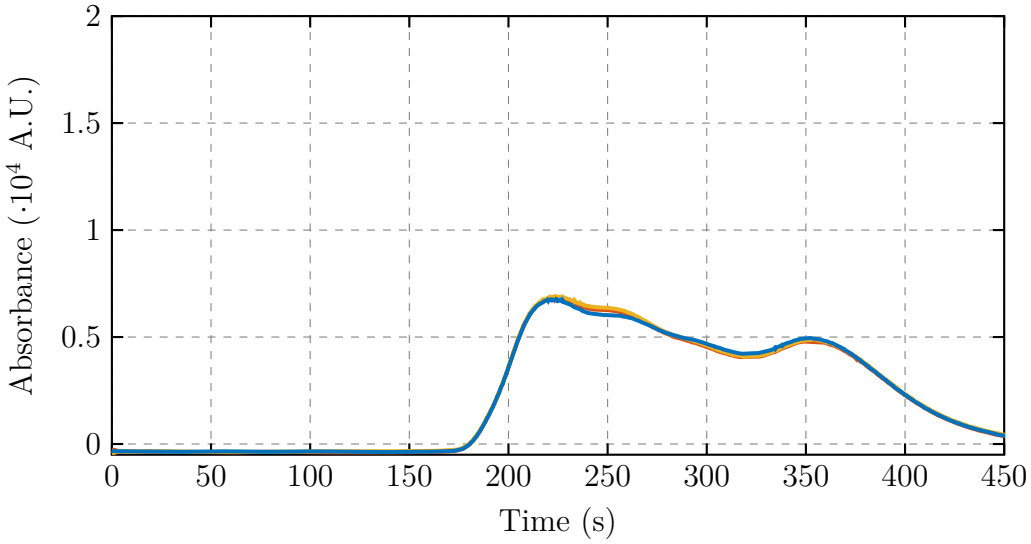

Fig. 6.18.: Elution chromatograms of a CHT bed packed using de-coupled vibration.

Similarly as for the PMA particles, CHT packings which were compacted using lateral vibration appear to deliver less efficient columns. In this case, several peaks are observed, which would indicate a severely heterogenous microstructure. As in the previous case, no macroscopic heterogeneities were observed.

De-coupled vibration - 300 $\frac{cm}{h}$ - Lateral vibration: A second K-8 vibrator was attached to the other side of the horizontal holder. It was proposed that since only a single K-8 vibrator had been employed so far, the observed inhomogeneities could be caused by the region near the vibrator being denser than the region at the opposing side.

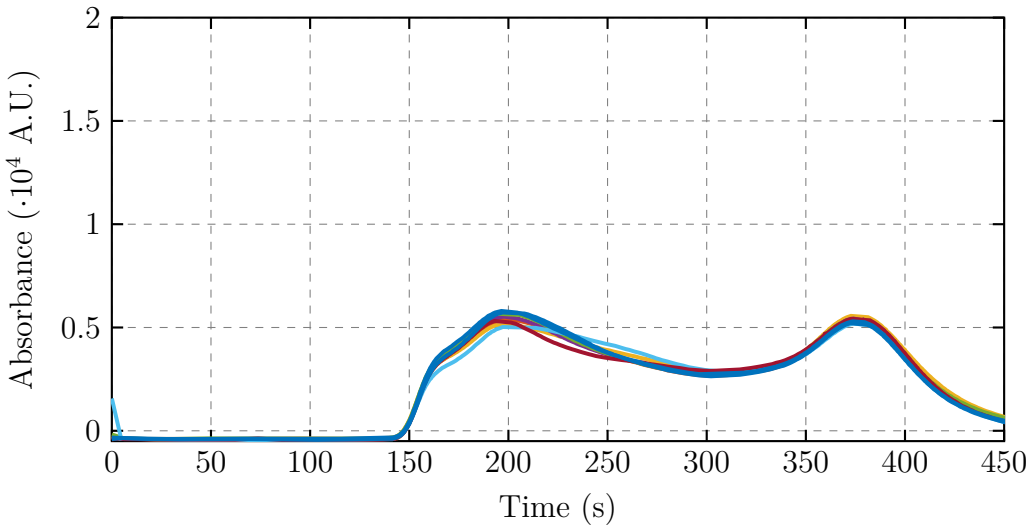

Fig. 6.19.: Elution chromatograms of a CHT bed packed using de-coupled vibration. 2 vibrators.

Even though the chromatograms show fewer peaks than the case with a single vibrator, it is still apparent that the vibrated columns do not posses an homogeneous microstructure and are still less efficient than the standard packed ones. Furthermore, a small macrostructural inhomogeneity in the bed could be observed at the end of the vibration time. The central region appeared to build a plateau forming a higher region than the surrounding ring region near the column wall.

De-coupled vibration - 300 $\frac{cm}{h}$ - 2 Vibrators - 2 bar - Vibration rotation: Another hypothesis for the inhomogeneous peak shape was that this was caused by the vibrators only contacting a limited portion of the total circumference of the column. The total vibration time was divided in two. After the first half, vibration was stopped and the holders were rotated 90 °around the column axis. Vibration was then applied for the remaining half total time.

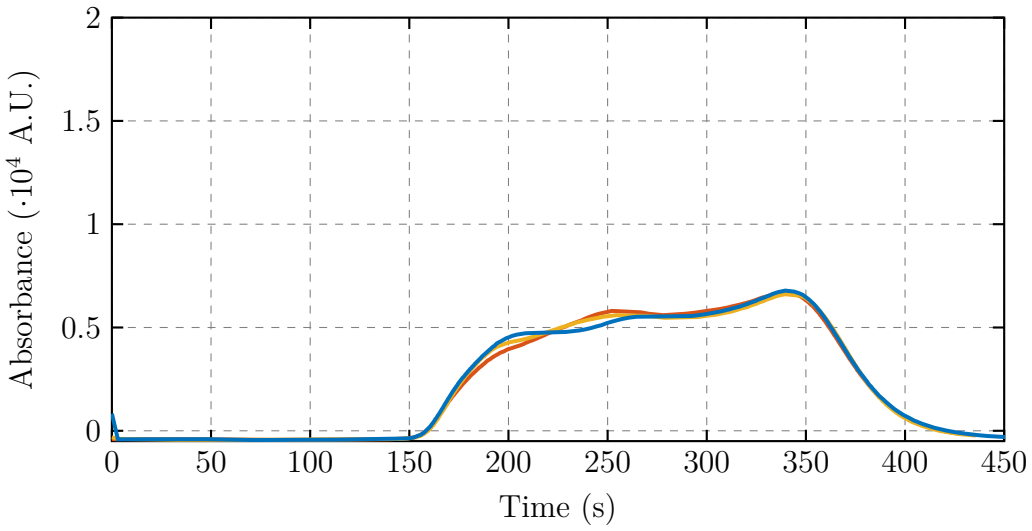

Fig. 6.20.: Elution chromatograms of a CHT bed packed using de-coupled vibration. 2 vibrators with partial rotation.

De-coupled vibration - 300 $\frac{cm}{h}$ - 2 Vibrators - 4 bar: Another hypothesis for the inhomogeneous peak was a lack of force of the vibrators. The air pressure into the vibrators was thus doubled to 4 bar.

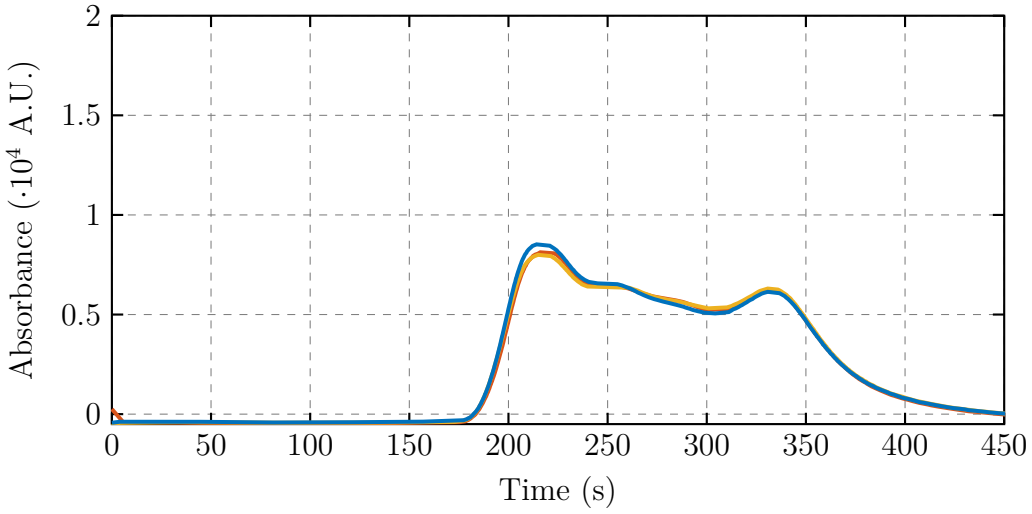

Fig. 6.21.: Elution chromatograms of a CHT bed packed using de-coupled vibration. 2 vibrators at 4 bar.

It was observed that the surface of the bed acquired a similar plateau (see Figure 6.22) as seen in the experiment at 2 bar but much more pronounced. This could be caused by granular convection carrying the particles toward the center or the attenuation of mechanical vibration as it enters the packing, with stronger waves and larger compaction

on the outside of the bed, while weaker vibrations generate smaller compaction in the center. As in the previous cases, vibration appeared to generate a more inhomogeneous microstructure as well.

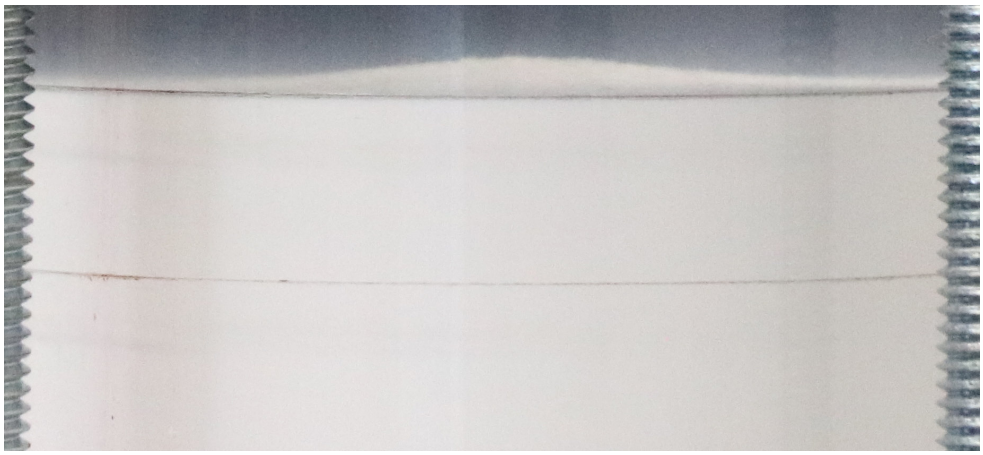

Fig. 6.22.: Top surface of the bed after lateral vibration with 2 K-8 vibrators at 4 bar.

Peak-evolution experiments

The change of peak shape hints towards an inhomogeneous change of the packed bed. It was not known if this heterogeneity took place from the start of the vibration, or if it started once the whole bed homogeneously compacted and the vibration was kept on. To answer this, the change of the peak was followed by carrying out a vibration-assisted packing during which the vibration was stopped every 10 minutes, and elution chromatograms were measured.

De-coupled vibration - 300 $\frac{cm}{h}$ - Lateral vibration: Packing and vibration parameters remain equal to the last section.

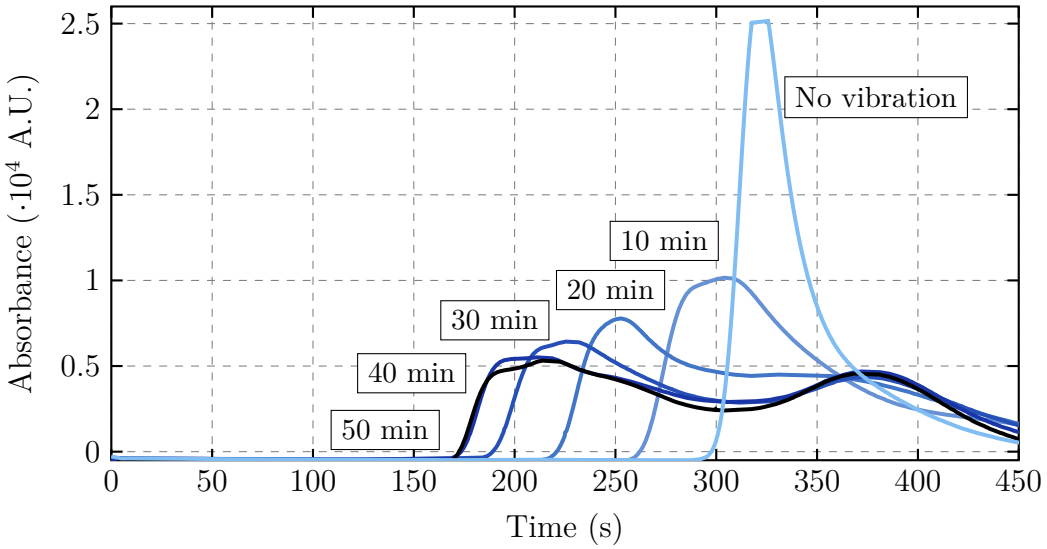

Fig. 6.23.: Elution chromatograms taken under vibration with two K-8 at intervals of 10 minutes. The clear blue curve shows the elution chromatogram of a bed with no vibration. The black curve shows the elution chromatogram after 50 minutes of vibration.

It appeared that all compaction achieved with lateral vibration is inhomogeneous and starts as such from the time vibration is turned on. An alternative approach was the use of vertical vibration directly applied to the bottom flow distributor of the column as shown in Section 4.3.2. Due to place limitations, it was only possible to attach a single K-8 rotational vibrator to the metal clamp. When turned on, the rotational vibrator caused granular convection with a region of the bed flowing towards the opposing side, generating a marked heterogeneous macroscopic structure. The use of rotational vibrators was thus stopped and instead, two FP-12-S linear vibrators were attached to the bottom flow distributor through the metal clamp as shown in Figure 4.7.

6.3.2. Vibration packing in a 50 mm column

To better reproduce the conditions in real preparative chromatographic processes [5], the $^{H}/_{D}$ was set to 0.5. As in the previous experiments, gravity sedimentation was avoided and the beds were first packed using flow after which vertical linear vibration was applied.

Polymethylacrylate packings

Following the flow packing method recommended by the manufacturer, the standard PMA beds were packed using 3 flow-packing steps at 800 $^{cm}/_{h}$ for 2 minutes each. Between each step the top fluid distributor is lowered down to a distance of 2 mm above the bed edge. As a last step, the distributor is driven 1 - 2 mm into the bed, exerting a mechanical compression. Vibration-assisted packing was based on the same packing template, with the vibration taking place after the first flow-packing step. Once vibration ended, all flow steps were carried out as usual. The vibrators were operated with pressurized air at 1.5 bar to compensante for the shorter bed, achieving a volumetric force of $\sim$ 1190 $^{N}/_{l}$. Pressures under 1.5 bar failed to consistently start the vibrators and also caused them to randomly stop working, these were thus not explored. Figure 6.24 exemplarily shows the compaction evolution of a PMA bed. The comparison between the initial flow-packed and final vibrated bed can be seen in Figure 7.6 in the last chapter.

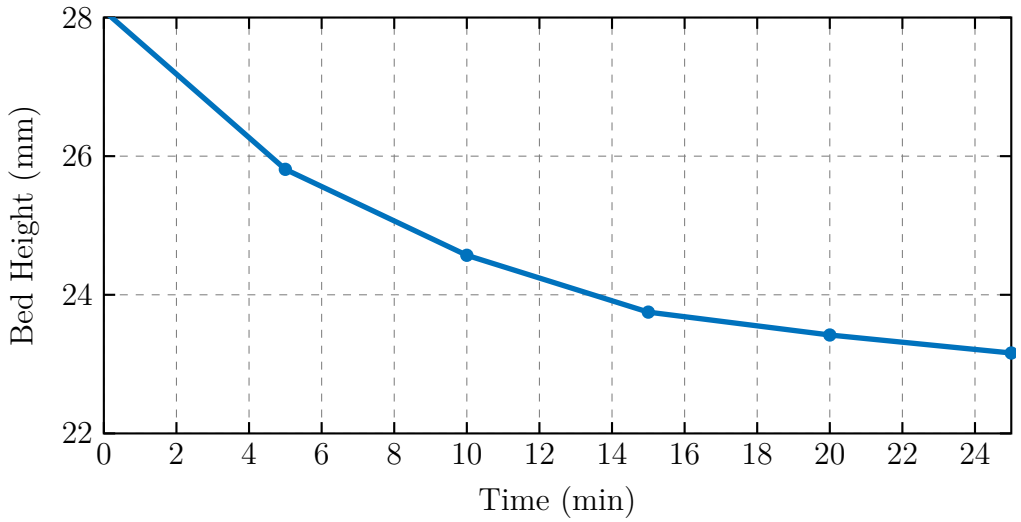

Fig. 6.24.: Exemplary height evolution of a PMA bed compacted through vibration. Additional bed compaction was 4.9 mm ($\lambda = 18\%$).

Flow-packed beds had an average height of 27.7 ± 0.5 mm (N=3), while vibrated beds reached 23.3 ± 0.2 mm (N=3). This corresponded to a relative compaction of $18 \pm 0.9\%$. The total compaction time was 25 minutes, after which no appreciable compaction was observed. Macroscopically, the bed showed an homogeneous compaction. As with the previous experiments, the homogeneity of the bed at the microstructural level was checked with pulse injection experiments and comparison of HETP.

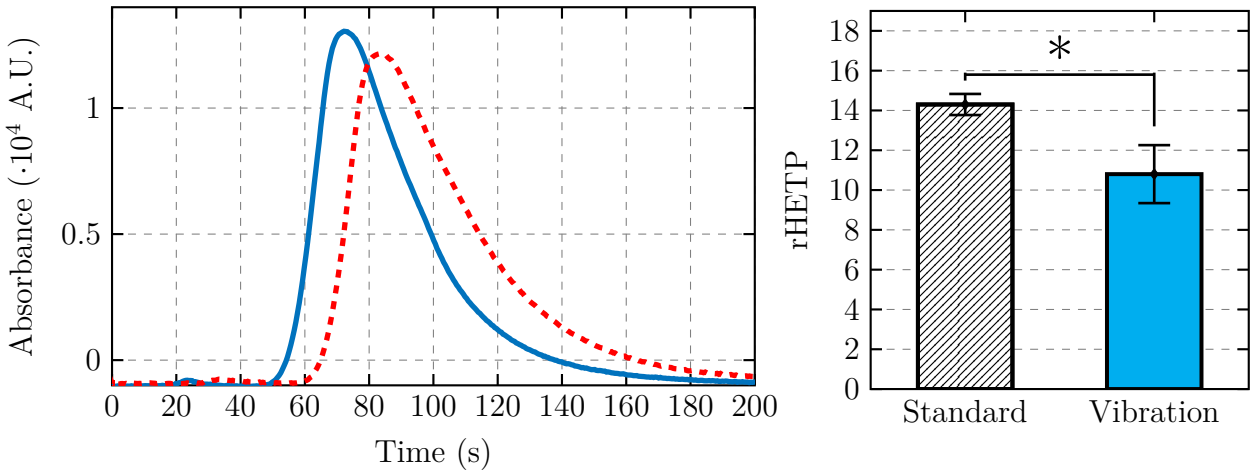

(a) Elution chromatograms of (red dashed line) standard-packed PMA bed, and (blue continuous line) vibration-packed bed.

(b) rHETP from standard and vibration-packed beds.

Fig. 6.25.: Improved bed efficiency through vibration-assisted packing of polymethylacrylate beds. Standard packing (N=3, $rHETP = 14.3 \pm 0.53$), and vibration-assisted packing (N=3, $rHETP = 10.8 \pm 1.46$), ($P < .05$).

Figure 6.25 shows two chromatograms. One corresponds to a PMA bed packed following conventional flow-packing methods (dashed line), while the second one corresponds to the vibration-assisted packing method. It can be seen that the vibrated bed has a comparatively larger peak maximum and narrower peak width. The corresponding rHETP for both experiment series can bee seen in Figure 6.25b. Standard-packed rHETP (N=3) reached 14.3 ± 0.5 while vibrated beds (N=3) had rHETP of 10.8 ± 1.4. There was a statistically significant difference between both packing methods at the 95 % confidence level (P=0.0395).

Ceramic hydroxyapatite

The standard packing method for CHT particles consists of a single flow packing step at 300 $^{cm}/_{h}$ held for two minutes, after which the top flow distributor is lowered until there is a space of 1 - 2 mm between it and the bed edge. This gap is set due to the incompressible nature of CHT, to prevent any mechanical compression, avoiding particle damage and formation of fines.

For the vibration-assisted packing, vibration is turned on after the bed has been flow-packed. Once compaction has fully taken place, packing continues as usual and the top distributor is lowered until there is a gap of 1 - 2 mm between it and the bed.

Flow-packed beds had an average height of 28.3 ± 0.03 mm (N=3), while vibrated beds reached 24.3 ± 0.05 mm (N=2). This corresponded to a relative compaction of

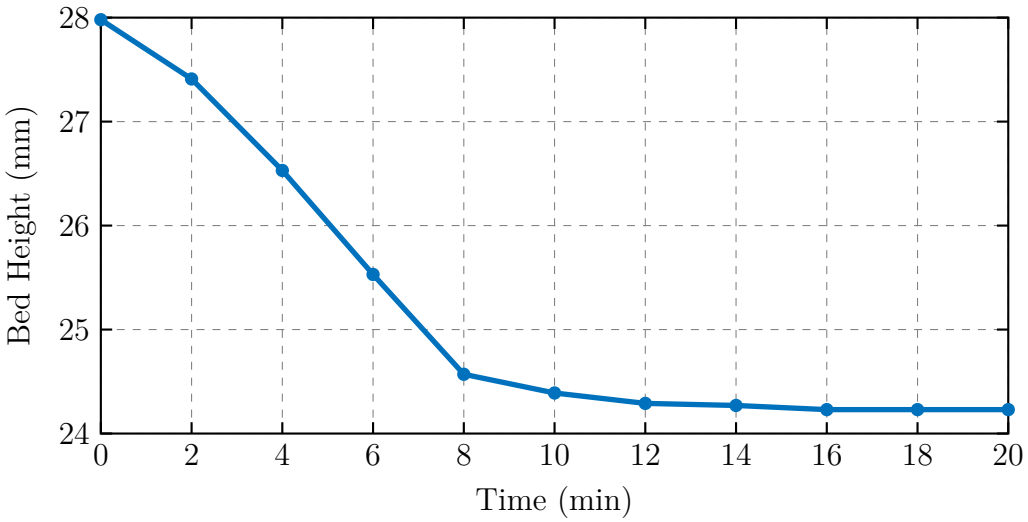

Fig. 6.26.: Exemplary height evolution of a CHT bed compacted through vibration. Additional bed compaction was 3.7 mm ($\lambda = 13\%$).

$13 \pm 0.2\%$. Figure 6.26 exemplarily shows the compaction behavior of a CHT packing under vibration. The bed compacted rapidly in the first 8 minutes of vibration, after which it acquired a significant lower speed, approaching the final height asymptotically. The height difference of the same bed before and after vibration can be seen in Figure 7.6. As in the previous case, the bed appeared to be macroscopically homogeneous.

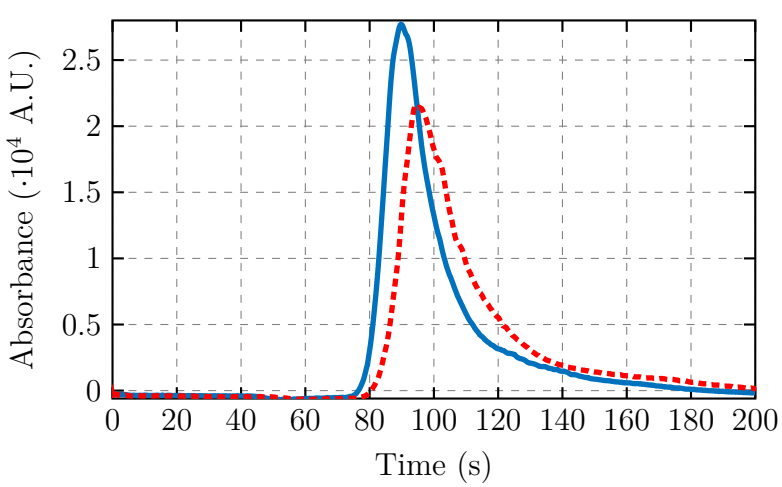

(a) Elution chromatograms of (red dashed line) standard-packed CHT bed, and (blue continuous line) vibration-packed bed.

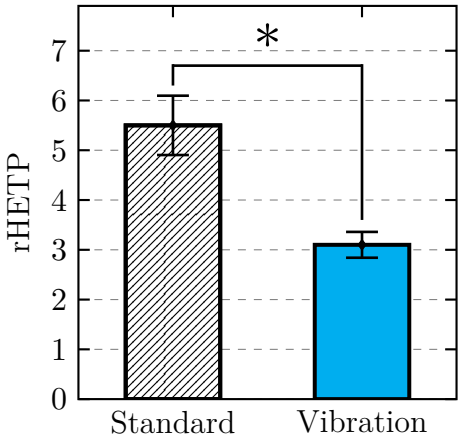

(b) rHETP from standard and vibration-packed beds.

Fig. 6.27.: Improved bed efficiency through vibration-assisted packing of ceramic hydroxyapatite beds. Standard packing (N=3, $rHETP = 5.5 \pm 0.6$), and vibration-assisted packing (N=3, $rHETP = 3.1 \pm 0.26$), ($P < .05$).

Figure 6.27 shows a chromatogram of a standard-packed and vibration-assisted bed. As for PMA packings, CHT vibrated beds exhibit a larger maximum peak and a narrower peak width in comparison to standard beds. Associated rHETP can be seen in Figure 6.27, in which standard beds reach rHETP of 5.5 ± 0.6 and vibrated beds rHETP of 3.1 ± 0.26. There a statistically difference between both values at the 95 % significance level (P=0.01).

The comparatively smaller improvement of rHETP for polymethacrylate columns in comparison to CHT can be attributed to the additional mechanical compression step after flow packing of the compressible particles. During this step, the upper flow distributor was pressed up to 2 mm into the PMA bed, corresponding to a compaction factor of $\lambda = 7$ %, which further reduced the void spaces of the column. The packing structure was thus already denser in comparison to the solely flow-packed CHT structure. As the porosity of standard-packed polymethacrylate column was smaller, there was comparatively less room for improvement through vibration.

6.3.3. In-situ correction of packing defects in the 50 mm column

It has been established that vibration can be successfully implemented into packing methods, and that these deliver denser and microscopically homogeneous packings. The possibility of correcting packing defects on already packed beds was additionally studied. Figure 6.28a shows a PMA bed with flow channels caused by the presence of air bubbles during flow packing. The packing process was carried out following the standard method and the final state including mechanical compression can be seen in Figure 6.28b.

No macroscopic heterogeneities could be seen, however through pulse injections it was apparent that the channels were still present. Figure 6.29a shows (dashed red line) the chromatogram of the bed with channeling defects. A peak fronting shoulder can be observed and most likely corresponds to the channeled region having a lower porosity in comparison to the bulk of the bed. Thus, a portion of the mobile phase exits the packing through this less dense region and reaches the detector faster.

Using the same vibration parameters for the vibration-assisted packing, the bed with defects was vibrated in place for 25 minutes. No other modifications or work were carried out on the column. After this, pulse injection was repeated and the resulting chromatogram can be seen in Figure 6.29a as the continuous blue line. It is apparent

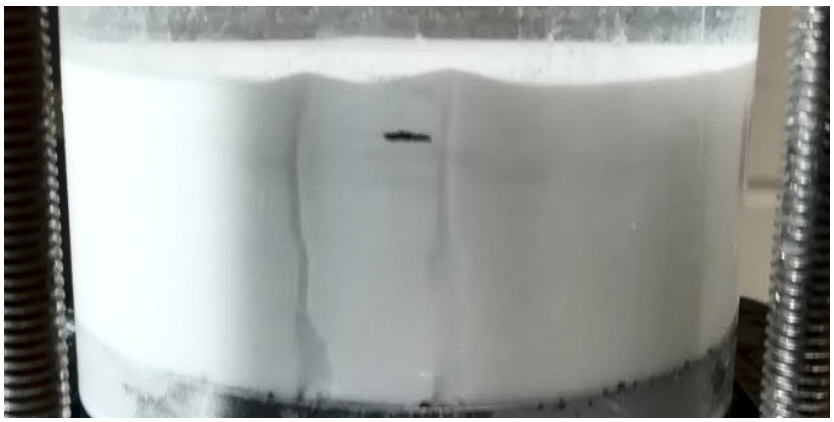

(a) Channeling defects due to air bubbles during packing.

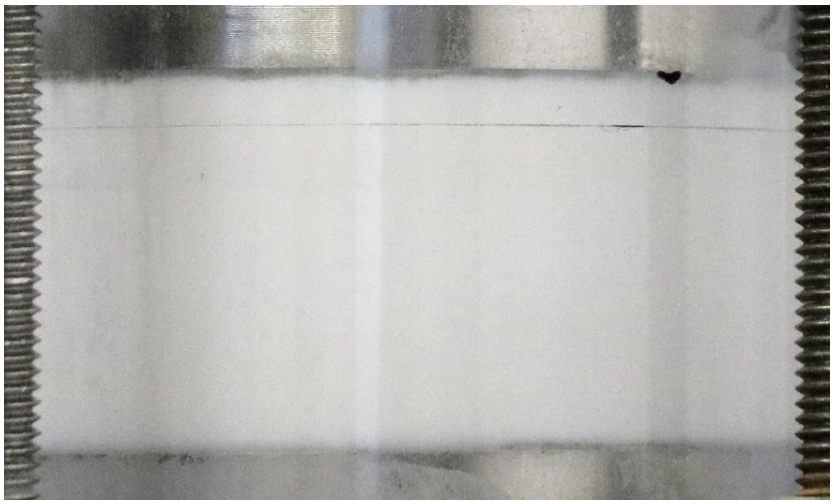

(b) Unobservable bed defects after a mechanical compression of 2 mm. Macroscopically, the bed appears homogeneous.

Fig. 6.28.: Correction of bed defects through in-situ vibration.

that the shoulder has disappeared, and the peak maximum has increased.

The associated rHETP can be seen in Figure 6.29b. The rHETP of the bed has been improved considerably from 25.6 down to 12.5, thus restoring the bed to an efficiency even slightly better than the standard rHETP of 14.3 ± 0.53. The fact that the rHETP did not reach the values of the vibration-assisted packed beds can be in part explained by the mechanical compression of the bed. This restricts the motion range of the particles and hinders the exploration of the phase space.

6.3.4. Vibration packing in a 200 mm column

Once the feasibility of of vibration-assisted packing was established, the possibility of employing analogous methods for process-scale columns was explored. To do this,

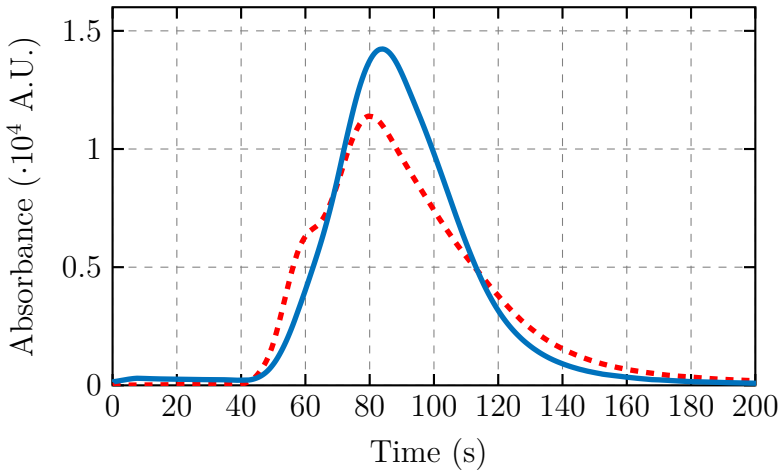

(a) Elution chromatograms of (left) a bed with channeling defects, and (right) after defect correction with vibration.

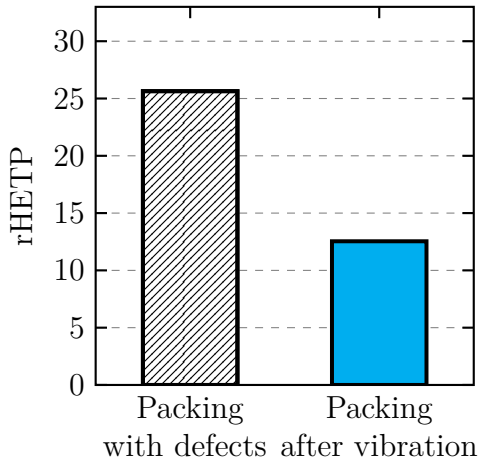

(b) rHETP of **(left)** bed with defects and (right) after vibration.

Fig. 6.29.: Correction of bed defects through in-situ vibration on a polymethylacrylate bed with flow channels. With defects $rHETP = 25.6$, and after vibration $rHETP = 12.5$.

four FP-35-S vibrators were attached to the column (see Section 4.4.2). Due to space constraints it was not possible to attach the linear vibrators directly underneath the bottom flow distributor. Instead, each vibrator was attached to a leg of the column. The starting point for all packing procedures was a suspension with an approximately 30 % particle concentration unless stated otherwise.

Ceramic hydroxyapatite

As for the 50 mm column, the standard packing method for CHT particles consisted of a single flow-packing step at 300 $^{cm}/_{h}$, after which pulse experiments were carried out. Several vibration-packing experiments were carried out. The first one consisted of the vibration of the flow-packed bed. As no satisfactory result was obtained, a series of vibration variations were undertaken. An overview of the experiments and their respective results can be seen in Table 6.1.

Experiment	H/D	ΔH (%)	$rHETP$	As
Standard packing	~ 0.5	-	7.08	2.1
Standard packing. Vibration (5 bar) for 20 minutes afterwards	~ 0.5	3.9	21	2.8
Standard packing. Vibration (6 bar) for 20 minutes afterwards	~ 0.5	5.9	16.86	3.02
Standard packing. Alternating vibration (6 bar) and flow ($300\frac{cm}{h}$) every 2 minutes, 5 times	~ 0.5	3.9	8.83	2.36
Standard packing and simultaneous vibration (6 bar)	~ 0.5	3.9	21.95	1.45
Standard packing and simultaneous vibration (6 bar). Alternating vibration (6 bar) and flow ($300\frac{cm}{h}$) every 2 minutes, 5 times	~ 0.5	6.9	11.99	1.82

Table 6.1.: Results overview of standard- and vibration-packing protocols for CHT beds in the 200 mm column.

It is evident that, as in the 50 mm columns, there is room for additional compaction in the 200 mm columns packed following standard methods. All experiments showed height compressions between 4 and 7 %. However, the microstructure seems to become heterogeneous, resulting in much higher rHETP and asymmetries.

Polymethylacrylate packing

PMA beds were analogously packed using the same 200 mm column configuration. The standard procedure consists of three flow packing steps (FPI, FPII and FPIII), as was done for the 50 mm column. An overview of the experiments and their respective results can be seen in Table 6.2.

Experiment	H/D	ΔH (%)	$rHETP$	As
Standard packing	~ 0.5	-	2.93	1.44
Sedimentation. Vibration (6 bar) for 5 minutes	~ 0.5	3.4	4.48	1.27
Vibration (6 bar) for 20 minutes between FPI and FPII	~ 0.5	5.7	5.52	1.48
Vibration (6 bar) for 20 minutes after FPIII	~ 0.5	3.4	10.83	1.76
Vibration (6 bar) for 5 minutes after between FPI and FPII, and FPII and FPIII	~ 0.5	3.4	6.06	1.89
Rotating one vibrator (6 bar, 5 min) in all positions between FPI and FPIII	~ 0.5	5.7	3.5	1.4
Rotating one vibrator (6 bar, 20 min) in all positions between FPI and FPII	~ 0.5	5.7	4.97	1.01
Rotating one vibrator (6 bar, 20 min) with simultaneous flow (800 $\frac{cm}{h}$)in all positions between FPI and FPII	~ 0.5	3.4	36.97	1.45
Rotating two vibrators (6 bar, 5 min) in all positions between FPI and FPII	~ 0.5	6.8	5.2	1.2
Rotating two vibrators (6 bar, 5 min) in all positions between FPI and FPII, and FPII and FPIII	~ 0.5	5.7	6.56	1.27

Table 6.2.: Results overview of standard- and vibration-packing protocols for PMA beds in the 200 mm column.

Similarly as with CHT particles, a macroscopic height compaction between 3.4 and 6.8 % could be observed when vibration was applied, indicating that thus both particle types have considerable room for improvement regarding conventional packing methods. However, and similarly to the CHT results, it appears that the current configuration delivers an inhomogeneous compaction of the bed. No improved rHETP or asymmetries could be observed. Furthermore, such inhomogeneity could be macroscopically observed. Figure 6.30 shows a ring-like section of the packed bed which is more compact than the central region. This denser section limits with the column wall.

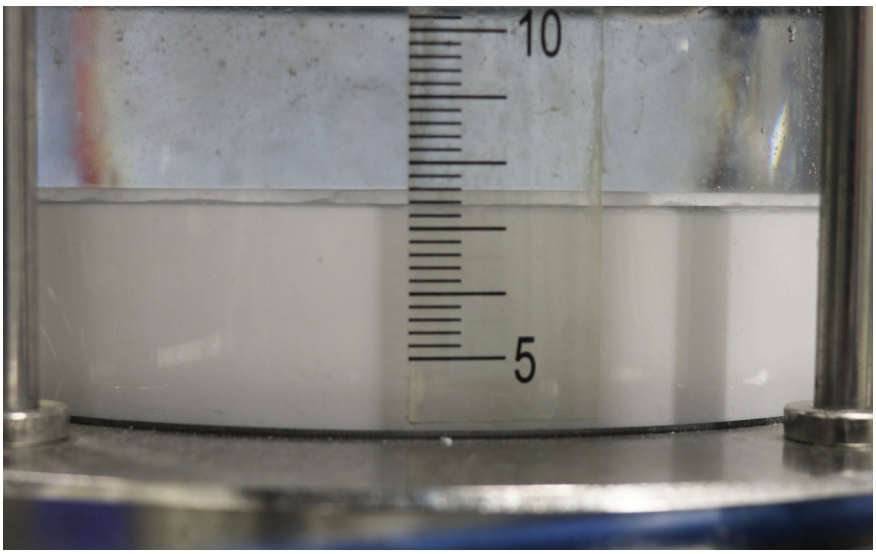

Fig. 6.30.: Height difference between the denser outer ring and central region of vibrated column. Distance between each marking is about 2 mm. Picture was taken during a flow packing step (800 $^{ch}/_{h}$)

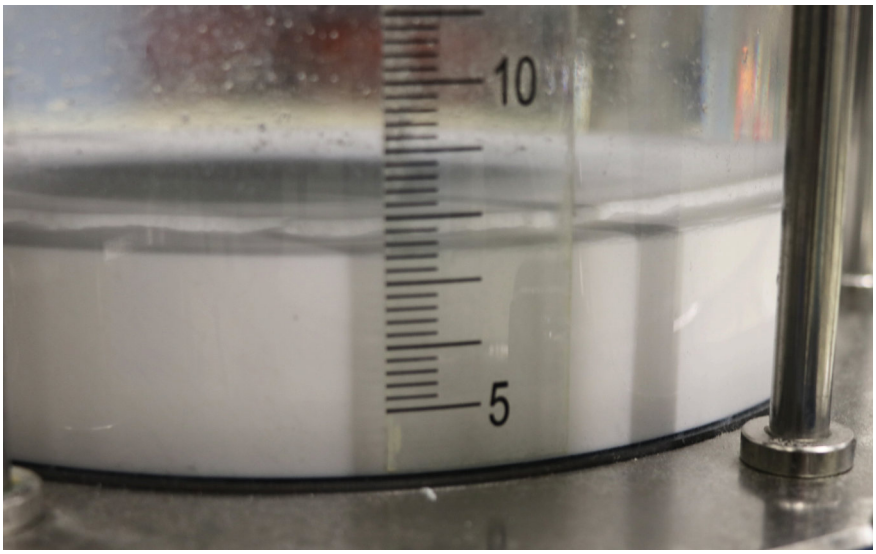

Fig. 6.31.: Width of the denser outer ring of approximately 2 cm. Picture was taken during a flow packing step (800 $^{cm}/_{h}$)

A possible explanation for the observed worsened column efficiencies and inhomogeneous compaction of the column is the entry direction of the vibrations. As seen in Section 6.3.1, it is possible that as vibrations enter the packing laterally, these do not reach the inner region of the packing. This results in the formation of a central region less dense than the outer ring, and unsatisfactory efficiencies. The location of the vibrators could be causing a partial lateral entry of vibration into the column.

6.3.5. Vibration packing in a 400 mm column

The scale-up of vibration packing was also explored in the 400 mm column. As shown in Section 4.4.2, four FP-35-S vibrators were attached to the feet of the column. CHT particles were packed following the standard packing procedure and combinations of vibration packing seen in Table 6.3. H/D ratios of 0.25 and 0.5 were explored. As with the previous 200 mm column, CHT packing underwent compaction through vibration. At H/D = 0.25 the maximal compaction was 3 %, while at H/D = 0.5 it was 1.5 % . However, additional compaction did not translate into an improve of either rHETP or asymmetries, indicating that the particle rearrangement did not generate an homogeneous microstructure.

Experiment	$\frac{H}{D}$	ΔH (%)	$rHETP$	As
Standard packing	~ 0.5	-	5.1	1.5
Standard packing. Vibration (5 bar) for 20 minutes afterwards	~ 0.5	1.51	6.0	1.8
Standard packing with simultaneous vibration (5 bar)	~ 0.5	0	14.3	2.3
Standard packing. Alternating vibration (5 bar) and flow ($300\frac{cm}{h}$) every 2 minutes, 5 times	~ 0.5	1.2	5.8	1.5
Standard packing	~ 0.25	-	6.4	1.6
Standard packing. Vibration (5 bar) for 20 minutes afterwards	~ 0.25	2.03	7.2	2.4
Standard packing. Alternating vibration (5 bar) and flow ($300\frac{cm}{h}$) every 2 minutes, 5 times	~ 0.25	3	7.9	2.1

Table 6.3.: Results overview of standard- and vibration-packing protocols for CHT beds in the 400 mm column.

A possible explanation for this is the entry direction of the vibration into the column. As can be seen in Figure 6.32, each vibrator is bolted onto a leg of the column, which in turn is attached to the underside of the column. It can be expected that vibrations do not enter the column in a purely vertical direction, and that any horizontal portion

of the mechanical waves causes an inhomogeneous compaction as previously seen in the 50 mm or 200 mm column.

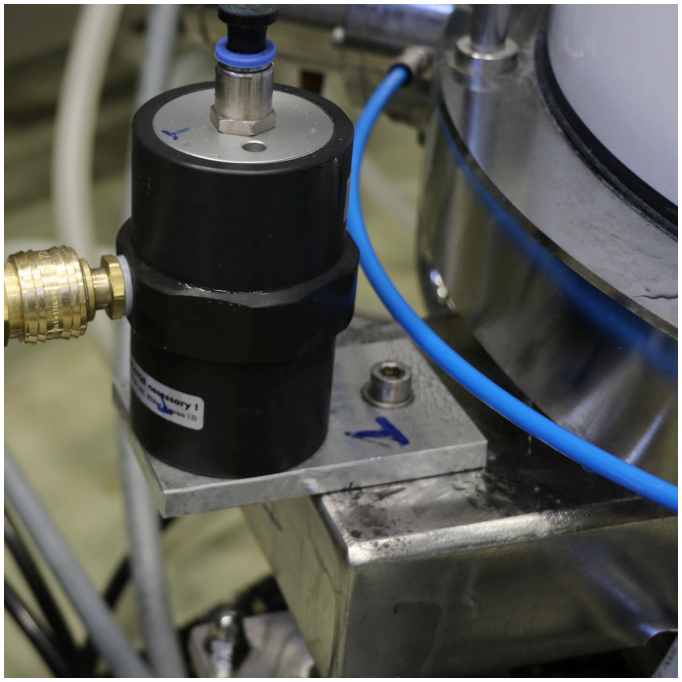

Fig. 6.32.: Detail of attachment of FP-35-S pneumatic vibrator to the 400 mm column. Each of the 4 vibrators was attached in the same manner.

Furthermore, it was observed that the use of vibration caused fines which were visible in the process line downstream from the column. The presence of fines was also seen under the microscope from samples taken after vibration experiments. The amount of fines present depended on the intensity of the vibrators and vibration time. Figure 6.33 shows the effluent of the column after a vibration experiment of 20 minutes in comparison to the normal buffer solution

Overall, the available possibilities for the attachment of the vibrators limited the vibration options. An adequate positioning of the vibrators on the underside of the column, generating a vertical vibration of the bed could deliver an homogeneous particle rearrangement as seen in the 50 mm column. Moreover, it is conceivable that a portion of the vibration energy was lost due to the vibrators being attached to the legs. These are not only connected to the column, but also in direct contact with the floor, which could have absorbed a fraction of the energy. Thus, a setup that bypasses the legs could mean a more efficient compaction.

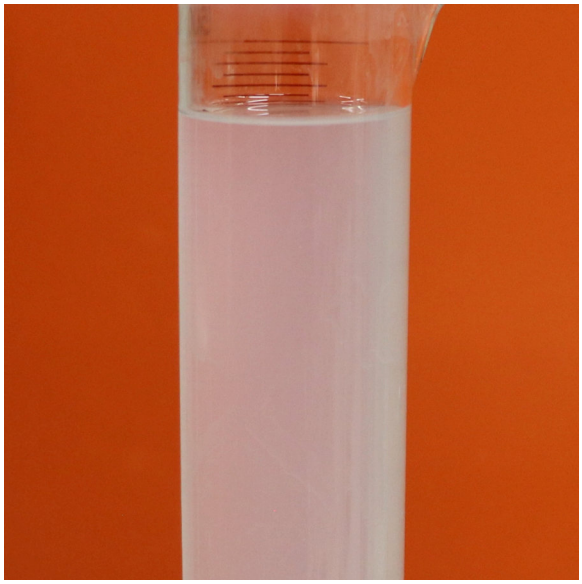

(a) Outlet solution cloudy with particle fines.

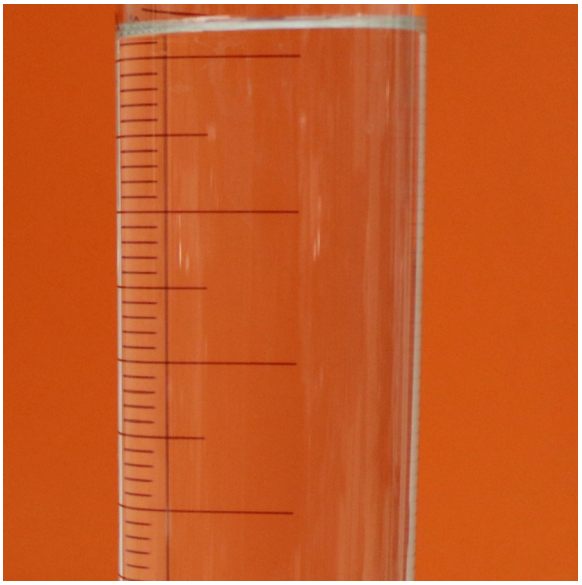

(b) Normal outlet solution.

Fig. 6.33.: Evidence of fine formation due to mechanical stress on the particles.

The generation of fines most likely took place at the nearest point between the vibrator and the packing, near the column wall. At this point vibrations have not been attenuated as much as in the center of the column. The reasoning for the use of high-intensity vibration was to overcome such attenuation by delivering enough vibrational energy as to reach the center of the packing. Vibrators attached directly on the underside of the column would negate such necessity, thus potentially avoiding fine formation at vibrational "hot-spots".

Overall, it can be concluded that current packing methods do not deliver the most dense bed structure possible either for the 50 mm, 200 mm and 400 mm column. This applies both for compressible and incompressible particles. The amount of maximal compression was seen to depend on the column diameter. It is well known that the wall effect is strongest at small column diameters. It causes the formation of stabilizing force networks along the packing which contain void spaces increasing porosity. As the wall effect becomes weaker at larger diameters, such networks are no longer able to support as much of the bed. This results in the collapse of granular structures, filling void spaces and decreasing porosity. This means that wider columns have less compaction potential than narrower ones as can be seen in Figure 6.34.

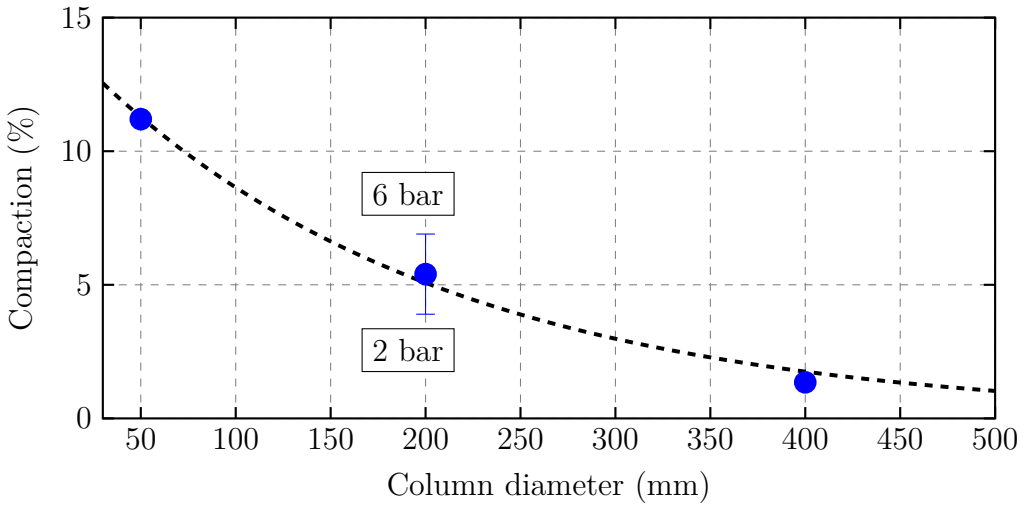

Fig. 6.34.: Maximal height compaction through vibration of ceramic hydroxyapatite beds at $^{H}/_{D} \pm 0.5$ as a function of column diameter. Wider columns exhibit a less pronounced wall effect, and have a smaller possible maximal compaction.

7. Conclusions

This work focused on two issues with current packed bed chromatography technology in the biomanufacturing sector:

- There is a lack of measurement techniques for detailed 3-dimensional reconstructions of biochromatography packings at the microscopic scale. This prevents the analysis of real bed structures and their study in connection with packing methods or evolution during operation. To overcome this, a reconstruction process based on micro-computed tomography (micro-CT) was developed and demonstrated on three commonly used chromatographic media

- Current column packing technology achieves chromatographic beds which are not in their most densely packed state, often resulting in a slow continuous settling under operation. As the packing structure changes, the chromatographic separation may be negatively impacted by headspace or channel formation. Moreover, performance drift is unwanted in biomanufacturing, which is heavily focused on robustness, stability and reproducibility of unit operations. The limitations of packing protocols stem from the lack of knowledge on the packed structure achieved by different packing protocols, and the limitations regarding the tools used during packing. Primarily two tools are available, either dragging the particle suspension in the column downwards using flow or mechanically compressing an already formed packing with the upper column plunger. The use of mechanical vibration as an additional packing tool was developed in this work and applied on two commonly used chromatographic media and at three different column diameters

7.1. 3-dimensional reconstruction of chromatographic columns with micro-computed tomography

Robust and able to achieve high resolutions in the range of 2 µm per pixel, micro-CT relies on the X-ray absorption contrast between different materials to distinguish them. This represents a challenge for the measurement of biochromatography packings due to the properties of the particles forming them. These particles are commonly based on organic polymers with weak X-ray absorption and have a high internal porosity, resulting in an overall X-ray absorption near that of the mobile phase in the void spaces between them. Figure 7.1a shows a tomographic slice of a packing made of polymethylacrylate (PMA) particles without any modification. The similarity of X-ray absorption properties between particles and void spaces prevents their differentiation and no structure can be observed.

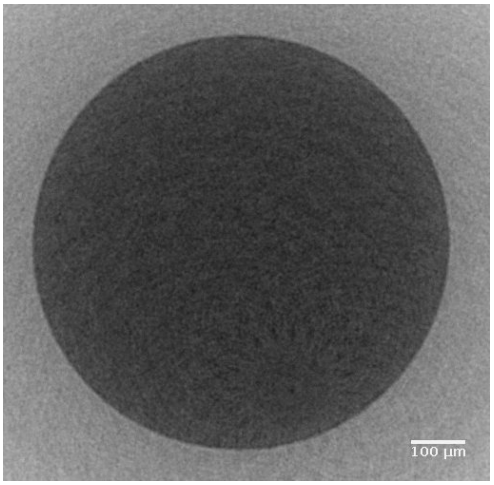

(a) Tomographic slice of an unmodified PMA packing in a 760 µm column. Particles and void spaces are filled with 10 mM NaOH.

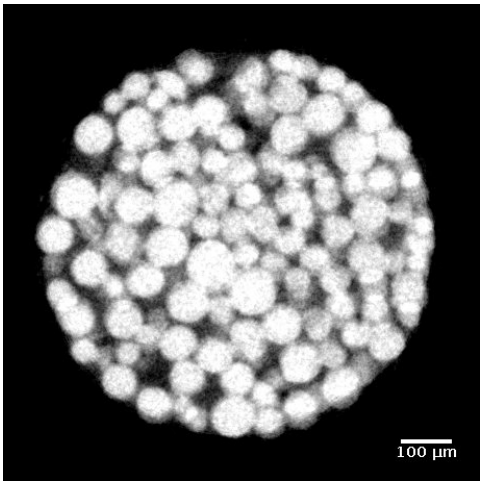

(b) Tomographic slice of a PMA packing after PBM. Particles contain a 7.2 M potassium iodide aqueous solution and void spaces are filled with n-decane.

Fig. 7.1.: The developed method to increase X-ray contrast of chromatographic media enables their measurement and posterior 3-dimensional reconstruction. Copy of Fig. 5.7 and Fig. 5.8b.

To overcome this, a method based on the pore-blocking method (PBM) to increment the particle-void X-ray absorption contrast was successfully developed. The PBM relies on the non-miscibility between a hydrophobic and an aqueous phase. By sequential pumping of the phases through a packing at adequate flow rates, times and volumes,

it is possible to obtain a column in which the particles contained the aqueous solution containing a radio-contrast agent, while the voids contained a hydrophobic phase. This process could be applied in-situ on already packed columns and required no previous particle modification. The individual steps on a packed column are schematically shown in Figure 7.2, with potassium iodide as the radio-contrast agent and n-decane as the hydrophobic media.

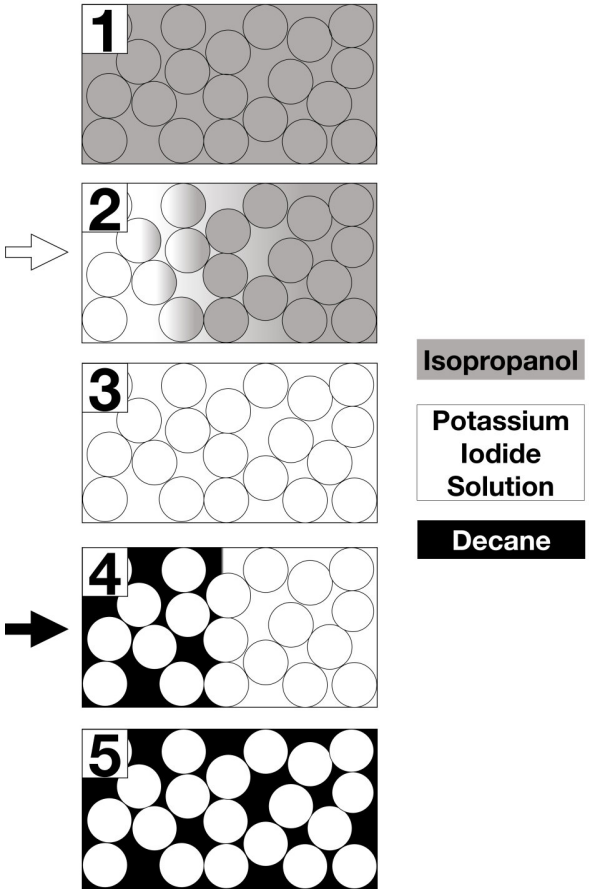

Fig. 7.2.: Schematic representation of the modified pore blocking method. 1) The packed column is filled with isopropanol. 2) An aqueous solution of potassium iodide is pumped into the column. 3) Due to their miscibility, isopropanol mixes with and is eventually displaced by the aqueous solution of potassium iodide which then fills all spaces. 4) N-decane is pumped into the column, displacing the immiscible aqueous solution from the extraparticle void space. 5) Particles remain filled with the aqueous potassium iodide solution while the extraparticle space contains n-decane. Copy of Fig. 5.2.

This method was applied for the measurement of packings of three particle types; one polmethylacrylate and two different agarose media. Once pore-blocked, the packings were measured with micro-CT to generate 3-dimensional microscopic reconstructions. Figure 7.1b shows a tomographic slice from a packing of polymethylacrylate particles

after undergoing PBM. Since the radio-contrast agent is filling the pores of the particles, it is now possible to differentiate these from the void spaces containing n-decane, a weak X-ray absorber.

The binarised tomographic data enables the reconstruction of the 3-dimensional structures, as can be seen in Figure 7.3 for a polymethylacrylate and an agarose packing. Furthermore, it enables the calculation of geometric properties of real already packed chromatography columns.

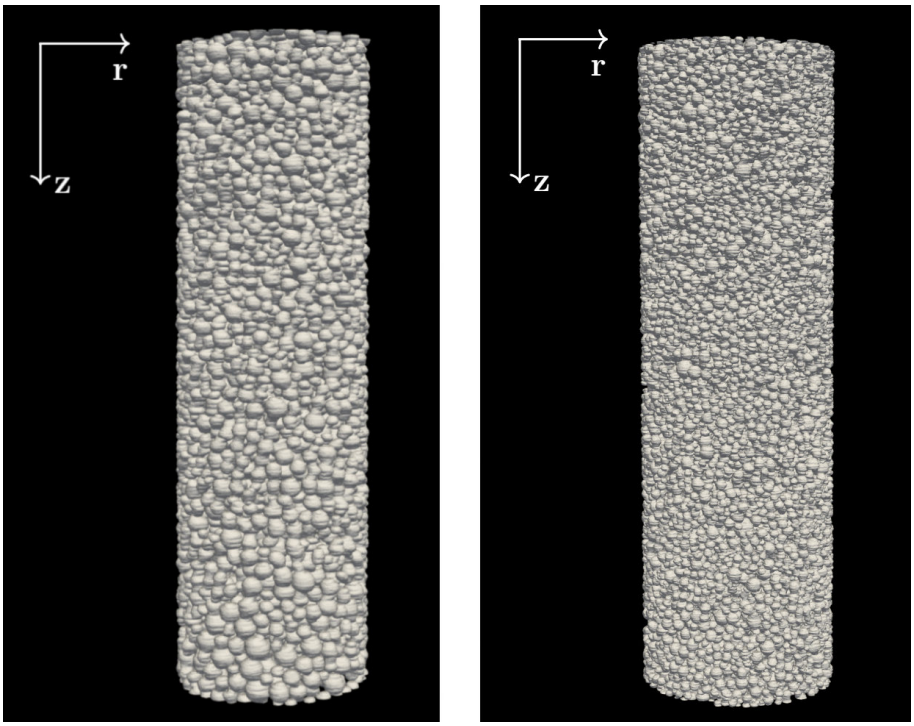

Fig. 7.3.: 3-dimensional reconstruction of (left) polymethylacrylate and (right) agarose packings. Height and diameter are respectively 2.5 mm and 760 µm for both packings. Copy of Fig.5.10.

The radial porosity profile corresponding to the PMA packing can be seen in Figure 7.4 and agrees well with the expected porosity profile of sphere packings in cylinders. The porosity minimum is located approximately at a distance of one mean radius ($\sim$ 30 µm) from the column wall and shows the highly organized first layer in contact with the wall. The packing becomes more locally disorganized near its center, approaching the overall mean porosity. Additional geometric properties such as axial porosity profile or presence of void spaces could also be calculated based on the tomographic data.

In summary, a method for the 3-dimensional reconstruction of biochromatography columns based on micro-CT and particle pore-blocking was successfully developed in

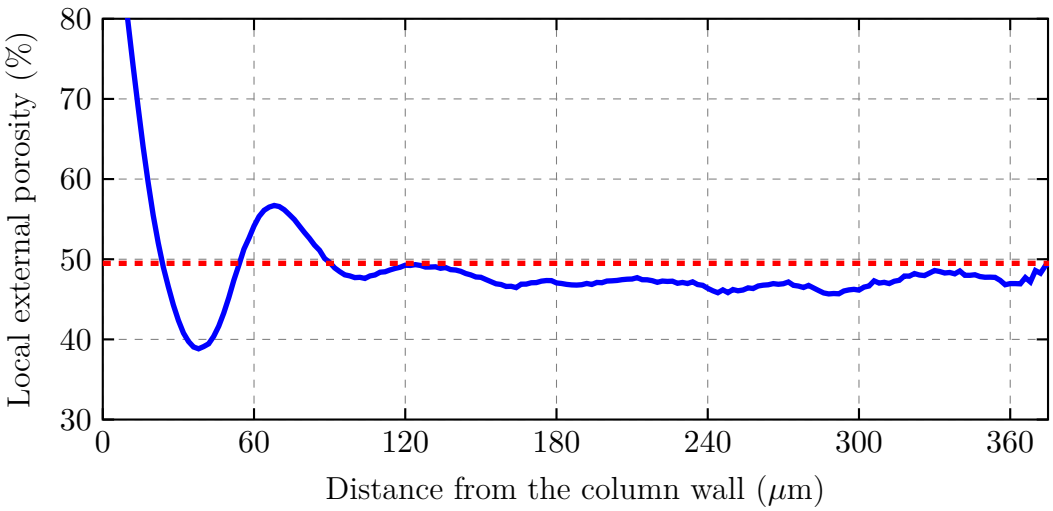

Fig. 7.4.: Radial porosity profile of the PMA packing. Blue line represents the smoothed profile ($r = 0$ corresponds to the column wall), while the dashed line indicates the overall packing porosity of 49.5 %. Copy of Fig. 5.12.

this work. To the author's knowledge, these are the first ever 3-dimensional reconstructions of agarose and polymethylacrylate chromatographic packings reported in the literature. The calculation of structure properties based on data with resolution at the individual particle level also represents a novel advancement for biochromatography packings.

7.2. Packing of biochromatography columns using mechanical vibration

The absence of understanding regarding the granular process of packing chromatography columns often leads to empirical packing protocols with poor reproducibility and inefficient columns. Such variability negatively affects not only the individual chromatographic step, but also the overall robustness of the downstream process.

Although ubiquitous in other industrial areas handling granular matter, the use of vibration has been sparsely implemented for the packing of biochromatography columns, with a limited number of articles and patents published for this application. Among uses such as material transport and unjamming of granular materials, mechanical vibration is often employed for compaction through energy delivery to a granular system so that it can explore the phase space and reach a denser configuration.

Two approaches for the inclusion of mechanical vibration in packing protocols were

explored; the use of ultrasonic transducers and pneumatic vibrators. Although the former could achieve enough acoustic potential to generate a flow inside the column and keep the particles in suspension, it could not deliver enough energy for the packing to further compress once settled. On the other hand, the use of the latter enabled an additional compaction of packings made from two chromatographic particles; a compressible polymethylacrlate and a rigid ceramic hydroxyapatite media (CHT).

7.2.1. Ultrasonic vibration

An ultrasonic field inside a chromatographic column creates a pressure gradient and fluid convection due to acoustic streaming. It was found that if the field is generated while the particle suspension in the column settles, the mixing effect will keep the media longer in suspension in comparison to gravity settling. A comparison of the suspension height for both cases can be seen in Figure 7.5. While during normal sedimentation the suspension beings consolidating as soon as the active flow stops, the particles under ultrasound irradiation remain longer in suspension, giving more time for the preparation and packing of the column, and delivering slightly denser beds.

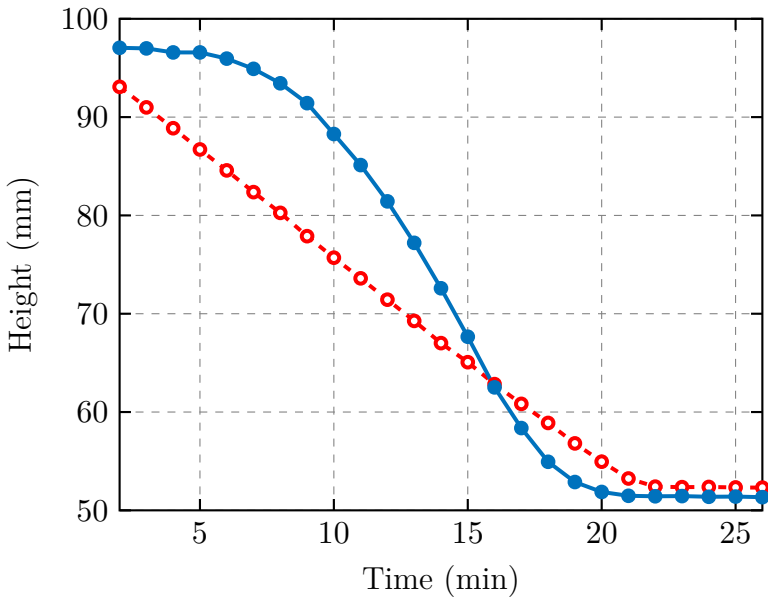

Fig. 7.5.: Settling curve of a polymethylacrylate slurry with (solid blue line) and without (dashed red line) ultrasound in a 50 mm column. The ratio of acoustic power to column volume was $\sim$ 76 $^{\text{Watt}}/_{\text{l}}$. Copy of Fig. 6.1a.

Once the packing had consolidated, it was observed that ultrasonic waves were not strong enough to overcome the frictional forces of the structure and cause additional compaction. This was attributed to the low power input of the ultrasonic transducer and the high acoustic reflection at the steel-water interface.

7.2.2. Pneumatic vibration

Using a 50 mm diameter column, pneumatic vibrators of two types (linear and rotational) were used in packing methods in combination with flow and mechanical packing. Additionally, the input direction of vibration, horizontal and vertical, was also studied.

In general, considerable additional compaction could be achieved employing mechanical vibration generated with pneumatic vibrators in almost all configurations, showing a stark contrast to ultrasonic vibration. The exception was simultaneous vibration during flow packing. It was observed that no compaction took place if flow was applied to the column as it was being vibrated, which indicated that the viscous drag of the mobile phase acted as a reinforcement on the force-chains supporting the packing.

Vibration de-coupled from flow caused additional bed compaction of rigid CHT and compressible PMA packings in all cases. Figure 7.6 shows the initial and final height of chromatographic beds of both media before and after linear vertical vibration. PMA flow-packed beds had an average height of 27.7 $\pm$ 0.5 mm, while vibrated beds were compacted to 23.3 $\pm$ 0.2 mm. CHT flow-packed beds had an average height of 28.3 $\pm$ 0.03 mm, while vibrated beds reached 24.3 $\pm$ 0.05 mm.

Rotational or lateral vibration also caused a macroscopic compaction of the packing, this was however concluded not to be homogeneous. This was observed as a considerable deterioration of efficiency, and the formation of a visible central plateau in the packing.

Mechanical vibration was accompanied with improvements in column efficiency when compaction using linear vertical vibration was carried out. Figures 7.7a and 7.7b show the rHETP reduction of 44 % for PMA (14.3 $\pm$ 0.53 to 10.8 $\pm$ 1.46) and 25 % for CHT (5.5 $\pm$ 0.6 to 3.1 $\pm$ 0.26) achieved through the compaction seen in the corresponding Figures 7.6a and 7.6b.

Furthermore, the use of in-situ vibrations for the correction of packing defects on already-packed beds was established. During a packing process, unwanted channels formed on the side of a polymethylacrylate packing due to the presence of air bubbles in the column. As consequence the column showed a diminished quality reflected in a rHETP of 25, considerably higher than the standard 14.3 $\pm$ 0.5. Linear vertical vibration was applied in-situ to the packing without other modifications and the rHETP

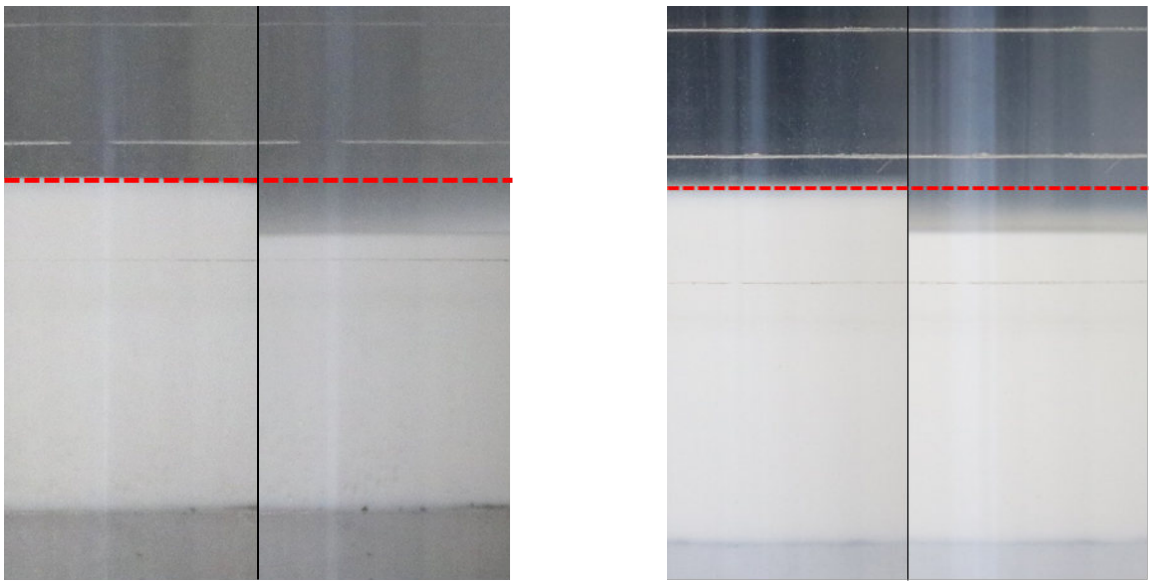

(a) Polymethylacrylate bed (left) after flow-packing, and (right) after vibration (compaction = 18%). Red dashed line indicates initial bed height of ∼25 mm.

(b) CHT bed (left) after flow-packing, and (right) after vibration (compaction = 13%). Red dashed line indicates initial bed height of ∼25 mm.

Fig. 7.6.: Compaction trough vertical linear vibration in a 50 mm column on **(a):** a polymethylacrylate packing, and **(b)**: a ceramiy hydroxyapatite packing. Vibration times were 25 and 20m minutes respectively. The ratio of vibration force to column volume was ∼ 1190 $^{N}/_{l}$.

was measured again with a value of 12.5. The improvement in quality can be seen in Figure 7.7c showing the rHETP decrease after vibration. It was proposed that the local inhomogeneities caused by the channels were corrected as vibration caused adjacent particles to move and reduce the amount of void spaces in the region.

Scale-up of column vibration packing

The scale-up of the vibration-packing methods in 200 mm and 400 mm column was limited due to the lack of space in the columns for vibrator attachment. It was not possible to generate the same kind of vibration as in the successful 50 mm experiments. Instead of being attached to the underside of the column, the vibrators could only be arranged on the sides of the column.

Although vibration-packing in both columns showed additional height compaction (up to 7 % in the 200 mm, and up to 3 % for the 400 mm column for CHT packings), this was not accompanied by improvement in column efficiency. This agreed with observed results from non-vertical and non-linear vibration experiments in the 50 mm column, hinting that the geometry of the generated waves heterogeneously compacted

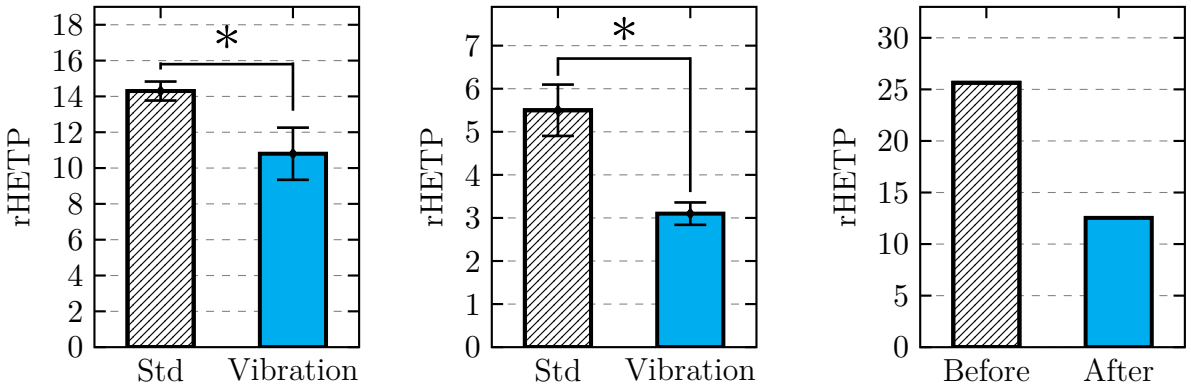

(a) rHETP improvement of 44 % through vibration packing ($P < 0.05$) of polymethylacrylate packings.

(b) rHETP improvement of 25 % through vibration packing ($P < 0.05$) of CHT packings.

(c) Correction of packing defects through in-situ vibration of a polymethylacrylate packing.

Fig. 7.7.: Effect of linear vertical vibration in a 50 mm column **(a) and (b):** during packing of two chromatographic media corresponding to those in Figure 7.6, and **(c):** as correction of channeling defects in an already packed column. Copy of Figs. 6.25b, 6.27b and 6.29b.

the column. This was further confirmed by the observation of a central plateau after vibration seen in Figure 7.8, showing a much denser outer ring-like region of the column caused by the inhomogeneous vibrations.

Even though the possible additional compaction at larger column diameters was observed to be smaller due to the diminished influence of the wall effect, vibration-packing can have a considerable effect on overall process reliability. Obtaining a more stable bed which does not settle or build gaps during operation will allow the column to be used longer and require less re-packing. Re-packing is a time, personnel and resource intensive process. Moreover, large-scale chromatography is often used as one of the last steps in the bioproduction chain, commonly carrying out the last purifying portion of an already concentrated product with a high added value. Thus any improvement on the process reliability and stability would imply considerable advantages in the biomanufacturing process.

Overall, it was shown that current conventional packing methods deliver columns which are far from their most dense and stable state, explaining why the reproducibility of column packing, and long-term stability is often reported to be lacking. The use of adequate mechanical vibration can deliver denser and more efficient beds. It is to be expected that such columns will also be more stable under operation, as their state after vibration is closer to the energetic minimum.

It could also be seen that macroscopic compaction does not necessarily imply a more

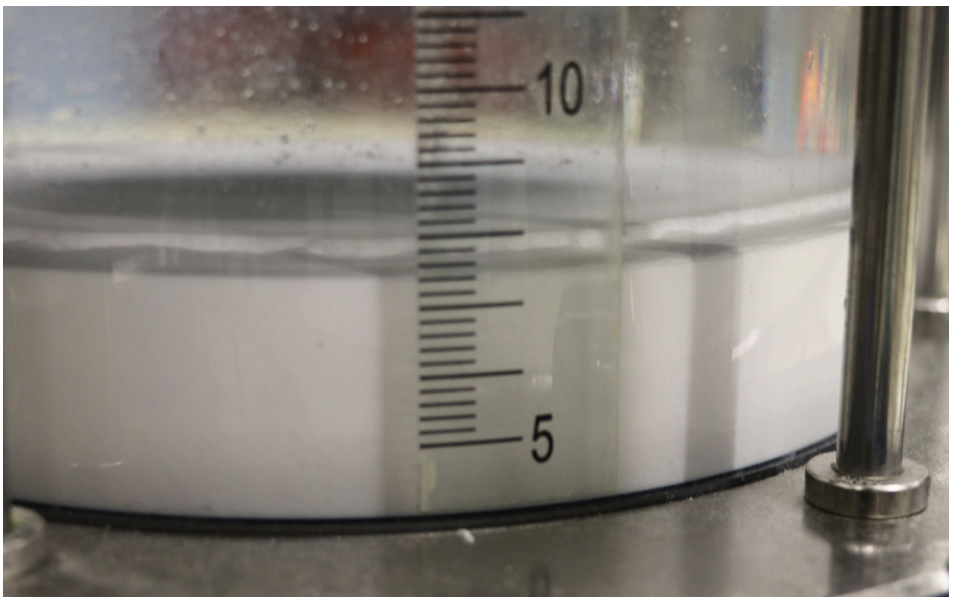

Fig. 7.8.: Inhomogeneous compaction of a polymethylmetacrylate packing in a 200 mm column after mechanical vibration. The outer ring of the packing was more compacted than the central region. Copy of Fig. 6.31

efficient column, which also depends on the microscopic homogeneity of the packing. This is affected by the type of vibration and how it is applied to the system, determining the symmetry of vibration. Linear vibrators located on the underside of the column achieved chromatographic beds with higher efficiencies than those obtained by standard packing methods only. Thus, mechanical vibration was established as an additional packing tool, opening the door to more reliable and efficient packing methods and advancing column packing technology.

8. Outlook

The scale-up of the improved packing methods on larger columns should be continued. A custom-built bottom flow distributor for larger columns would enable the attachment of linear vibrators to the underside of the column as done in the 50 mm column. The distribution of the vibrators should be done symmetrically as shown in Figure 8.1. A direct transfer of the developed packing methods, i.e. vertical linear vibration done either as the last packing step for rigid media, or between flow packing steps for compressible media, could then be made.

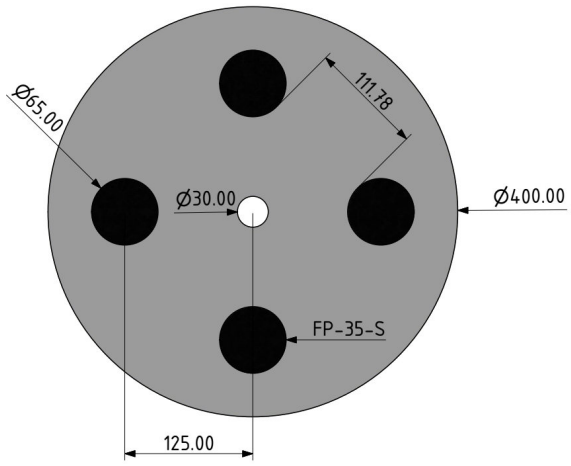

Fig. 8.1.: Symmetric arrangement of four FP-35-S linear vibrators on the underside of a 400 mm column. Gap between vibrators of over 10 cm for process line.

The use of ultrasound during packing can be scaled-up by using multiple transducers embedded in the bottom flow distributor. Wider columns enable the use of larger, more powerful transducers which would improve the energetic input into the column. A possible disadvantage of stronger transducers is the potential for inertial cavitation. To partially avoid this, high-frequency transducers in the MHz-range should be used.

Another possibility is the use of numerous medium-sized transducers distributed along the flow distributor. Such a transducer array could be used to generate signals targeted at specific regions of the packed bed by modulating and phasing the activation

of individual transducers (see Figure 8.2). This principle is well understood and used in medical ultrasound imaging, antennas and radars.

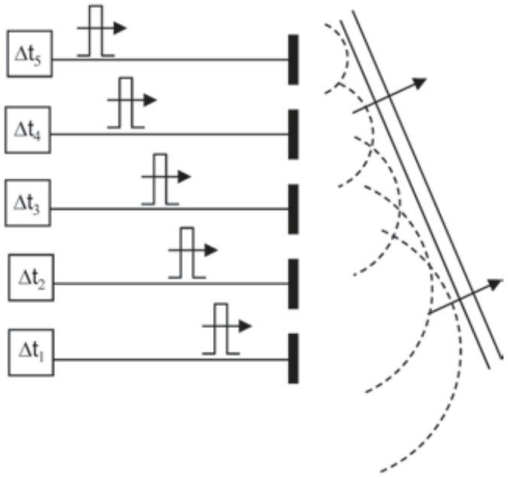

Fig. 8.2.: Principle of phased arrays [89].

The contrast-enhancing method and micro-CT measurements should be used to measure packing structures obtained through different packing methods using the 3 mm column developed in this work. Additionally, the image processing of obtained tomographic images should be further optimized either through novel approaches such as machine learning, or through improved algorithms.

Another phenomenon that can be measured is the change of packing structure under column operation. This can be done by measuring the initial packing structure, washing out the PBM substances from the column and subjecting it to simulated separation cycles. After a determined number of cycles, the structure can be measured again to determine how the packing evolved. The same general procedure could also be used to study particle migration using the particle-tagging method.

List of Figures

List of Tables

Abbreviations

API Active Pharmaceutical Ingredient.

As Peak asymmetry.

CHT Ceramic Hydroxyapatite.

CT Computed Tomography.

DI Deionized.

FFC Face-centered cubic.

FZWB Forschungszentrum für Weise Biotechnologie.

HCP Hexagonal close-packed.

HETP Height of an Equivalent Theoretical Plate.

LC Liquid Chromatography.

Micro-CT Micro Computed Tomography.

PBM Pore-blocking method.

PETG Polyethylene terephthalate glycol-modified.

PMA Polymethylacrylate.

PMMA Poly(methyl methacrylate).

rHETP Reduced HETP.

SEM Scanning electron microscope.

Nomenclature

A Eddy diffusion term.

As Column asymmetry.

B Axial diffusion term.

C Non-equilibrium factor.

F^{Rad} Acoustic radiation force.

L_C Column length.

N_C Number of plates in a column.

R Acoustic reflection.

U^{Rad} Acoustic energy field.

V_S Superficial velocity.

$W_{50\%}$ Peak width at half height.

Z_i Acoustic impedance.

λ Column compaction.

$\langle P^2 \rangle$ Mean acoustic pressure squared field.

$\langle v^2 \rangle$ Mean acoustic velocity squared field.

ϕ Column solids fraction.

ρ_i Density.

ε Column porosity.

a Fronting asymmetry term.

b Tailing asymmetry term.

d_P Particle diameter.

d_c Column diameter.

f_i Particle acoustic contrast factors.

u_{Int} Interstitial velocity.

Bibliography

[1] Brent Erickson, Nelson, and Paul Winters. "Perspective on Opportunities in Industrial Biotechnology in Renewable Chemicals". en. In: *Biotechnology Journal* 7.2 (Feb. 2012), pp. 176–185. ISSN: 18606768. DOI: 10.1002/biot.201100069.

[2] Gunter Festel. "Industrial Biotechnology: Market Size, Company Types, Business Models, and Growth Strategies". en. In: *Industrial Biotechnology* 6.2 (Apr. 2010), pp. 88–94. ISSN: 1550-9087, 1931-8421. DOI: 10.1089/ind.2010.0006.

[3] Eric Valeur et al. "New Modalities for Challenging Targets in Drug Discovery". en. In: *Angewandte Chemie International Edition* 56.35 (Aug. 2017), pp. 10294–10323. ISSN: 14337851. DOI: 10.1002/anie.201611914.

[4] Horst Chmiel, Ralf Takors, and Dirk Weuster-Botz, eds. *Bioprozesstechnik*. de. 4. Auflage. Berlin: Springer Spektrum, 2018. ISBN: 978-3-662-54041-1 978-3-662-54042-8.

[5] Schmidt-Traub, Michael Schulte, and Andreas Seidel-Morgenstern. *Preparative Chromatography*. 2012.

[6] Stefan Bruns et al. "Slurry Concentration Effects on the Bed Morphology and Separation Efficiency of Capillaries Packed with Sub-2 Mm Particles". In: *Journal of Chromatography A* 1318 (Nov. 2013), pp. 189–197. ISSN: 0021-9673. DOI: 10.1016/j.chroma.2013.10.017.

[7] Siarhei Khirevich et al. “Geometrical and Topological Measures for Hydrodynamic Dispersion in Confined Sphere Packings at Low Column-to-Particle Diameter Ratios”. In: *Journal of Chromatography A* 1262 (Nov. 2012), pp. 77–91. ISSN: 0021-9673. DOI: 10.1016/j.chroma.2012.08.086.

[8] Mark R. Schure and Robert S. Maier. “How Does Column Packing Microstructure Affect Column Efficiency in Liquid Chromatography?” In: *Journal of Chromatography A*. The Role of Theory in Chromatography 1126.1–2 (Sept. 2006), pp. 58–69. ISSN: 0021-9673. DOI: 10.1016/j.chroma.2006.05.066.

[9] Tosoh Biosciences. *Toyopearl Instruction Manual*. en. https://www.separations.eu.tosohbioscience.com/TBG/Products%20Download/Instruction%20Manual/m15p73a.pdf.

[10] Bio-Rad Laboratories. *CHT Ceramic Hydroxyapatite Instruction Manual*. https://www.bio-rad.com/webroot/web/pdf/lsr/literature/LIT611E.PDF.

[11] *Sepharose Fast Flow - Ion Exchange Media- Instructions*.

[12] R. Andrew Shalliker et al. “Visualization of Bed Compression in an Axial Compression Liquid Chromatography Column”. In: *Journal of Chromatography A* 977.2 (Nov. 2002), pp. 213–223. ISSN: 0021-9673. DOI: 10.1016/S0021-9673(02)01273-6.

[13] M. Dorn et al. “Influence of Different Packing Methods on the Hydrodynamic Stability of Chromatography Columns”. en. In: *Journal of Chromatography A* 1516 (Sept. 2017), pp. 89–101. ISSN: 00219673. DOI: 10.1016/j.chroma.2017.08.019.

[14] Martin Dorn and Dariusch Hekmat. “Simulation of the Dynamic Packing Behavior of Preparative Chromatography Columns via Discrete Particle Modeling”. In: *Biotechnology Progress* 32.2 (Nov. 2015), pp. 363–371. ISSN: 87567938. DOI: 10.1002/btpr.2210.

[15] Dzmitry Hlushkou, Stanislau Piatrusha, and Ulrich Tallarek. “Impact of Diffusion on Transverse Dispersion in Two-Dimensional Ordered and Random Porous Media”. en. In: *Physical Review E* 95.6 (June 2017), p. 063108. ISSN: 2470-0045, 2470-0053. DOI: 10.1103/PhysRevE.95.063108.

[16] R. Andrew Shalliker, B. Scott Broyles, and Georges Guiochon. “Physical Evidence of Two Wall Effects in Liquid Chromatography”. In: *Journal of Chromatography A* 888.1–2 (Aug. 2000), pp. 1–12. ISSN: 0021-9673. DOI: 10.1016/S0021-9673(00)00517-3.

[17] Arved E. Reising et al. “Bed Morphological Features Associated with an Optimal Slurry Concentration for Reproducible Preparation of Efficient Capillary Ultrahigh Pressure Liquid Chromatography Columns”. en. In: *Journal of Chromatography A* 1504 (June 2017), pp. 71–82. ISSN: 00219673. DOI: 10.1016/j.chroma.2017.05.007.

[18] Rezvan Abedini, Amir Abdullah, and Yunes Alizadeh. “Ultrasonic Assisted Hot Metal Powder Compaction”. en. In: *Ultrasonics Sonochemistry* 38 (Sept. 2017), pp. 704–710. ISSN: 13504177. DOI: 10.1016/j.ultsonch.2016.09.025.

[19] Justin M. Godinho et al. “Implementation of High Slurry Concentration and Sonication to Pack High-Efficiency, Meter-Long Capillary Ultrahigh Pressure Liquid Chromatography Columns”. en. In: *Journal of Chromatography A* 1462 (Sept. 2016), pp. 165–169. ISSN: 00219673. DOI: 10.1016/j.chroma.2016.08.002.

[20] R. Andrew Shalliker, B. Scott Broyles, and Georges Guiochon. “Evaluation of the Secondary Consolidation of Columns for Liquid Chromatography by Ultrasonic Irradiation”. In: *Journal of Chromatography A* 878.2 (2000), pp. 153–163.

[21] Evelien Moorkens et al. “The Market of Biopharmaceutical Medicines: A Snapshot of a Diverse Industrial Landscape”. en. In: *Frontiers in Pharmacology* 8 (June 2017). ISSN: 1663-9812. DOI: 10.3389/fphar.2017.00314.

[22] Georges Guiochon and Lois Ann Beaver. “Separation Science Is the Key to Successful Biopharmaceuticals”. en. In: *Journal of Chromatography A* 1218.49 (Dec. 2011), pp. 8836–8858. ISSN: 00219673. DOI: 10.1016/j.chroma.2011.09.008.

[23] Georges Guiochon. “Monolithic Columns in High-Performance Liquid Chromatography”. In: *Journal of Chromatography A*. Editors’ Choice I 1168.1–2 (Oct. 2007), pp. 101–168. ISSN: 0021-9673. DOI: 10.1016/j.chroma.2007.05.090.

[24] Pete Gagnon. “Monoclonal Antibody Purification with Hydroxyapatite”. In: *New Biotechnology*. Special Issue: Biotechnology Annual Review 2009 25.5 (June 2009), pp. 287–293. ISSN: 1871-6784. DOI: 10.1016/j.nbt.2009.03.017.

[25] Sun Chau Siu et al. “Packing of Large-Scale Chromatography Columns with Irregularly Shaped Glass Based Resins Using a Stop-Flow Method”. en. In: *Biotechnology Progress* 30.6 (Nov. 2014), pp. 1319–1325. ISSN: 87567938. DOI: 10.1002/btpr.1962.

[26] Gauss C. F. "Besprechung Des Buchs von L. A. Seeber: Intersuchungen Über Die Eigenschaften Der Positiven Ternären Quadratischen Formen Usw". In: *Göttingsche Gelehrte Anzeigen* 2 (1831), pp. 188–196.

[27] J. J. van Deemter, Zuiderweg F. J., and Klinkenberg A. "Longitudinal Diffusion and Resistance to Mass Transfer as Causes of Nonideality in Chromatography". In: *Chemical Engineering Science* 5 (Feb. 1956), pp. 271–289.

[28] Klaus K. Unger et al. "Liquid Chromatography-Its Development and Key Role in Life Science Applications". en. In: *Angewandte Chemie International Edition* 49.13 (Mar. 2010), pp. 2300–2312. ISSN: 14337851. DOI: 10.1002/anie.200906976.

[29] Pete Gagnon et al. "Practical Issues in the Industrial Use of Hydroxyapatite for Purification of Monoclonal Antibodies". en. In: (), p. 35.

[30] Arne Staby et al. "Comparison of Chromatographic Ion-Exchange Resins". en. In: *Journal of Chromatography A* 1069.1 (Mar. 2005), pp. 65–77. ISSN: 00219673. DOI: 10.1016/j.chroma.2004.11.094.

[31] John H. Knox and Jon F. Parcher. "Effect of Column to Particle Diameter Ratio on the Dispersion of Unsorbed Solutes in Chromatograph". In: *Analytical Chemistry* 41.12 (1969), pp. 1599–1606.

[32] Mark R. Schure et al. "Simulation of Packed-Bed Chromatography Utilizing High-Resolution Flow Fields: Comparison with Models". en. In: *Analytical Chemistry* 74.23 (Dec. 2002), pp. 6006–6016. ISSN: 0003-2700, 1520-6882. DOI: 10.1021/ac0204101.

[33] J. J. Kirkland and J. J. DeStefano. "The Art and Science of Forming Packed Analytical High-Performance Liquid Chromatography Columns". In: *Journal of Chromatography A*. The Role of Theory in Chromatography 1126.1–2 (Sept. 2006), pp. 50–57. ISSN: 0021-9673. DOI: 10.1016/j.chroma.2006.04.027.

[34] Heinrich M. Jaeger, Sidney R. Nagel, and Robert P. Behringer. "Granular Solids, Liquids, and Gases". In: *Reviews of modern physics* 68.4 (1996), p. 1259.

[35] Hernán A. Makse, Jasna Brujić, and Sam F. Edwards. "Statistical Mechanics of Jammed Matter". en. In: *The Physics of Granular Media*. Weinheim, FRG, June 2005, pp. 45–85. ISBN: 978-3-527-60362-6 978-3-527-40373-8. DOI: 10.1002/352760362X.ch3.

[36] Andrea J. Liu and Sidney R. Nagel. "Nonlinear Dynamics: Jamming Is Not Just Cool Any More". In: *Nature* 396.6706 (1998), pp. 21–22.

[37] Jonathan Kollmer, Scott M. Lindauer, and Karen E. Daniels. "Digging on Asteroids: A Laboratory Model of Granular Dynamics in Microgravity". In: *ASCE Proceedings for Earth & Space Conf.* (2016), pp. 195–201. DOI: 10.1061/9780784479971.021.

[38] Anita Mehta. "Spatial, Dynamical and Spatiotemporal Heterogeneities in Granular Media". en. In: *Soft Matter* 6.13 (June 2010), pp. 2875–2883. ISSN: 1744-6848. DOI: 10.1039/B926809J.

[39] Qicheng Sun, Guangqian Wang, and Kaiheng Hu. "Some Open Problems in Granular Matter Mechanics". en. In: *Progress in Natural Science* 19.5 (May 2009), pp. 523–529. ISSN: 10020071. DOI: 10.1016/j.pnsc.2008.06.023.

[40] Fabrice Gritti and Georges Guiochon. "The Current Revolution in Column Technology: How It Began, Where Is It Going?" In: *Journal of Chromatography A*. High-Performance Columns and Their Operations: The Speed, Efficiency and Peak Capacity Obtainable with High-Performance Columns under Various Operation Conditions 1228 (Mar. 2012), pp. 2–19. ISSN: 0021-9673. DOI: 10.1016/j.chroma.2011.07.014.

[41] Ruili Wang, Eric Habib, and X.X. Zhu. "Application of Close-Packed Structures in Dental Resin Composites". en. In: *Dental Materials* 33.3 (Mar. 2017), pp. 288–293. ISSN: 01095641. DOI: 10.1016/j.dental.2016.12.006.

[42] C. Hanotin et al. "Vibration-Induced Liquefaction of Granular Suspensions". en. In: *Physical Review Letters* 108.19 (May 2012). ISSN: 0031-9007, 1079-7114. DOI: 10.1103/PhysRevLett.108.198301.

[43] K. Chen et al. "Packing Grains by Thermal Cycling". en. In: *Nature* 442.7100 (July 2006), pp. 257–257. ISSN: 0028-0836, 1476-4687. DOI: 10.1038/442257a.

[44] Alexis Tariot, Georges Gauthier, and Philippe Gondret. "Granular Compaction by Fluidization". en. In: *EPJ Web of Conferences* 140 (2017), p. 10003. ISSN: 2100-014X. DOI: 10.1051/epjconf/201714010003.

[45] C. J. Olson Reichhardt et al. "Softening of Granular Packings with Dynamic Forcing". In: *Physical Review E* 92.2 (Aug. 2015). ISSN: 1539-3755, 1550-2376. DOI: 10.1103/PhysRevE.92.022203. arXiv: 1406.4529.

[46] Zorica Jakši and Darko Vasiljevi. "Compaction Dynamics of Vibrated Granular Materials". en. In: (2012), p. 6.

[47] Xiaoping Jia, Th. Brunet, and J. Laurent. "Elastic Weakening of a Dense Granular Pack by Acoustic Fluidization: Slipping, Compaction, and Aging". en. In: *Physical Review E* 84.2 (Aug. 2011). ISSN: 1539-3755, 1550-2376. DOI: 10.1103/PhysRevE.84.020301.

[48] Xiaoping Jia, C. Caroli, and B. Velicky. "Ultrasound Propagation in Externally Stressed Granular Media". In: *Physical Review Letters* 82.9 (1999), p. 1863.

[49] Andrew Feeney et al. "An Ultrasonic Compactor for Oil and Gas Exploration". en. In: *Physics Procedia* 87 (2016), pp. 72–78. ISSN: 18753892. DOI: 10.1016/j.phpro.2016.12.012.

[50] Marina Levina and Michael H. Rubinstein. "The Effect of Ultrasonic Vibration on the Compaction Characteristics of Ibuprofen". In: *Drug Development and Industrial Pharmacy* 28.5 (Jan. 2002), pp. 495–514. ISSN: 0363-9045. DOI: 10.1081/DDC-120003446.

[51] Marina Levina and Michael H. Rubinstein. "The Effect of Ultrasonic Vibration on the Compaction Characteristics of Paracetamol". In: *Journal of pharmaceutical sciences* 89.6 (2000), pp. 705–723.

[52] Vahid Fartashvand, Amir Abdullah, and Seyed Ali Sadough Vanini. "Effects of High Power Ultrasonic Vibration on the Cold Compaction of Titanium". en. In: *Ultrasonics Sonochemistry* 36 (May 2017), pp. 155–161. ISSN: 13504177. DOI: 10.1016/j.ultsonch.2016.11.017.

[53] Martin Franc et al. "Performance and Lifetime of Slurry Packed Capillary Columns for High Performance Liquid Chromatography". In: *Chemical Papers* 68.1 (2013), pp. 22–28.

[54] S. Kiesgen de Richter et al. "Vibration-Induced Compaction of Granular Suspensions". en. In: *The European Physical Journal E* 38.7 (July 2015). ISSN: 1292-8941, 1292-895X. DOI: 10.1140/epje/i2015-15074-7.

[55] Venkatesh Natarajan, Anthony Frederick Mann, and Daniel Schubnel. "Method of and Device for Packing a Chromatography Column". US20100084342 A1. Apr. 2010.

[56] William R. Hendee and E. Russell Ritenour. *Medical Imaging Physics*. en. 4th ed. New York: Wiley-Liss, 2002. ISBN: 978-0-471-38226-3.

[57] Martin Hofmann and David Johnson. "Detection Systems and Methods". US20070138100 A1. June 2007.

[58] Nimrod M Tole et al. *Basic Physics of Ultrasonographic Imaging*. en. Geneva: World Health Organization, 2005. ISBN: 978-92-4-159299-4.

[59] Frederick W. Kremkau. *Sonography Principlese and Instruments*. English. Elsevier Health Sciences, Nov. 2015. ISBN: 0-323-32271-9.

[60] Tung Manh et al. "Microfabrication of Stacks of Acoustic Matching Layers for 15MHz Ultrasonic Transducers". en. In: *Ultrasonics* 54.2 (Feb. 2014), pp. 614–620. ISSN: 0041624X. DOI: 10.1016/j.ultras.2013.08.015.

[61] Henrik Bruus. "Acoustofluidics 1: Governing Equations in Microfluidics". en. In: *Lab on a Chip* 11.22 (Oct. 2011), pp. 3742–3751. ISSN: 1473-0189. DOI: 10.1039/C1LC20658C.

[62] Peter Barkholt Muller et al. "A Numerical Study of Microparticle Acoustophoresis Driven by Acoustic Radiation Forces and Streaming-Induced Drag Forces". en. In: *Lab on a Chip* 12.22 (Oct. 2012), pp. 4617–4627. ISSN: 1473-0189. DOI: 10.1039/C2LC40612H.

[63] P. C. R. Courtney et al. "Manipulation of Microparticles Using Phase-Controllable Ultrasonic Standing Waves." In: *The Journal of the Acoustical Society of America* 128 (Oct. 2010), EL195–EL199. ISSN: 1520-8524. DOI: 10.1121/1.3479976.

[64] Martin Wiklund, Roy Green, and Mathias Ohlin. "Acoustofluidics 14: Applications of Acoustic Streaming in Microfluidic Devices". In: *Lab Chip* 12 (2012), pp. 2438–2451.

[65] R.J. Boughtflower, T. Underwood, and J. Maddin. "The Production of Packed Capillaries Using a Novel Pressurised Ultrasound Device". In: *Chromatographia* 41.7/8 (Oct. 1995).

[66] Steffen Ehlert, Thomas Rösler, and Ulrich Tallarek. "Packing Density of Slurry-Packed Capillaries at Low Aspect Ratios". en. In: *Journal of Separation Science* 31.10 (June 2008), pp. 1719–1728. ISSN: 16159306, 16159314. DOI: 10.1002/jssc.200800018.

[67] Steffen Ehlert et al. "Separation Efficiency of Particle-Packed HPLC Microchips". en. In: *Analytical Chemistry* 80.15 (Aug. 2008), pp. 5945–5950. ISSN: 0003-2700, 1520-6882. DOI: 10.1021/ac800576v.

[68] Steffen Ehlert. "High-Performance Liquid Chromatography with Packed Microchips". PhD thesis. Magdeburg: Philipps - Universität Marburg, 2010.

[69] Robert E. Apfel and Christy K. Holland. “Gauging the Likelihood of Cavitation from Short-Pulse, Low-Duty Cycle Diagnostic Ultrasound”. In: *Ultrasound in medicine & biology* 17.2 (1991), pp. 179–185.

[70] Stefan Bruns and Ulrich Tallarek. “Physical Reconstruction of Packed Beds and Their Morphological Analysis: Core–Shell Packings as an Example”. In: *Journal of Chromatography A* 1218.14 (Apr. 2011), pp. 1849–1860. ISSN: 0021-9673. DOI: 10.1016/j.chroma.2011.02.013.

[71] Dorthe Wildenschild and Adrian P. Sheppard. “X-Ray Imaging and Analysis Techniques for Quantifying Pore-Scale Structure and Processes in Subsurface Porous Medium Systems”. en. In: *Advances in Water Resources* 51 (Jan. 2013), pp. 217–246. ISSN: 03091708. DOI: 10.1016/j.advwatres.2012.07.018.

[72] L. De Chiffre et al. “Industrial Applications of Computed Tomography”. en. In: *CIRP Annals - Manufacturing Technology* 63.2 (2014), pp. 655–677. ISSN: 00078506. DOI: 10.1016/j.cirp.2014.05.011.

[73] L. Leu et al. “Fast X-Ray Micro-Tomography of Multiphase Flow in Berea Sandstone: A Sensitivity Study on Image Processing”. en. In: *Transport in Porous Media* 105.2 (Nov. 2014), pp. 451–469. ISSN: 0169-3913, 1573-1634. DOI: 10.1007/s11242-014-0378-4.

[74] T.F. Johnson et al. “X-Ray Computed Tomography of Packed Bed Chromatography Columns for Three Dimensional Imaging and Analysis”. en. In: *Journal of Chromatography A* 1487 (Mar. 2017), pp. 108–115. ISSN: 00219673. DOI: 10.1016/j.chroma.2017.01.013.

[75] Peter DePhillips and Abraham M. Lenhoff. “Pore Size Distributions of Cation-Exchange Adsorbents Determined by Inverse Size-Exclusion Chromatography”. In: *Journal of Chromatography A* 883.1 (2000), pp. 39–54. DOI: 10.1016/S0021-9673(00)00420-9.

[76] Irma Schmidt et al. “Estimation of Chromatographic Columns Performances Using Computer Tomography and CFD Simulations”. en. In: *Chemie Ingenieur Technik* 83.1-2 (Jan. 2011), pp. 130–142. ISSN: 0009286X. DOI: 10.1002/cite.201000171.

[77] Irma Schmidt, Mirjana Minceva, and Wolfgang Arlt. “Selection of Stationary Phase Particle Geometry Using X-Ray Computed Tomography and Computa-

tional Fluid Dynamics Simulations". en. In: *Journal of Chromatography A* 1225 (Feb. 2012), pp. 141–149. ISSN: 00219673. DOI: 10.1016/j.chroma.2011.12.072.

[78] Yan Yao and Abraham M. Lenhoff. "Pore Size Distributions of Ion Exchangers and Relation to Protein Binding Capacity". en. In: *Journal of Chromatography A* 1126.1-2 (Sept. 2006), pp. 107–119. ISSN: 00219673. DOI: 10.1016/j.chroma.2006.06.057.

[79] Volker Deutsch, Michael Platte, and Manfred Vogt. *Ultraschallprüfung: Grundlagen und industrielle Anwendungen*. de. reprint von 1997. VDI-Buch. Berlin: Springer, 1997. ISBN: 978-3-642-63864-0.

[80] *Selection Guide for Industrial Vibrators.Pdf*. https://www.clevelandvibrator.com/images/Do

[81] *Prosep Ultra Plus Affinity Chromatography Media*.

[82] Curtis T. Rueden et al. "ImageJ2: ImageJ for the next Generation of Scientific Image Data". In: *BMC Bioinformatics* 18.1 (Nov. 2017), p. 529. ISSN: 1471-2105. DOI: 10.1186/s12859-017-1934-z.

[83] N. Otsu. "A Threshold Selection Method from Gray-Level Histograms". In: *IEEE Transactions on Systems, Man, and Cybernetics* 9.1 (Jan. 1979), pp. 62–66. ISSN: 0018-9472. DOI: 10.1109/TSMC.1979.4310076.

[84] Bradley E. Treeby et al. "Modeling Nonlinear Ultrasound Propagation in Heterogeneous Media with Power Law Absorption Using a K-Space Pseudospectral Method". In: *The Journal of the Acoustical Society of America* 131.6 (2012), pp. 4324–4336.

[85] C. Kloss et al. "Models , Algorithms and Validation for Opensource DEM and CFD-DEM". In: *Pcfd* 12 (2012), pp. 140–152. ISSN: 1468-4349. DOI: 10.1504/PCFD.2012.047457.

[86] Deirdre Cabooter et al. "Total Pore Blocking as an Alternative Method for the On-Column Determination of the External Porosity of Packed and Monolithic Reversed-Phase Columns". en. In: *Journal of Chromatography A* 1157.1-2 (July 2007), pp. 131–141. ISSN: 00219673. DOI: 10.1016/j.chroma.2007.04.053.

[87] Anil Govindrao Ghom. *Textbook of Oral Radiology - E-Book*. en. Elsevier Health Sciences, Mar. 2017. ISBN: 978-81-312-4024-3.

[88] Junjun Lei, Martyn Hill, and Peter Glynne-Jones. "Numerical Simulation of 3D Boundary-Driven Acoustic Streaming in Microfluidic Devices". en. In: *Lab on a Chip* 14.3 (Dec. 2013), pp. 532–541. ISSN: 1473-0189. DOI: 10.1039/C3LC50985K.

[89] Lester W. Schmerr. *Fundamentals of Ultrasonic Phased Arrays*. en. Vol. 215. Solid Mechanics and Its Applications. Cham: Springer International Publishing, 2015. ISBN: 978-3-319-07271-5 978-3-319-07272-2.

Appendices

A. X-ray tomography processing

A.1. 760 µm column

A.1.1. Binarization of Toyopearl SP-650M Tomographs

```
run("Kuwahara Filter", "sampling=3");
run("Median...", "radius=3");
run("Enhance Contrast...", "saturated=0.3 normalize equalize");
run("Auto Local Threshold", "method=Otsu radius=18 parameter_1=0 parameter_2=0 white");
run("Convert to Mask");
run("Watershed");
run("Morphological Filters", "operation=Opening element=Disk radius=3");
run("Make Binary");
run("Max Inscribed Circles", "minimum=12 use minimum_0=0.90 closeness=5");
roiManager("Show All without labels");
roiManager("Set Fill Color", "black");
run("Subtract Background...", "rolling=50 light create");
run("Flatten");
run("8-bit");
setOption("BlackBackground", false);
run("Make Binary");
roiManager("Delete");
run("Watershed");
// For the entire image stack
run("Morphological Filters (3D)", "operation=Opening element=Ball x-radius=5 y-radius=5 z-radius=5");
run("Watershed");
run("Morphological Filters", "operation=Opening element=Disk radius=1");
run("Morphological Filters", "operation=Dilation element=Disk radius=3");
run("Watershed");
run("Invert", "stack");
```

A.1.2. Binarization of CaptoQ ImpRes Tomographs

```
run("Kuwahara Filter", "sampling=3");
run("Median...", "radius=1");
run("Enhance Contrast...", "saturated=0.3 normalize equalize");
run("Auto Local Threshold", "method=Otsu radius=20 parameter_1=0 parameter_2=0 white");
run("Make Binary");
run("Max Inscribed Circles", "minimum=8 use minimum_0=0.90 closeness=5");
roiManager("Show All without labels");
roiManager("Set Fill Color", "black");
run("Subtract Background...", "rolling=50 light create");
run("Flatten");
run("8-bit");
setOption("BlackBackground", false);
run("Make Binary");
roiManager("Delete");
```

```
run("Watershed");
// For the entired image stack
run("Morphological Filters (3D)", "operation=Opening element=Ball x-radius=2 y-radius=2 z-radius=2");
run("Watershed");
run("Morphological Filters", "operation=Opening element=Disk radius=1");
run("Morphological Filters", "operation=Dilation element=Disk radius=2");
run("Watershed");
run("Invert", "stack");
```

A.1.3. Finding void spaces in the Toyopearl SP-650M packing

```
//setBatchMode(true);
run("Image Sequence...", "open=$PATH$ sort");
run("Invert", "stack");
rename("All_Voids_Black.tiff");
//--- Generating all voids - white
selectWindow("All_Voids_Black.tiff");
run("Duplicate...", "duplicate");
makeOval(13, 39, 384, 384);
run("Invert");
rename("All_Voids_White.tiff");
//--- Carrying out Distance Transform 3D
selectWindow("All_Voids_Black.tiff");
run("Distance Transform 3D");
//--- Ignoring values outside column
makeOval(13, 39, 384, 384);
run("Clear Outside", "stack");
setAutoThreshold("Default dark");
setThreshold(15.0000, 50.0000);
run("Make Binary", "method=Default background=Dark black");
run("Morphological Filters (3D)", "operation=Dilation element=Ball x-radius=15 y-radius=15 z-radius=15");
rename("Dilated_Goal_Voids.tiff");
imageCalculator("AND create stack", "Dilated_Goal_Voids.tiff","All_Voids_White.tiff");
rename("Final_Voids.tiff");
//setBatchMode(false);
```

A.1.4. Finding void spaces in the CaptoQ ImpRes packing

```
//setBatchMode(true);
run("Close All");
run("Image Sequence...", "open=$PATH$ sort");
run("Invert", "stack");
rename("All_Voids_Black.tiff");
//--- Generating all voids - white
selectWindow("All_Voids_Black.tiff");
run("Duplicate...", "duplicate");
makeOval(30, 23, 385, 385);
run("Invert");
rename("All_Voids_White.tiff");
//--- Carrying out Distance Transform 3D
selectWindow("All_Voids_Black.tiff");
run("Distance Transform 3D");
//--- Ignoring values outside column
makeOval(30, 23, 385, 385);
run("Clear Outside", "stack");
setAutoThreshold("Default dark");
setThreshold(10.0000, 19.3400);
run("Make Binary", "method=Default background=Dark black");
run("Morphological Filters (3D)", "operation=Dilation element=Ball x-radius=10 y-radius=10 z-radius=10");
rename("Dilated_Goal_Voids.tiff");
//--- Deleting elements outside column
imageCalculator("AND create stack", "Dilated_Goal_Voids.tiff","All_Voids_White.tiff");
rename("Final_Voids.tiff");
```

B. Acoustic simulations

B.1. K-Wave Simulation of acoustic field inside the 50 mm column

```
% This function recreates an empty column with a transducer on top/bottom and no
% particles inside - All 2D, elastic function
% Elastic --> No non-linearity, Alpha coefficient is assumed to be 2

clearvars
%==========================================================================
% MAIN PARAMETER INPUT
%==========================================================================
% Source signal parameters
source_freq =0.82e6;          % [Hz]
source_mag = 0.1e6;           % [Pa] bar = 100kPa, 0.1MPa
t_end = 10e-5;          % Sim time
Scale_Sim=2;           % Sim scale

sensor.record = {'p_rms','u_rms','p_max'};
Trans_Diam_Orig = 15e-3;       % [m]
Column_ID = 50e-3;         % [m]
Column_OD = 58e-3;       % [m]
Options = [1 1 1 1];           % 1-Column wall, 2-Stainles steel bottom, 3-Particles, 4-Bottom transducer
Desired_Porosity=0.4;       % Bed porosity, if necessary
Starting_Level_Particles=20e-3;

% set desired grid size in the x-direction not including the PML
Length_X = 60e-3;             % [m] - remember, X-direction is vertical
Depth_Bottom = 50e-3;                % [m], depth of the bottom, either glass or steel, measured from the transducer face
cfl    = 0.12;

Wait_For_Confirmation =1;    % if ==1, a pic of the maks will be showed before simulation
Visualize=1;
Save_Variables = 0;           % if ==1, the variables will be saved in the folder
Mat_Filename = 'AMM_CE2D_190516.mat';        % CHECK THE NAME. Make sure a file with its name is not already present
%==========================================================================
% SIM PARAMETERS - DEFINE THE K-WAVE GRID
%==========================================================================
% set the size of the perfectly matched layer (PML)
PML_X_SIZE = 10;              % [grid points]
PML_Y_SIZE = 10;              % [grid points]
% checkFactors(100, 150)
% Numbers with a maximum prime factor of 2
% 16    32    64   128   256   512
% Numbers with a maximum prime factor of 3
% 12    18    24    27    36    48    54    72    81    96   108   144   162   192   216   243   288   324   384   432   486   576   648   729
       768   864   972% set total number of grid points not including the PML
Nx = 512*Scale_Sim - 2*PML_X_SIZE;      % [grid points]
Ny = 512*Scale_Sim - 2*PML_Y_SIZE;      % [grid points]
% calculate the spacing between the grid points
dx = Length_X/Nx;             % [m]
dy = dx;                      % [m]
```

```
Length_Y = dy*Ny;               % [m]
disp('-----------------------------------------')
disp(['The dimensions of the simulated region are: ',num2str(Length_X*100),'cm in X, and ', num2str(Length_Y*100), 'cm in Y '])
disp(['The resolutions are: ',num2str(dx*1000),'mm in X, and ', num2str(dy*1000), 'mm in Y'])
disp('-----------------------------------------')
% create the k-space grid
kgrid = makeGrid(Nx, dx, Ny, dy);

%==========================================================================
% MATERIAL PROPERTIES
%==========================================================================
% Water
Sound_Compr_Water = 1500;       % m/s
Sound_Shear_Water = 0;          % m/s
Density_Water =1000;            % kg/m3
alpha0_p_Water = 0.002;         % compressional wave absorption [dB/(MHz^2 cm)]
alpha0_s_Water = 0;             % shear wave absorption [dB/(MHz^2 cm)]
alpha_power_Water = 2;          % Exponent=2 is assumed in elastic fn
BonA_Water = 5.2;               %
% Column material - PMMA
Sound_Compr_PMMA = 2590;        % m/s
Sound_Shear_PMMA = 0;           % m/s
Density_PMMA =1150;             % kg/m3
alpha0_p_PMMA = 16.8;           % compressional wave absorption [dB/(MHz^2 cm)]
alpha0_s_PMMA = 0;              % shear wave absorption [dB/(MHz^2 cm)]
alpha_power_PMMA = 0.8;         % Exponent=2 is assumed in elastic fn
BonA_PMMA = 1.2;                %
% Bottom face - Stainless steel 316
Sound_Compr_Steel = 5720;       % m/s
Sound_Shear_Steel = 3272;       % m/s
Density_Steel =7700;            % kg/m3
alpha0_p_Steel = 0.002;         % compressional wave absorption [dB/(MHz^2 cm)]
alpha0_s_Steel = 0;             % shear wave absorption [dB/(MHz^2 cm)]
alpha_power_Steel = 2;          % Exponent=2 is assumed in elastic fn
BonA_Steel = 5.2;               %
% Bottom face - PE-Frit, approximated as a PE-sheet.
Sound_Compr_PELD = 2000;        % m/s
Sound_Shear_PELD = 940;         % m/s
Density_PELD =920;              % kg/m3
alpha0_p_PELD = 0.002;          % compressional wave absorption [dB/(MHz^2 cm)]
alpha0_s_PELDl = 0;             % shear wave absorption [dB/(MHz^2 cm)]
alpha_power_PELD = 2;           % Exponent=2 is assumed in elastic fn
BonA_PELD = 5.2;                %
% Chromatographic media - Sepharose (STAND IN PROPERTIES OF BONE!)
Sound_Compr_Seph = 1480; % m/s Hoffman-Patent has info on it
Sound_Shear_Seph = 10;   % m/s
Density_Seph =1100;      % kg/m3
alpha0_p_Seph = .2;      % compressional wave absorption [dB/(MHz^2 cm)]
alpha0_s_Seph = .2;      % shear wave absorption [dB/(MHz^2 cm)]
% Chromatographic media - Toyopearl
Sound_Compr_Toyo = 1550; % m/s
Sound_Shear_Toyo = 10;   % m/s
Density_Toyo=1100;       % kg/m3
alpha0_p_Toyo = .2;      % compressional wave absorption [dB/(MHz^2 cm)]
alpha0_s_Toyo= .2;       % shear wave absorption [dB/(MHz^2 cm)]
% Media - glass beads (Lidon_2016)
Sound_Compr_Glass = 4540; % m/s
Sound_Shear_Glass = 3280;   % m/s
Density_Glass=2500;         % kg/m3
alpha0_p_Glass = .03;       % compressional wave absorption [dB/(MHz^2 cm)]
alpha0_s_Glass= .2;         % shear wave absorption [dB/(MHz^2 cm)]
BonA_Glass = 0;

%==========================================================================
% DEFINE ELEMENTS - ASSIGN PROPERTIES
%==========================================================================
% Propagation medium - water
medium.sound_speed_compression  = Sound_Compr_Water*ones(Nx, Ny);
medium.sound_speed_shear  = Sound_Shear_Water*ones(Nx, Ny);
medium.density  = Density_Water*ones(Nx, Ny);
medium.alpha_coeff_compression  = alpha0_p_Water*ones(Nx, Ny);
```

```
119 medium.alpha_coeff_shear  = alpha0_s_Water*ones(Nx, Ny);
120 %-------- Column - PMMA
121 Column_Mask = zeros(Nx,Ny);
122 Aux_Mask = zeros(1,Ny);
123 Column_ID_GridPoints = Column_ID/dy;
124 Column_OD_GridPoints = Column_OD/dy;
125 Left_x_ID=round(Ny/2-(Column_ID_GridPoints/2));
126 Right_x_ID=round(Ny/2+(Column_ID_GridPoints/2));
127 Left_x_OD=round(Ny/2-(Column_OD_GridPoints/2));
128 Right_x_OD=round(Ny/2+(Column_OD_GridPoints/2));
129 Aux_Mask(1,Left_x_OD:Left_x_ID)=1;
130 Aux_Mask(1,Right_x_ID:Right_x_OD)=1;
131 if Options(1)==1;
132 oo=1;
133 while oo<Nx
134 Column_Mask(oo,:)=Aux_Mask;
135 oo=oo+1;
136 end
137 %figure, imshow(Column_Mask);
138 medium.density(Column_Mask==1)=Density_PMMA;
139 medium.sound_speed_compression(Column_Mask==1)  = Sound_Compr_PMMA;
140 medium.sound_speed_shear(Column_Mask==1)  = Sound_Shear_PMMA;
141 medium.alpha_coeff_compression(Column_Mask==1)  = alpha0_p_PMMA;
142 medium.alpha_coeff_shear(Column_Mask==1)  = alpha0_s_PMMA;
143 end
144
145 %---------- STEEL BOTTOM
146 Depth_Bottom_GridPoints =round(Depth_Bottom/dx);
147 Bottom_Mask = zeros(Nx,Ny);
148 Bottom_Mask(Depth_Bottom_GridPoints:end,:)=1;
149 if Options(2)==1;
150 Type = 'Steel';       %'Steel' or 'PELD'
151 switch Type
152 case 'Steel'
153 medium.density(Bottom_Mask==1)=Density_Steel;
154 medium.sound_speed_compression(Bottom_Mask==1)  = Sound_Compr_Steel;
155 medium.sound_speed_shear(Bottom_Mask==1)  = Sound_Shear_Steel;
156 medium.alpha_coeff_compression(Bottom_Mask==1)  = alpha0_p_Steel;
157 medium.alpha_coeff_shear(Bottom_Mask==1)  = alpha0_s_Steel;
158 case 'PELD'
159 medium.density(Bottom_Mask==1)=Density_PELD;
160 medium.sound_speed_compression(Bottom_Mask==1)  = Sound_Compr_PELD;
161 medium.sound_speed_shear(Bottom_Mask==1)  = Sound_Shear_PELD;
162 medium.alpha_coeff_compression(Bottom_Mask==1)  = alpha0_p_PELD;
163 medium.alpha_coeff_shear(Bottom_Mask==1)  = alpha0_s_PELD;
164 end
165 end
166
167 %---------- PARTICLES IN THE COLUMN
168 if Options(3)==1;
169 % -- Creating the porous particle bed
170 % -- Creating the porous particle bed
171 Image_Particles=zeros(Nx,Ny);
172 Starting_Level_Particles=round(Starting_Level_Particles/dx);
173 i_x=Starting_Level_Particles;
174 while i_x<=Depth_Bottom_GridPoints
175 i_y=Left_x_ID;
176 while i_y<=Right_x_ID
177 Random_Number =rand;
178 if Random_Number <= 1-Desired_Porosity
179 Image_Particles(i_x,i_y)=1;
180 end
181 i_y=i_y+1;
182 end
183 i_x=i_x+1;
184 end
185 Particle_Mask=Image_Particles;
186 %figure,imshow(Particle_Mask);
187 Type = 'Glass'; %'Seph'
188 switch Type
189 case 'Seph'
190 medium.density(Particle_Mask==1)=Density_Seph;
```

```
medium.sound_speed_compression(Particle_Mask==1)  = Sound_Compr_Seph;
medium.sound_speed_shear(Particle_Mask==1)  = Sound_Shear_Seph;
medium.alpha_coeff_compression(Particle_Mask==1)  = alpha0_p_Seph;
medium.alpha_coeff_shear(Particle_Mask==1)  = alpha0_s_Seph;
case 'Toyo'
medium.density(Particle_Mask==1)=Density_Toyo;
medium.sound_speed_compression(Particle_Mask==1)  = Sound_Compr_Toyo;
medium.sound_speed_shear(Particle_Mask==1)  = Sound_Shear_Toyo;
medium.alpha_coeff_compression(Particle_Mask==1)  = alpha0_p_Toyo;
medium.alpha_coeff_shear(Particle_Mask==1)  = alpha0_s_Toyo;
case 'Glass'
medium.density(Particle_Mask==1)=Density_Glass;
medium.sound_speed_compression(Particle_Mask==1)  = Sound_Compr_Glass;
medium.sound_speed_shear(Particle_Mask==1)  = Sound_Shear_Glass;
medium.alpha_coeff_compression(Particle_Mask==1)  = alpha0_p_Glass;
medium.alpha_coeff_shear(Particle_Mask==1)  = alpha0_s_Glass;
end
end

%-------- BOTTOM TRANSDUCER
if Options(4)==1;

end

%==========================================================================
% CREATE THE TIME ARRAY
%==========================================================================
kgrid.t_array= makeTime(kgrid, medium.sound_speed_compression, cfl, t_end);

%==========================================================================
% DEFINE ULTRASOUND TRANSDUCER
%==========================================================================
% This function recreates 1 "round" transducer on top
Trans_Diam_Grid = Trans_Diam_Orig/dy;        % Transducer size in grid points
% Placing the transducer in the middle
Left_x_Trans=Ny/2-(Trans_Diam_Grid/2);
Right_x_Trans=Ny/2+(Trans_Diam_Grid/2);
Ini_y_Trans=5;
End_y_Trans=5;
Transducer_Mask=zeros(Nx,Ny);
Transducer_Mask(Ini_y_Trans:End_y_Trans,Left_x_Trans:Right_x_Trans)=1;
%figure, imshow(Transducer_Mask);

%==========================================================================
% DEFINE SIGNAL
%==========================================================================
Wavelength = Sound_Compr_Water/source_freq*1000; % in mm
source_cycles = 100;              % number of tone burst cycles
source.s_mask = Transducer_Mask;
source.sxx = -source_mag*toneBurst(1/kgrid.dt, source_freq, source_cycles);
source.sxx = -source_mag*sin(2*pi*source_freq*kgrid.t_array);
source.sxx = filterTimeSeries(kgrid, medium, source.sxx);
source.syy = source.sxx;

%==========================================================================
% DEFINE SENSOR
%==========================================================================
% create a sensor mask covering the entire computational domain using the
% opposing corners of a rectangle
sensor.mask = [1, 1, Nx, Ny].';

%==========================================================================
% DEFINE SIMULATION PARAMETERS
%==========================================================================
try
Display_Mask = source.s_mask;        % Display mask - transducer, p-sources,etc
catch
end
try
Display_Mask = Display_Mask + Column_Mask;
catch
end
```

```
try
Display_Mask =Display_Mask + Particle_Mask;
catch
end
try
Display_Mask= Display_Mask+Bottom_Mask;
catch
end
if Wait_For_Confirmation ==1;
figure,imshow(Display_Mask);
disp('Check the masks')
k = waitforbuttonpress;
end
% set the input arguments
input_args = {'PlotPML', true, 'PMLInside', false, 'PlotScale', [-1, 1]*source_mag, ...
   'PMLSize', [PML_X_SIZE, PML_Y_SIZE]...
   'PlotSim',true,...
   'DisplayMask', 'off', 'DataCast', 'single'};

%==========================================================================
% RUN SIMULATION - PREPARE RESULTS
%==========================================================================
sensor_data = pstdElastic2D(kgrid, medium, source,sensor, input_args{:});

if Save_Variables==1
save(Mat_Filename)
end

u_rms = sqrt(sensor_data.ux_rms.^2 + sensor_data.uy_rms.^2);
%==========================================================================
% VISUALISATION - SAVING DATA
%==========================================================================
%------- Pressure
figure, imagesc(kgrid.y_vec*1e3, (kgrid.x_vec - min(kgrid.x_vec(:)))*1e3,sensor_data.p_rms/(0.1e6));    % Pressure in bars
colormap(jet(256));
c = colorbar;
ylabel(c, 'Pressure [MPa]','FontName','Times New Roman','FontSize',20);
axis image;
str = {['P^{2}_{rms}, \phi_{Tr}= ', num2str(Trans_Diam_Orig*1000), 'mm, \lambda=',num2str(round(Wavelength,2)),'mm P_{Ini}=
      ',num2str(source_mag/(0.1e6)),...
   ' bar, Freq= ', num2str((round(source_freq/1e6,2))), ' GHz'];
   [' X-axis= ', num2str((round(Length_X*100,2))),' cm, Y-axis= ',...
   num2str((round(Length_Y*100,2))),' cm, Res= ',num2str((round(dy*1000,2))),' mm']};
title(str,'FontName','Times New Roman','FontSize',16)
% ax = gca;
% New_Y_ticks = ax.YTick.*1000;
% New_X_ticks = ax.XTick.*1000;
% ax.XTickLabel = New_X_ticks;
% ax.YTickLabel = New_Y_ticks;
xlabel('Y-Position (mm)','FontName','Times New Roman','FontSize',20);
ylabel('X-Position (mm)','FontName','Times New Roman','FontSize',20);

%------- Velocity
figure, imagesc(kgrid.y_vec*1e3, (kgrid.x_vec - min(kgrid.x_vec(:)))*1e3,u_rms);
colormap(jet(256));
c = colorbar;
ylabel(c, 'Velocity [mm/s]','FontName','Times New Roman','FontSize',20);
axis image;
str = {['U^{2}_{rms}, \phi_{Tr}= ', num2str(Trans_Diam_Orig*1000), 'mm, \lambda=',num2str(round(Wavelength,2)),'mm P_{Ini}=
      ',num2str(source_mag/(0.1e6)),...
   ' bar, Freq= ', num2str((round(source_freq/1e6,2))), ' GHz'];
   [' X-axis= ', num2str((round(Length_X*100,2))),' cm, Y-axis= ',...
   num2str((round(Length_Y*100,2))),' cm, Res= ',num2str((round(dy*1000,2))),' mm']};
title(str,'FontName','Times New Roman','FontSize',16)
% ax = gca;
% New_Y_ticks = ax.YTick.*1000;
% New_X_ticks = ax.XTick.*1000;
% ax.XTickLabel = New_X_ticks;
% ax.YTickLabel = New_Y_ticks;
xlabel('Y-Position (mm)','FontName','Times New Roman','FontSize',20);
ylabel('X-Position (mm)','FontName','Times New Roman','FontSize',20);

```

```
%------- GORKOV
Gorkov_Question=0;
if Gorkov_Question==1
figure, imagesc(kgrid.y_vec*1e3, (kgrid.x_vec - min(kgrid.x_vec(:)))*1e3,sensor_data.p_rms/(0.1e6));
colormap(jet(256));
c = colorbar;
ylabel(c, 'Pressure [MPa]','FontName','Times New Roman','FontSize',20);
axis image;
str = {['P^{2}_{rms}, \phi_{Tr}= ', num2str(Trans_Diam_Orig*1000), 'mm, \lambda=',num2str(round(Wavelength,2)),'mm P_{Ini}=
      ',num2str(source_mag/(0.1e6)),...
   ' bar, Freq= ', num2str((round(source_freq/1e6,2))), ' GHz'];
   [' X-axis= ', num2str((round(Length_X*100,2))),' cm, Y-axis= ',...
   num2str((round(Length_Y*100,2))),' cm, Res= ',num2str((round(dy*1000,2))),' mm']};
title(str,'FontName','Times New Roman','FontSize',16)
% ax = gca;
% New_Y_ticks = ax.YTick.*1000;
% New_X_ticks = ax.XTick.*1000;
% ax.XTickLabel = New_X_ticks;
% ax.YTickLabel = New_Y_ticks;
xlabel('Y-Position (mm)','FontName','Times New Roman','FontSize',20);
ylabel('X-Position (mm)','FontName','Times New Roman','FontSize',20);

figure, surf(sensor_data.p_rms), colormap(jet)
title(str,'FontName','Times New Roman','FontSize',16)
end
```